Chem Soc Rev

Chemical Society Reviews

N

S

B

F

H

ROYAL SOCIETY
OF CHEMISTRY

175 YEARS

REVIEW ARTICLE
Martin Pumera *et al.*
Graphene and its electrochemistry – an update

CrossMark
←click for updates

Graphene and its electrochemistry – an update

Adriano Ambrosi,† Chun Kiang Chua,† Naziah Mohamad Latiff, Adeline Huiling Loo, Colin Hong An Wong, Alex Yong Sheng Eng, Alessandra Bonanni and Martin Pumera*

The electrochemistry of graphene and its derivatives has been extensively researched in recent years. In the aspect of graphene preparation methods, the efficiencies of the top-down electrochemical exfoliation of graphite, the electrochemical reduction of graphene oxide and the electrochemical delamination of CVD grown graphene, are currently on par with conventional procedures. Electrochemical analysis of graphene oxide has revealed an unexpected inherent redox activity with, in some cases, an astonishing chemical reversibility. Furthermore, graphene modified with p-block elements has shown impressive electrocatalytic performances in processes which have been historically dominated by metal-based catalysts. Further progress has also been achieved in the practical usage of graphene in sensing and biosensing applications. This review is an update of our previous article in *Chem. Soc. Rev.* 2010, **39**, 4146–4157, with special focus on the developments over the past two years.

1. Introduction

Graphene and its derivatives, such as graphene oxide, doped and functionalized graphene materials, is the major focus in the area of materials science research.[1,2] The high conductivity, large surface area and high electron transfer rate of graphene are the underlying reasons for its extensive usage in modern electrochemistry related technologies. This is further enhanced by the fact that the carbon backbone of graphene can be covalently or non-covalently functionalized with heteroatoms (non-carbon atoms), as it unlocks the potential of tailoring its electrochemical and electrical properties to cater to various applications.

In 2010,[3] when research on the electrochemistry of graphene was just taking off, we have contributed a tutorial review on the topic. Now six years later, we wish to provide a more comprehensive overview on the electrochemistry of graphene, focusing mostly, but not exclusively, on its developments over the past two years. In the first section of this review, an overview on the preparation of graphene based on electrochemical techniques, mainly by electrochemical exfoliation of graphite and electrochemical delamination of chemical vapour deposited graphene, would be provided. Subsequently, the modification of graphene *via* electrochemically-induced reactions as well as the major factors that influence the capacitance of graphene would

Division of Chemistry & Biological Chemistry, School of Physical and Mathematical Sciences, Nanyang Technological University, Singapore 637371, Singapore.
E-mail: pumera.research@gmail.com; Fax: +65-6791-1961
† Authors contributed equally.

be reviewed. Next, the variations of electrocatalytic properties of graphene materials, as conferred by the introduction of hetero-atoms (also known as doping) such as p-block (*i.e.*, B, N, S, P, halogens) and d-block elements, would be addressed. Lastly, the usage of graphene for sensing and biosensing applications would be critically reviewed to also include important practical considerations.

We believe that this review is a timely insight into the quintessence of graphene electrochemistry.

2. Electrochemically assisted fabrication of graphene

The use of chemical methods currently available for the preparation of graphene and graphene materials guarantees certain positive outcomes but suffers from major drawbacks as well. For example, liquid-phase exfoliation of graphite in organic solvents assisted by sonication and/or mechanical shearing can provide extremely high quality graphene with low density of defects and negligible presence of oxygen functionalities, but the exfoliation efficiency is extremely low with yields generally of <1%.[4] Higher efficiencies can be achieved if an intercalation step is introduced prior to exfoliation. The formation of such graphite intercalation compounds (GIC) normally requires strong oxidants and acids which assist in splitting the graphene layers apart to facilitate exfoliation.[5] However, this is achieved at the cost of significant function-alization with various oxygen groups and/or structural damage to the resulting graphene.[5] If we take into consideration the

bottom-up chemical vapor deposition (CVD) of graphene onto catalytic metallic substrates, this allows greater control over the quality and quantity of graphene sheets produced. However, it is limited by the need for post-production chemical etching of the metal substrate in order to separate graphene for transfer to more useful surfaces. Such chemical etching is time-consuming, and more importantly, cannot guarantee the complete removal of the catalytic metal substrate which always remains strongly adsorbed onto the graphene in the form of atomic species and/or nanometer-sized metal impurities. These impurities have profound influences on the electronic and electrochemical properties of graphene.[6–8]

The electrochemical technique has recently regained great interest due to very promising results not only in assisting the exfoliation of graphite but also as a powerful method to control the delamination of CVD graphene. Much higher yields have been achieved with the electrochemical exfoliation of graphite apart from the possibility to control the chemical and structural features of the produced graphene. As for the electrochemical assisted delamination of CVD graphene, this method has demonstrated good control, minimal structural damage and functionalization, no residual contamination and more importantly, it is an extremely fast process compared to the aforementioned chemical etching technique. A detailed review of the most recent methods based on electrochemistry to either exfoliate graphite or to delaminate CVD graphene from the metal substrate is presented in the following sub-sections.

2.1 Electrochemical exfoliation of graphite

The electrochemically assisted exfoliation of graphite consists of the application of a cathodic or anodic potential to a graphite working electrode in aqueous or organic electrolytes. A second Pt electrode is generally used in a two-electrode electrochemical system while Pt and reference (*e.g.* Ag/AgCl, SCE, *etc.*) electrodes are used in a standard three-electrode electrochemical system.

The usage of positive (anodic) potential facilitates the intercalation of negative anions into the graphite layers. This results in the gradual expansion of graphite leading to successive exfoliation to form graphene flakes. One of the drawbacks of this method is the introduction of a significant amount of oxygen functionalities into the produced graphene material with consequences for its electrical properties. On the other hand, a negative (cathodic) potential drives the intercalation of positive ions from the electrolyte into graphite layers followed by expansion and exfoliation. In general, this approach is less efficient and slower as compared to anodic exfoliation. However, cathodic exfoliation produces graphene flakes of higher quality. Some methods combine both the anodic and cathodic potentials, in which the initial potential is applied to drive intercalation while the reverse potential is used to facilitate exfoliation.

The use of electrochemical methods to intercalate ions and compounds inside graphite layers was first demonstrated more than thirty years ago (1980s) when graphite intercalation compounds (GICs) were prepared with Li^+ ions,[9] F^- ions,[10,11] Ni^{2+} ions[12] or sulfuric acid,[13] in aqueous or organic solvents. Such intercalation methods are aimed exclusively at the preparation of "graphitic salts" as promising materials for batteries, mainly to serve as catalysts and also as materials with tunable electrical and electronic properties. However, it is only after the discovery of the extraordinary properties of graphene that the electrochemical approach experienced renewed scientific interest as a promising scalable method for the preparation of graphene. The first attempt was made by Wang and collaborators in 2009 where they employed poly(styrenesulfonate) (PSS) as an electrolyte and two graphite rods as cathode and anode electrodes.[14] A 5 V bias to the electrodes was applied for over 4 h during which a black product was released from the anode. After characterization, graphene flakes showed quite a significant density of defects and presence of oxygen functionalities as well

Pumera's group originated in the wonderful National Institute for Materials Science, Tsukuba, Japan, in 2006. In 2010, this group, having two members, moved to Nanyang Technological University, Singapore (M. Pumera renounced ERC-StG offer at EPFL at that time) where quickly grew to current 20+ members. It consists of Martin, four postdoctoral researchers, a lecturer, thirteen PhD students, three master students and countless undergraduates. This group takes pride in the fact that it has produced three young faculty members, who are strategically located from the Iberian to Malay Peninsula, thus spanning the whole Eurasian continent; we have trained 17 PhD students and over forty undergraduate students. Pumera's group has broad interests in nanomaterials and microsystems, in the specific areas of electrochemistry and synthetic chemistry of carbon nanomaterials, layered anisotropic materials, nanotoxicity, micro- and nanomachines and 3D printing. This group produced over 400 papers (some of them are reviewed here) which received over 14 000 citations. "We enjoy finding things out".

as residual PSS molecules strongly adsorbed on them.[14] Since treatment with anodic potentials produces more defective graphene materials containing significant amounts of oxygen functional groups, cathodic exfoliation procedures have been attempted. It is worth mentioning the work by Morales *et al.* which carefully studied the effects of different reducing potentials applied to graphite foils in aqueous perchloric acid.[15] The produced graphene indeed showed a low D-band in the Raman spectra but due to the scarce efficiency of the exfoliation process, post-processing microwave thermal treatment and prolonged sonication in NMP were required to obtain a final dispersion. Based on similar cathodic processes, Loh *et al.* obtained remarkable results by employing a highly negative potential of −15 V in the presence of Li^+ ions in an organic propylene carbonate (PC) electrolyte. After prolonged sonication, an impressive value of over 70% of the graphene flakes had thickness of less than five layers although with reduced lateral size due to prior sonication treatment.[16] An improved cathodic procedure was later proposed by Zhong and Swager who employed a milder cathodic potential of −5 V, but in two successive steps. The first expansion was done in the presence of Li^+ ions in PC, followed by a second treatment with the same potential but in the presence of a larger cation, tetra-*n*-butylammonium (TBA) (Fig. 1a). After extensive washing to remove the residual Li ions, the material showed extremely low oxygen content (Fig. 1b and c). However the presence of defects was still detected by Raman spectroscopy (Fig. 1e).[17] Cooper *et al.* used tetramethylammonium perchlorate (TMA ClO_4), tetraethylammonium tetrafluoroborate (TEA BF_4), and tetrabutylammonium tetrafluoroborate (TBA BF_4) as electrolytes to study the expansion and the exfoliation of different graphite sources (HOPG and graphite rods) using cyclic voltammetry in a three-electrode electrochemical system.[18]

In other procedures, a combination of both anodic and cathodic potentials has been used to facilitate the intercalation of electrolyte ions in the first step followed by the application of a reverse potential to drive the exfoliation process. For example, using an aqueous sodium dodecyl sulfate (SDS) solution, graphene sheets have been obtained from graphite rods by first applying a preliminary anodic potential of +1.6 V in order to obtain SDS-intercalated graphite followed by the application of −1 V to exfoliate the intercalated graphite.[19] Graphene flakes of 1–2 layers thick and around 0.5 μm in size were obtained in a stable graphene/SDS suspension. Apart from that, an ionic liquid [triethyl sulfonium bis (trifluromethyl sulfonyl) imide] (IL) electrolyte was used for the first time to provide greener alternatives to conventional methods that employ organic electrolytes. In such a study, a pencil graphite electrode was subjected to a potential of +8 V for 600 s followed by a step of 600 s with the reverse (−8 V) potential. The produced graphene flakes were 1–2 layers thick and have unexpectedly lower density of defects compared to the initial pencil graphite electrode.[20] In addition, cycles of anodic/cathodic potentials of ±10 V have been used in the presence of $NaClO_4$ in PC to exfoliate microcrystalline natural graphite minerals. In this work, the authors showed that high quality impurity-free graphene can be obtained despite the fact that the starting graphite material is rich in silicate and other impurities from the ore, which thus avoids complex preliminary purification steps.[21]

It is undoubtedly recognized that the electrochemical exfoliation of graphite electrodes using anodic potentials is far more efficient than using cathodic potentials, particularly in aqueous electrolytes. This is because the intercalation of anions is facilitated by the concomitant formation of radical species (*e.g.* •OH and •O) by the oxidation of water. These radical
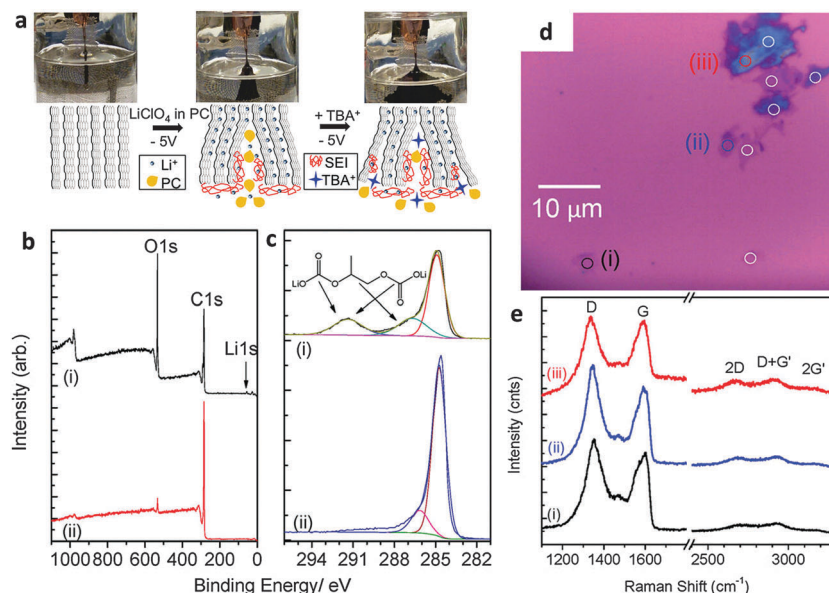

Fig. 1 (a) Schematic and images of electrochemical expansion of graphite. (b) XPS survey scans and (c) C1s XPS spectrum of electrochemically expanded graphene (i) after rinsing once with DMF and (ii) after extensive washing. (d) Optical micrograph of EFG spin-coated on silicon before laser ablation. (e) Raman spectra of selected spots (i) to (iii) as marked in panel d. Adapted with permission from ref. 17. Copyright (2012) American Chemical Society.

species oxidize/break the graphite structure starting from the edges and result in the surge of available openings for anions to penetrate. The successive formation of oxygen gas splits the graphene layers apart to provide a suspension of graphene. Therefore, such an exfoliation process is significantly accelerated but at the cost of a more defective and oxygen-functionalized graphene. A fast anodic exfoliation was demonstrated in sulfuric acid by Su and collaborators who applied a preliminary potential of +1 V for 5–10 min to wet a graphite sample and initiate the intercalation of SO_4^{2-} ions into the graphite. This was then followed by the application of a +10 V bias to the graphite anode which resulted in a massive exfoliation over 1 min. Between 5–8% of the collected product was single layer graphene and over 60% was bilayer graphene; oxygen content was quite low but according to Raman analysis, the graphene sheets presented an I_D/I_G ratio of around 0.7.[22] A similar procedure was proposed by Parvez et al. who by using a positive potential of +10 V in the H_2SO_4 electrolyte obtained graphene sheets with a lower I_D/I_G ratio (0.4) and low oxygen content. The graphene sheets were subsequently applied for organic electronics.[23] The same group later demonstrated a more efficient exfoliation method and production of higher quality graphene by using an aqueous solution of inorganic salts such as ammonium sulfate ($(NH_4)_2SO_4$), sodium sulfate (Na_2SO_4), and potassium sulfate (K_2SO_4) at neutral pH.[24] It is however important to notice that while the presence of edge plane defects on graphene materials can be detrimental for their mechanical properties and for some electronic applications, they are beneficial for other applications, such as electrochemistry in particular. It is well-known, in fact, that electron transfer processes on carbon materials occur at much higher rates at edge plane defects than on basal planes[25] and therefore anodic exfoliation of graphite could be the preferred method for electrochemical applications. In our group, we investigated the use of different aqueous electrolytes (i.e., H_2SO_4, Na_2SO_4 and $LiClO_4$) for anodic exfoliation of graphite foils (Fig. 2a–g). Subsequent structural characterization showed the presence of defects regardless of the electrolyte used (Fig. 2i), but interestingly the oxygen content could be tuned ranging from a very low C/O ratio of 8.8 using Na_2SO_4 to a value of 4.0 using $LiClO_4$ which is close to the values usually observed for the chemically produced graphene oxide (GO) materials (Fig. 2h). By varying the chemical features using different exfoliating electrolytes, the electrochemical properties of the produced graphene are also altered, which might suit different electrochemical applications (Fig. 2j–m).[26]

An improved exfoliation process proposed by Liu et al. applied anodic potentials in solutions of protonic acids (i.e., H_2SO_4, H_3PO_4 or $H_2C_2O_4$) as electrolytes in a vertical cell configuration with the graphite rod placed at the bottom of the cell. This system allowed for multiple exfoliation steps to improve the yield and quality of graphene.[27]

Rao et al. employed milder anodic conditions (+1–3 V) in the presence of an electrolyte solution containing NaOH, H_2O_2 and H_2O to obtain an impressive 95% yield of graphene with thickness between 3–6 layers. The authors highlighted the crucial role of H_2O_2 in the process as it reacts with hydroxyl ions to form the peroxide ion O_2^{2-}, which is a strong nucleophile that can effectively penetrate into the graphene layers.[28] The same group later proposed a more efficient exfoliation method that provides graphene of similar quality by using glycine–H_2SO_4 ionic complex electrolyte solution.[29] A recent interesting work by the Müllen group showed that the introduction of reducing agents during the anodic exfoliation process in aqueous electrolytes can eliminate highly reactive radicals that are generated from H_2O. Different reducing agents such as (2,2,6,6-tetramethylpiperidin-1-yl)oxyl (TEMPO), ascorbic acid and sodium borohydride were tested and the most effective additive which gave the highest quality graphene was TEMPO. The produced graphene sheets have large dimensions (5–10 μm), outstanding hole mobilities (~ 405 cm^2 V^{-1} s^{-1}), impressively low Raman I_D/I_G ratios (<0.1), and extremely high carbon to oxygen (C/O) ratios (~ 25.3).[30]

In addition, a recently published study aimed to investigate the effects of changing different parameters of the anodic exfoliation process on the quality of graphene. In this study, by varying the exfoliation time, the potential applied and the type of electrolyte, the authors carefully evaluated the efficiency of exfoliation, the density of defects and the electrical properties of graphene. As this study provides further insights into the crucial steps occurring during the electrochemical exfoliation process, it can certainly be a valuable reference to control the properties of electrochemically exfoliated graphene.[31]

2.2 Electrochemical delamination of CVD grown graphene

Electrochemical methods can also be applied to the transfer of CVD graphene, which is grown on catalytic metal substrates. The most commonly used transfer process typically starts with the spin-coating of a polymer support layer onto the graphene surface, followed by the removal of the metal foil by wet-etching in solutions such as iron chloride and ammonium persulfate. This chemical etching step takes several hours for the metal foil to be completely dissolved and can contaminate the graphene film with dissolved metals from either the foil or the etchant.[8] Furthermore, the metal waste incurs additional costs from both economical as well as environmental standpoints. In a bid to overcome these problems, Wang et al. pioneered an electrochemical method to delaminate poly(methyl methacrylate) (PMMA)/graphene films from Cu foil.[32] A PMMA/graphene/Cu stack was immersed in aqueous $K_2S_2O_8$ and held at a voltage bias of -5 V, causing the reduction of water and producing hydrogen bubbles as shown in the equation: $2H_2O + 2e^- \rightarrow H_2 + 2OH^-$. The H_2 bubbles generated at the graphene/Cu interface serve to delaminate the PMMA/graphene film from the Cu foil, starting from the edges exposed to the electrolyte and progressing to the rest of the film due to electrolyte permeation into the interlayers (Fig. 3A). Increasing the potential applied to the cathode as well as the concentration of electrolyte used resulted in quicker delamination. Complete delamination followed by transfer to desired substrates could be achieved in 60 min, a mere fraction of the duration required for traditional wet-etching techniques. The authors noted that
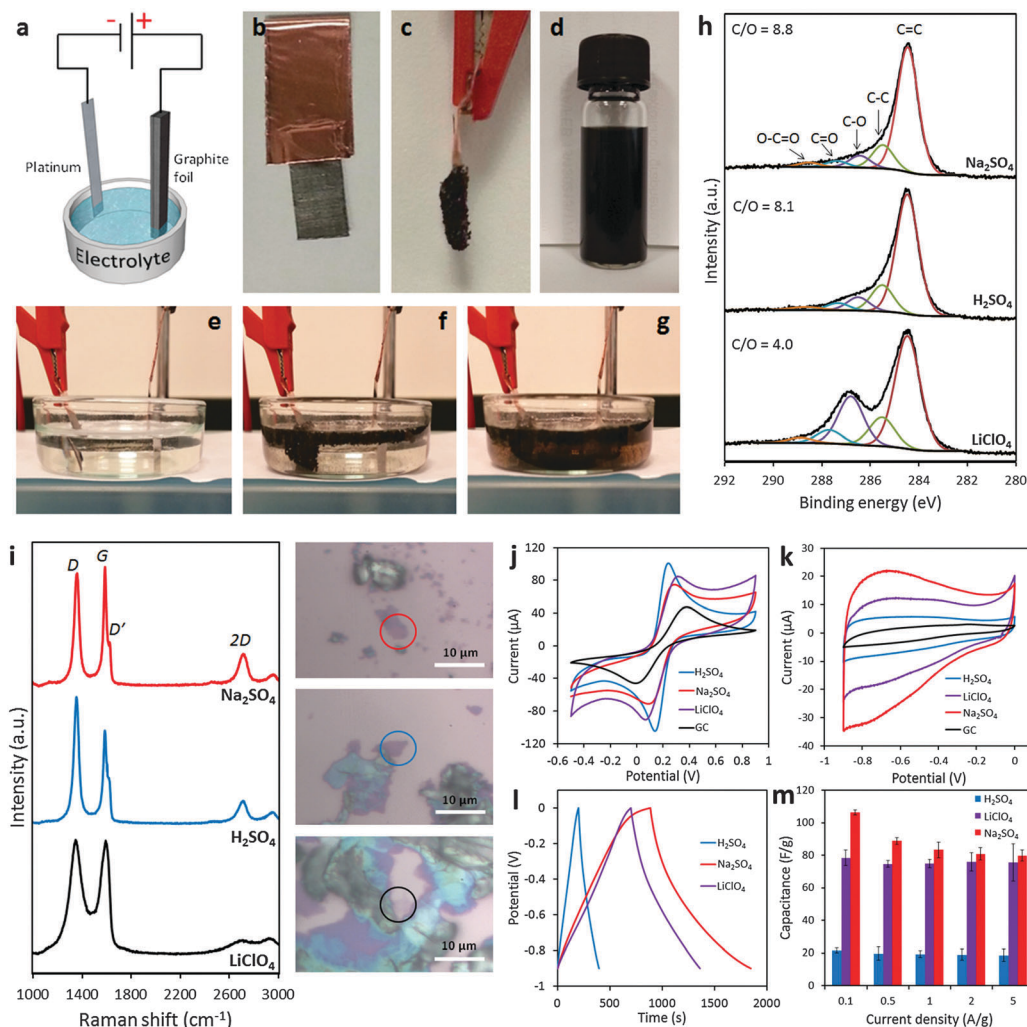
Fig. 2 (a) Schematic illustration of the experimental setup. Photos of graphite foil (b) before and (c) after the exfoliation process. (d) Graphene dispersion in DMF solution (1 mg mL^{-1}). Photos illustrating the exfoliation process at (e) time zero, (f) after 5 min, and (g) after 20 min. (h) High-resolution C1s XPS spectra of the electrochemically exfoliated graphene materials. Fitting peaks corresponding to different functional groups along with the C/O ratios for each material are also indicated. (i) Representative Raman spectra recorded for the graphene material obtained in Na$_2$SO$_4$ (red), H$_2$SO$_4$ (blue), and LiClO$_4$ (black) corresponding to the material portion as indicated in the optical images on the right. (j) Representative cyclic voltammograms recorded by using a GC electrode modified with graphene obtained in Na$_2$SO$_4$ (red), H$_2$SO$_4$ (blue), and LiClO$_4$ (purple) in the presence of a 5 mM Fe(CN)$_6$$^{3-/4-}$ redox probe in 0.1 M KCl electrolyte. (k) Cyclic voltammograms at a 100 mV s^{-1} scan rate in 6 M KOH solution recorded for the graphene material obtained in Na$_2$SO$_4$ (red), H$_2$SO$_4$ (blue), and LiClO$_4$ (purple). The voltammogram of the bare GC electrode (black) is also shown for comparison. (l) Galvanostatic charge/discharge curves recorded for all graphene materials at a current density of 0.1 A g^{-1} in 6 M KOH solution. (m) Summary of the gravimetric capacitance measured for all graphene materials at different current densities between 0.1 and 5 A g^{-1}. Adapted with permission from ref. 26. Copyright (2016) John Wiley and Sons.

only a small amount of Cu was electrochemically etched during each CVD growth–delamination–transfer cycle ($<$40 nm), allowing the Cu foil to be reused for hundreds of cycles for a 25 μm thick foil. Additionally, repeated etching/heating cycles caused the Cu foil to become increasingly smoother, due to the preferential etching of step edges and grain boundaries, coupled with the electrodeposition of Cu nanoparticles in trenches and concavities on the foil. This resulted in the improvement of the quality and charge carrier mobility of the grown graphene films with each successive cycle (Fig. 3B). Gao *et al.* later improved on this method by growing CVD graphene on Pt foil, which exhibits faster growth rates as well as lower

temperature requirements than Cu foil.[33] The PMMA/graphene/Pt stack then served as a cathode in a cell with aqueous NaOH, in which bubbling delamination took place and was completed in 30 s for a 1 × 3 cm^2 film under a constant current of 1 A. Owing to the chemical inertness of Pt, this delamination could be carried out without etching of the foil. Atomic terraces on the Pt substrate were maintained without any degradation even after several hundred growth and delamination cycles, implying that the Pt foils could be re-used indefinitely. Graphene films grown on the re-used Pt foils under the same growth conditions showed no obvious structural differences even after 100 transfers. Despite the great potential of the high-speed delamination of

2462 | *Chem. Soc. Rev.*, 2016, **45**, 2458–2493

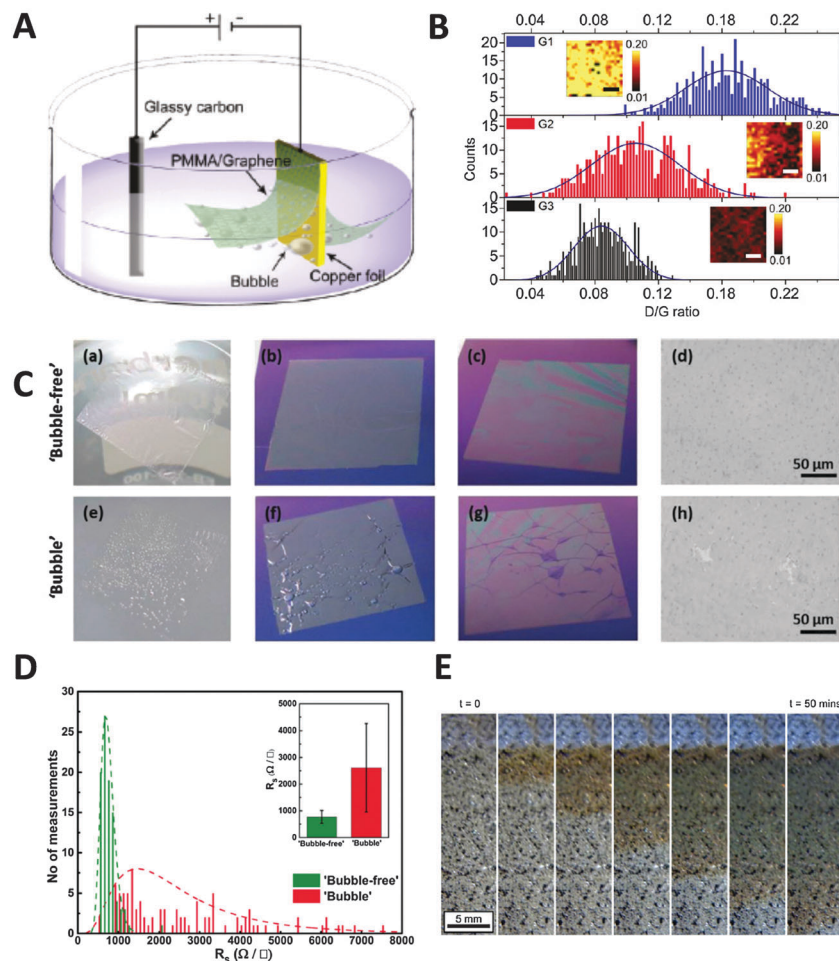This journal is © The Royal Society of Chemistry 2016

Fig. 3 Electrochemical delamination of CVD graphene from Cu foil. (A) Schematic of the electrochemical setup used in bubbling delamination. (B) Raman I_D/I_G ratios of graphene films G1, G2, and G3 during bubbling delamination (G1, G2, and G3 refer to the first, second, and third cycles of electrochemical delamination); inset: Raman I_D/I_G maps obtained from an area of 10×10 μm^2, scale bar = 3 μm. Reproduced with permission from ref. 32. Copyright (2011) American Chemical Society. (C) Comparison of films obtained from bubble-free (top) and bubbling (bottom) delamination at various stages of the transfer process: PMMA/graphene film floating on DI water after rinsing (a and e); immediately after transfer to Si wafer (b and f); after drying at 80 °C (c and g), as well as representative optical microscope images of the films (d and h; scale bars = 50 μm). (D) Histograms of sheet resistance measurements of bubble-free and bubbling delaminated graphene films. Inset: Average sheet resistance values of delaminated graphene films as well as their standard deviations. Reproduced with permission from ref. 35. Copyright (2015) John Wiley and Sons. (E) Optical images showing progression of the Cu oxidation front underneath CAB/graphene. Reproduced with permission from ref. 36. Copyright (2015) Elsevier.

CVD graphene from metal foils via electrochemical hydrogen bubbling, there is a possibility of mechanical damage to the graphene film due to the surface tension of bubbles at the polymer/graphene interface.[34] To avoid the formation of hydrogen bubbles, Cherian et al. developed an electrochemical delamination method at a less negative potential compared to bubbling delamination.[35] This method exploits the selective etching of adventitious cuprous oxide on the Cu foil surface ($Cu_2O + H_2O + 2e^- \rightarrow 2Cu + 2OH^-$) by holding the PMMA/graphene/Cu stack at -2.6 V in an unreferenced two-electrode electrochemical system, with 0.5 M NaCl as the electrolyte. To speed up the delamination in the absence of mechanical forces originally provided by bubbles, a gradual immersion technique was used, where the initially delaminated PMMA/graphene stack floating on the solution provided the driving force instead. Under these conditions, delamination of an $\sim$1.5 cm^2 sample could be completed

after 1–2 min without any visible formation of bubbles (Fig. 3C). Vigorous hydrogen evolution typically occurred at potentials more negative than -2.8 V. The graphene film obtained using "bubble-free" delamination adhered more uniformly to the final substrate, had a negligible amount of mechanical damage, and had lower sheet resistance than that obtained from hydrogen bubbling delamination (Fig. 3D). The authors also commented that their "bubble-free" method did not exclude the evolution of hydrogen, but noted that the very slow rate of hydrogen production enabled hydrogen to diffuse into the solution instead of forming a gas phase at the graphene/Cu interface. A similar method was demonstrated by Pizzocchero et al. for CVD graphene grown on copper catalyst surfaces, in particular copper thin films deposited on support substrates.[36] Such thin films tend to delaminate at the Cu/support interface rather than the graphene/Cu interface in the presence of small amounts of hydrogen bubbling; it is thus

important to ensure that hydrogen production from the thin film is kept to an absolute minimum, if not completely eliminated. In this procedure, CVD graphene was grown on Cu thin films sputtered on a SiO_2/Si support, and then spin-coated with cellulose acetate butyrate (CAB). Once immersed in a supporting electrolyte (1 M KCl), the Cu thin film oxidised to Cu_2O by dissolved oxygen present in the electrolyte, which started to weaken the adhesion of graphene to the catalyst surface. The CAB/graphene/Cu stack was then held at a potential of -0.4 V (vs. Ag/AgCl), which is sufficient to reduce Cu_2O back to Cu but at the same time preventing the evolution of hydrogen. A localised excess of hydroxide ions was produced and capillary forces aided in drawing more electrolyte further between the graphene film and Cu, which ultimately resulted in the delamination of the graphene film without removing Cu from the support substrate. No change in the mass or thickness of the Cu catalyst layer could be detected even after being exposed to the delamination conditions for 100 h. The Cu/support could then be reused for further CVD growth and delamination cycles, limited only by the loss of small amounts of catalyst through evaporation of Cu during CVD growth. However, time taken for complete delamination of graphene from Cu was significantly slower due to the milder conditions used, with the Cu oxidation front proceeding at an average rate of 24 mm per hour (Fig. 3E).

Alternatively, the Cu foil itself can also be electrochemically etched away to leave just the PMMA/graphene film, using a fraction of the time needed for conventional wet-etching techniques (although the Cu foil is wasted as well). Yang et al. showed that etching could be accelerated by holding a PMMA/graphene/Cu stack at a potential of $+0.5$ V (vs. SCE) in 0.5 M sulfuric acid.[37] In this acidic environment, Cu was oxidised to Cu^{2+} ions, which readily diffused into the bulk solution (Fig. 4A). As the electrochemical reaction proceeded and Cu was etched away, the current initially decreased slowly (Fig. 4B). A rapid drop in current values signified the point where the foil was etched into increasingly discontinuous Cu islands; however, the continuous and highly conductive graphene film then served as an electrode to facilitate the further etching of these Cu islands. In the final stage, current values dropped to almost zero, indicating that the electrochemical etching process was complete (within 10 min). Visual observation of the electrochemical etching process could be carried out using optical microscopy at different stages of etching (Fig. 4C–E). Electrochemical oxidation afforded the graphene film showing less p-doping than traditional wet-etching, was significantly faster, and avoided the additional contamination of iron impurities from Fe-based chemical etchants. Since the oxidative etching of Cu occurs at the anode, this process can be coupled with the abovementioned bubbling delamination (at the cathode) to improve transfer efficiency. Shi et al. employed such a bi-electrode electrochemical transfer system by using identical PMMA/graphene/Cu stacks as both electrodes, immersing them in 0.1 M $(NH_4)_2S_2O_8$, and then applying a voltage of $+2$ V to the anode (Fig. 4F).[38] This electrolyte and concentration were chosen because while an acidic environment was necessary for the dissolution of Cu_2O to Cu^{2+} at the anode, the generation of H_2 bubbles at the cathode would be too vigorous if the H^+ ion
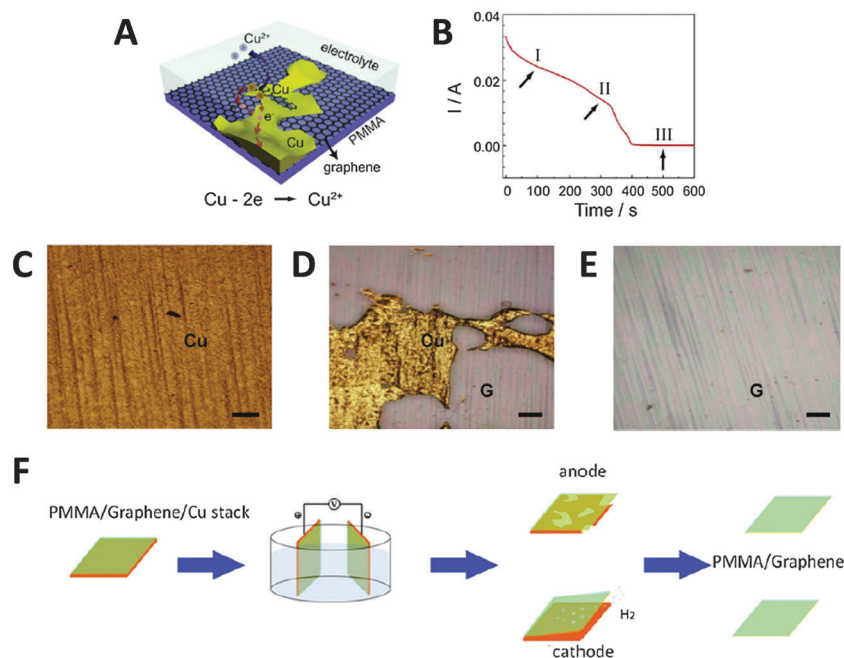

Fig. 4 Transfer of graphene thin films by electrochemical etching of a metal substrate. (A) Schematic of PMMA/graphene/Cu stack and the electrochemical reactions that occur during the etching process. (B) Evolution of current values measured during the etching process at $+0.5$ V (vs. SCE) in 0.5 M H_2SO_4. (C–E) Optical micrographs of the sample taken during stages I, II, and III of the etching process as shown in (B). G denotes the graphene film, scale bars = 200 μm. Reproduced with permission from ref. 37. Copyright (2013) Elsevier. (F) Schematic of the bi-electrode setup used for coupling electrochemical etching (anode) with bubbling delamination (cathode) for the simultaneous production of two PMMA/graphene films. Reproduced with permission from ref. 38. Copyright (2014) IOP Publishing.

concentration is high, potentially damaging the graphene film. Under these experimental conditions, two graphene films could be obtained simultaneously from a single setup within 20 min. The cathode (electrochemical oxidative etching) graphene showed higher p-doping than traditional metal-etched graphene, while the anode (bubbling delamination) graphene had less p-doping, which the authors attributed to differing electron loss/gain of graphene at their respective electrodes. The measured sheet resistance of both electrochemically-derived graphene samples was somewhat higher than that of metal-etched graphene, although their resistance distributions were narrower, hinting at more uniform graphene films being obtained via the electrochemical methods.

3. Graphene oxide as an electrochemically active material

3.1 Inherent redox activity of oxygen functional groups

A popular "top-down" approach to graphene production is the exfoliation and reduction of graphite oxide. This first involves graphite oxidation by chemical means using a combination of strong acids and oxidants, followed by subsequent reduction/exfoliation via thermal, chemical or electrochemical means. Ultrasonication may also be employed to facilitate exfoliation,

which produces graphene oxide (GO). In contrast to pristine graphene, the chemical (and electrochemical) characteristics of GO are exuberant due to its many reactive oxygen functionalities that include hydroxyls, epoxides, carbonyls, quinones, and carboxylic acids. Electrochemical reduction of GO was first explored in depth by Dong and co-workers, who used linear sweep voltammetry for GO electroreduction in aqueous solution at varying pH (Fig. 5A).[39] With application of a reductive potential, optical images show the gradual colour change from the yellow-brown of GO (Fig. 5B-i) to black for reduced-graphene near the electrode tip (Fig. 5B-ii) due to regeneration of π-conjugation. Although electrode morphology remains relatively unchanged (Fig. 5B, right panel), the deoxygenation of oxygen groups is confirmed by XPS and elemental analysis.

It is also crucial to note that differences in the composition of oxygen functionalities exist between GOs produced by various preparation methods (Fig. 5C).[40] All GOs exhibit characteristic reduction peaks and the peak potential typically correlates with the oxidation extent of GO in the order: Staudenmaier (ST) < Hofmann (HO) < Hummers (HU) < Tour (TO). This is because groups like carbonyls require stronger reductive overpotentials than epoxyls, peroxyls or aldehydes. More importantly, reductions occur irreversibly for the Staudenmaier and Hofmann GOs appearing only within the first cathodic sweep (Fig. 5C-i and ii). Interestingly however, chemically reversible behavior is observed
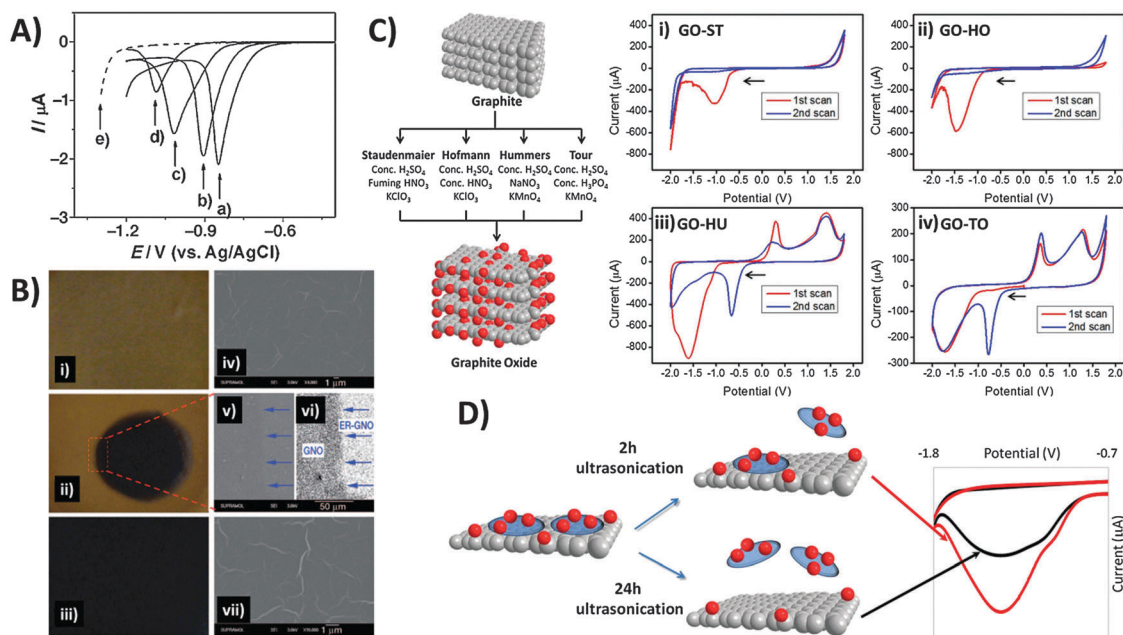

Fig. 5 Electrochemical behavior of inherent oxygen functionalities present in graphene oxide. (A) Linear sweep voltammograms of the GC electrode in contact with graphene oxide films on quartz, measured at pH values of (a) 4.12, (b) 7.22, (c) 10.26, and (d) 12.11. (e) Linear sweep voltammogram of the GC electrode in PBS (1 M, pH 4.12). (B) Optical (i–iii) and SEM images (iv–vii) of GO films before (top panel), during (1000 s; middle panel) and after electrolysis (5000 s; bottom panel). Image (vi) was obtained from image (v) using contrast enhancement. Arrows indicate the boundary between the reduced circular area and the unreduced surrounding GO. Reprinted with permission from ref. 39. Copyright (2009) John Wiley and Sons. (C) Scheme illustrating oxidation methods used for graphite oxide production. Cyclic voltammograms of GOs prepared from the methods of (i) Staudenmaier, (ii) Hofmann, (iii) Hummers, and (iv) Tour, with starting cathodic scan. Conditions: 50 mM PBS, pH 7.2, scan rate: 100 mV s^{-1}. All potentials are relative to the Ag/AgCl reference electrode. Reprinted with permission from ref. 40. Copyright (2013) John Wiley and Sons. (D) Effect of 2 h (red line) versus 24 h (black line) ultrasonication times on the cyclic voltammograms of GO as performed in 0.1 M PBS at pH 7. Reprinted with permission from ref. 41. Copyright (2014) American Chemical Society.

This journal is © The Royal Society of Chemistry 2016

Chem. Soc. Rev., 2016, 45, 2458–2493 | 2465

for the Hummers and Tour GOs, with new oxidation and reduction waves that persist after activation from the initial cathodic sweep (Fig. 5Ciii and iv). It was noticed that this disparity primarily arises from the choice of oxidising agent: either chlorate from the Staudenmaier and Hofmann methods or permanganate from the Hummers and Tour methods. The low Mn content measured from ICP-MS as compared to the large reduction charge passed additionally invalidates the possibility that manganese-based esters or impurities may be responsible. High resolution carbon-1s XPS and data from pH studies further suggest quinone–hydroquinone couples as likely sources of the reversible electrochemistry in GO-HU and GO-TO. As GO production is essentially a bulk oxidation and exfoliation process, it is also easy to envisage some heterogeneity in the size and stoichiometry of GO sheets. Particularly, small and highly oxidised sheets, known to be oxidative debris (OD), have been previously shown to exhibit fluorescence but are also likely the major contributors to the observed electroactivity.[41] OD fragments are typically strongly adsorbed on larger GO sheets due to π–π stacking, therefore requiring extended sonication times for desorption. Increasing sonication times in principle dislodge larger amounts of OD from the GO sheets, analogous to a cleaning procedure. Thus as seen in Fig. 5D, intensity of the reduction peak for precipitated GO sheets decreases with longer sonication due to OD removal. In this regard, one should always consider possible variations in GO electrochemistry as a result of either the oxidation method or experimental procedures (e.g. sonication times) employed during the material preparation process.

3.2 Applications of graphene oxide activity and its practical limitations

In light of the chemical reactivity of GO, several applications have been developed that exploit it for specific uses. The majority of graphene-modified electrodes to date are prepared through the technique of drop-casting, but also through spin-coating to a smaller extent. Subsequently, Luo and co-workers showed in a 2011 report and in subsequent studies that a reduced-graphene film may be prepared through electrochemical deposition for sensing applications.[42] The technique capitalizes on the solubility of GO in aqueous media due to its polar oxygen groups, compared to the poor dispersibility of graphene. Potential cycling of a 1.0 mg mL^{-1} GO dispersion in phosphate buffer at pH 9.18 (Fig. 6A) demonstrates a reduction at approximately -1.0 V vs. SCE, and a redox pair at 0.0 V similar to the inherent electroactivity of permanganate-oxidized GOs earlier discussed. The increase in peak currents with each cycle of deposition and film formation can be easily tracked using SEM. Consequently, sensing of a hydroquinone and catechol mixture was found to be significantly enhanced with the deposited graphene film in contrast to the lower sensitivity of bare glassy carbon electrodes (Fig. 6B) whether CV or DPV techniques were employed. In addition to detection of redox analytes, biological sensing is also feasible through the use of GO as an electrochemically-active label.[43] Selective thrombin aptasensing is achieved through a protocol first involving modification of a commercial carbon electrode with the thrombin aptamer (Fig. 6C). Upon exposure to thrombin, specific binding with the physically immobilised thrombin aptamer results in its partial release from the electrode surface, subsequently resulting in large uncovered surfaces for charge transfer between GO and the electrode. Detection is then based on voltammetric reduction of the inherent oxygen groups from the nanoplatelets, with a larger signal occurring in the case with thrombin.

Despite the usefulness of inherent GO activity towards sensing, it nonetheless places certain restrictions on its own applicability. The primary concern is that reliable detection cannot be achieved for any analyte with electrochemical activity occurring in the same region as the activity of inherent GO functionalities. This difficulty in distinguishing the voltammetric waves of the analyte and the material limits the usable potential window of the electrode. Such a situation is demonstrated for chlorate-based GO-ST against the permanganate-based GO-HU.[44] Anodic detection of molecules like ascorbic acid and dopamine are possible for GO-ST with no influence from the underlying electrode (Fig. 6Di and iii). For GO-HU however, its inherent oxidation overlaps with those from both analytes (Fig. 6Dii and iv), preventing any quantification data from being extracted. Hence, special care should be exercised when working with redox active graphene materials such as GO especially in sensing applications, and a simple measurement of the electrode material in a blank electrolyte is highly recommended for experimentalists before they proceed with any sensing protocols.

3.3 Electrochemical modification/activation of graphene oxide for tuning its electron transfer properties towards sensing and capacitance

Whilst we have seen that the inherent activity of GO can either be a boon or bane, it is reassuring to note that the oxygen content can in fact be controlled or tuned through prior electrochemical treatment. Electrochemical activation can be simply performed by application of a cathodic or anodic potential which tunes the surface oxygen composition and consequently the electron transfer properties of the material. In most cases with GO, electro-reduction of the oxygen groups greatly improves the heterogeneous electron transfer (HET) rate. Using XPS to identify changes in surface oxygen functionalities for a GO film on a screen-printed electrode (Fig. 7A), we observed the gradual loss of C–O and C=O groups with increasingly reductive potentials applied.[45] Peak separations for the ferro/ferricyanide redox couple decreased correspondingly, with HET rates increasing 1000-fold from 1.6×10^{-6} cm s^{-1} for the untreated GO film to 4.0×10^{-3} cm s^{-1} with an applied potential of -1.50 V. It should be noted however that strongly reducing potentials past -1.50 V vs. Ag/AgCl cause irreversible film damage for the screen-printed electrode due to hydrogen evolution. Additionally, changes in electron transfer properties due to electrochemical activation can also differ between various redox probes. For example, while both Fe(CN)$_6^{3-/4-}$ and Fe$^{2+/3+}$ are typically described as inner-sphere probes due to their sensitivity to surface oxygen groups,[46] a strong dependence of
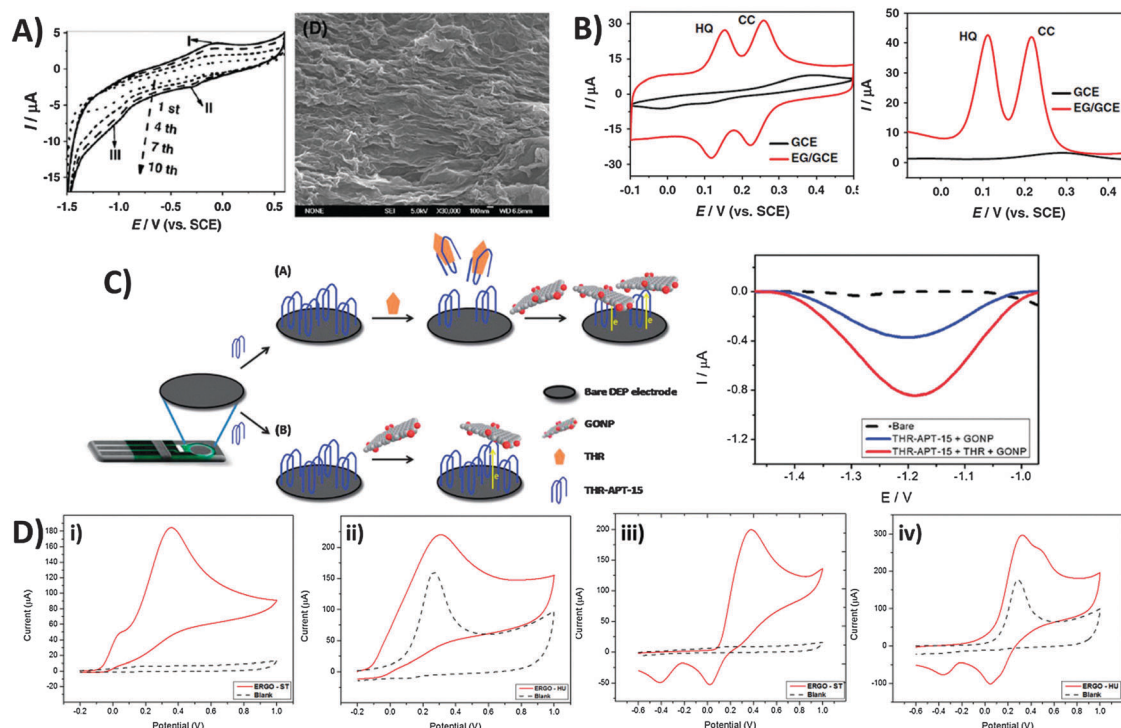
Fig. 6 Employment of inherent GO activity towards film deposition, sensing and its associated limitations. (A) Cyclic voltammogram illustrating electrochemical reduction of GO at 1.0 mg mL^{-1} concentration onto GC electrodes (0.067 M PBS, pH 9.18, scan rate: 10 mV s^{-1}), and the SEM image of the electro-deposited graphene film. (B) Cyclic voltammetry and differential pulse voltammetry of a mixed sample of hydroquinone (0.2 mM) and catechol (0.2 mM) in 0.2 M acetate buffer (pH 5.8) on bare GC and electro-deposited graphene film. CV parameters: a scan rate of 50 mV s^{-1}; DPV parameters: a scan rate of 4 mV s^{-1}, 50 mV pulse amplitude, and 20 ms pulse width. Reprinted with permission from ref. 42. Copyright (2011) Elsevier. (C) Use of graphene oxide nanoplatelets (GONPs) as electroactive labels for the detection of thrombin (THR). In the presence of THR, the aptamer (THR-APT-15) binds specifically to THR and results in the partial release of immobilized THR-APT-15 from the electrode surface, uncovering larger areas for electron transfer between conjugate GONPs and the electrode. Differential pulse voltammograms of GO reduction in the presence (red) and absence (blue) of THR. Reprinted with permission from ref. 43. Copyright (2013) Royal Society of Chemistry. (D) Inherent activity of permanganate-oxidised GO limits potential window for analyte sensing. Cyclic voltammograms of (i and ii) 10 mM ascorbic acid and (iii and iv) 10 mM dopamine on graphene oxides prepared by the (i and iii) Staudenmaier and (ii and iv) Hummer's methods. Voltammograms in a blank supporting electrolyte (dotted) are shown for comparison. Conditions: 50 mM PBS; pH 7.2; scan rate 100 mV s^{-1}. Reprinted with permission from ref. 44. Copyright (2014) American Chemical Society.

HET rates on the activation potential exists only for the former.[47] In its hydrated form, Fe$^{2+/3+}$ experiences strong interactions specifically with carbonyl groups similar to a chelate, and thus shows faster HET with anodic activation on glassy carbon.[47] However, a similar trend was not observed for GO since additional carbonyl groups cannot be introduced as these can only exist at sheet edges which are likely saturated from the beginning (Fig. 7B). Reduction of GO further removes such edge carbonyls which thus lower the observed HET rate. In comparison, ruthenium hexamine Ru(NH$_3$)$_6$$^{2+/3+}$ is an outer-sphere redox probe due to its surface insensitivity and is only affected by factors such as surface area and the electronic density of states (DOS). It is therefore largely uninfluenced by electrochemical activation. Finally in the case of ascorbic acid (AA), cathodic activation treatment of GO reduced the overpotential for AA oxidation as it removes oxygen moieties that would otherwise experience electrostatic repulsion with the negatively charged AA under neutral pH conditions.

Electrochemical activation has also been used to improve the performance of graphene-based capacitors. There are several reports by Kötz and co-workers who employed GO as a capacitor material.[48] As shown in Fig. 7C, large centimetre-sized GO paper (GOP) can be produced by flow-directed filtration, with subsequent thermal treatment to give partially reduced GO paper (GOPpr). This effectively reduces the inter-layer distance measured by X-ray diffraction. With an electrolyte of TEABF$_4$ in acetonitrile, the authors reported potentials of 1.31 V and −1.13 V vs. carbon for anodic and cathodic activations, respectively. It was particularly noted that anodic activation (Fig. 7D) resulted in an enhanced capacitive discharge of up to 270 F g^{-1} during the discharge sweep at 0.0 V regardless of polarization. Redox peaks were also seen at approximately −1.8 V during initial cathodic sweeps and at 0.7 V with anodic sweeps, but do not contribute to the overall capacitance. Cathodic activation in contrast produced slightly distorted voltammograms with less obvious redox peaks, and a lower specific capacitance of ca. 150 F g^{-1}. Although both activations were said to improve capacitor behavior, anodic activation resulted in a superior enhancement not only due to the different types of intercalated ions but was also proposed to be due to the remaining oxygen functional groups.[48]
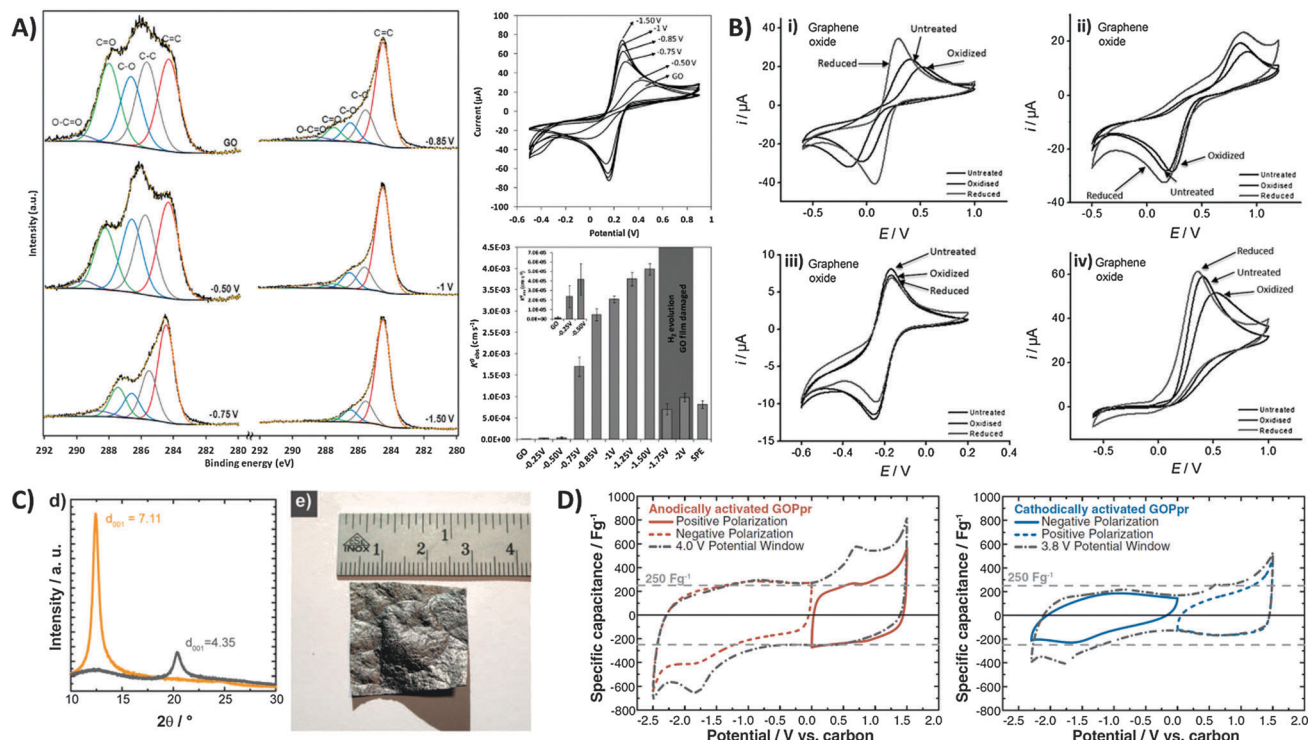
This journal is © The Royal Society of Chemistry 2016

Chem. Soc. Rev., 2016, **45**, 2458–2493 | **2467**

Fig. 7 Electrochemical modification and activation of graphene oxide towards applications. (A) High-resolution carbon-1s XPS spectra of GO-modified screen printed electrodes after application of different potentials for 5 min. Cyclic voltammograms of 5 mM ferro/ferricyanide obtained on GO-modified electrodes after electrochemical treatments at different potentials. Conditions: 0.1 M KCl; scan rate, 0.1 V s^{-1}; potentials are with reference to Ag/AgCl. HET rate constants (k_{obs}^0) calculated from the peak-to-peak separation of ferro/ferricyanide. Inset: enlarged graph of untreated GO film and after application of -0.25 and -0.50 V. Reprinted with permission from ref. 45. Copyright (2013) John Wiley and Sons. (B) Cyclic voltammograms of (i) Fe(CN)$_6^{3-/4-}$, (ii) Fe$^{2+/3+}$, (iii) Ru(NH$_3$)$_6^{2+/3+}$, and (iv) ascorbic acid redox probes on GO after electrochemical oxidation or reduction activation treatments. Scan rate: 100 mV s^{-1}; supporting electrolyte: 50 mM PBS at pH 7.2. Reprinted with permission from ref. 47. Copyright (2012) John Wiley and Sons. (C) XRD spectra of GO paper before (interlayer distance: 7.11 Å) and after (4.35 Å) thermal reduction treatment. Image of a large 7 cm^2 partially-reduced GO membrane. (D) Cyclic voltammograms demonstrating capacitances from positive and negative polarizations, and full sweep of anodically-activated GOPpr (grey dot-dashed line). Negative and positive polarizations, and full sweep of cathodically-activated GOPpr (grey dot-dashed line). Conditions: 1 mV s^{-1} scan rate, 1 M TEABF$_4$ in acetonitrile. Reprinted with permission from ref. 48. Copyright (2013) The Electrochemical Society.

4. Capacitance of graphene

The high conductivity, the exceptional mechanical properties and more importantly its high theoretical specific surface area (SSA) calculated as 2630 m^2 g^{-1} have certainly suggested the use of graphene as an electrode material for the construction of supercapacitors. However, several limitations still impede the full exploitation of all the extraordinary properties of graphene, as a result, leading to a much lower experimentally measured capacitance than expected. One of such limitations is the tendency of graphene sheets to restack after the production reducing significantly the active surface area. A gravimetric capacitance in the order of only tens of F g^{-1} has been measured for a graphene-based electrode which is similar to that obtained using graphite as the electrode material.[49]

Also, it was discovered that the interfacial capacitance measured for both sides of a single graphene sheet is much lower than the one measured on only one side indicating a quantum component in the charge storage mechanism.[50] Both these phenomena make the achievement of the theoretical capacitance value of 550 F g^{-1} for pure graphene[51] extremely hard.

In order to overcome such limitations different strategies have been adopted in the last few years, which can be summarized as follows: production of 3D graphene structures with high conductivity and high surface area, introduction of spacers to avoid graphene re-stacking, introduction of heteroatoms (doping), functionalization of graphene sheets with redox molecules and preparation of graphene composites in combination with other materials.

An activation method using KOH at high concentrations is known to increase significantly the active surface area of carbon materials.[52] Such a procedure was employed in 2011 by Zhu et al. to activate a microwave-exfoliated graphene oxide (MEGO). An extraordinary SSA value of 3100 m^2 g^{-1} and a high conductivity of 500 S m^{-1} were measured for the activated MEGO material which resulted in a capacitance of 166 F g^{-1} in 1-butyl-3-methyl-imidazolium tetrafluoroborate/acetonitrile (BMIM BF$_4$)/AN electrolyte at a current density of up to 5.7 A g^{-1}.[53] A similar activation procedure using KOH was utilized by Ma and coworkers to prepare a graphene-activated carbon composite (GAC) with a high SSA of 798 m^2 g^{-1} giving a capacitance of 122 F g^{-1} in an aqueous electrolyte (6 M KOH).[54] The same group later measured

a SSA of 3523 m^2 g^{-1} for a porous graphene material obtained by hydrothermal synthesis and carbonization of a mixture of GO and carbon sources such as biomass, phenol-formaldehyde (PF), and polyvinyl alcohol (PVA), followed by activation in KOH. Such porous graphene exhibited a high specific capacitance of 202 F g^{-1} in 1 M tetraethylammonium tetrafluoroborate in AN (TEA BF$_4$/AN) and 231 F g^{-1} in 1-ethyl-3-methylimidazolium (EMIM) BF$_4$, electrolyte.[55] Very recently a graphene aerogel has been activated using phosphoric acid and thermal annealing at 800 °C obtaining a porous material of about 1145 m^2 g^{-1} SSA exhibiting a gravimetric capacitance of 204 F g^{-1}.[56] Physical activation was proposed by Yun *et al.* who firstly prepared a trimodal porous graphene structure by self-assembly of graphene sheets, followed by CO$_2$ activation at 900 °C which produced micropores. A SSA of 829 m^2 g^{-1} was measured for this material which gave a capacitance of 278.5 F g^{-1} in an aqueous H$_2$SO$_4$ electrolyte (Fig. 8).[57]

A solution processable holey graphene oxide was easily obtained by heating a GO solution to 100 °C in the presence of H$_2$O$_2$ which, according to authors, etches the oxygenated carbons present on the basal plane. These holey graphene oxide nanosheets have then been processed into reduced porous 3D hydrogels and 2D layered papers with a SSA of 1330 m^2 g^{-1} and 217 m^2 g^{-1}, respectively. Both materials have been tested for capacitors obtaining a gravimetric capacitance of 283 F g^{-1} for the hydrogel and 209 F g^{-1} for the paper at a current density of 1 A g^{-1} in an aqueous electrolyte.[58]

To deal with the tendency of graphene to restack after exfoliation, different spacers have been introduced such as Au nanoparticles[59] and carbon nanotubes (CNTs).[60–66] Interestingly some reports showed a significant increase of capacitance after the preparation of CNT/graphene hybrid materials compared to that of the individual components[60–65] while others demonstrated that the final capacitance corresponded to the average between them.[66] Functionalization of graphene could also be used as methodology to prevent restacking of graphene sheets. Recent studies compared different graphene preparation methods in terms of the capacitance of the resulting materials.[67–69] Chemical, electrochemical or thermal reduction of graphene oxide significantly influences the capacitance of the final graphene material due to the different amount and types of oxygen functionalities. Conductivity is certainly another factor influencing the capacitance and from this study it resulted that the graphene material with the lowest amount of oxygen groups exhibited the largest capacitance due to the superior conductivity of the material.[67–69] Water has also been used as an effective spacer to prevent graphene restacking and fabricate highly porous graphene aerogels. Following a crystallization route which forms ice spacers a free-standing aerogel structure exhibited a capacitance of 172 F g^{-1} at a current density of 1 A g^{-1}.[70,71]

A different approach to improve the capacitive properties of graphene has been the introduction of heteroatoms into the graphene structure. These include nitrogen and boron as the most widely investigated, but also sulfur and phosphorous. It is interesting to notice that both the introduction of nitrogen (n-type electron donating atom)[72–75] and boron (p-type electron withdrawing atom)[76] has resulted in an increased capacitance.
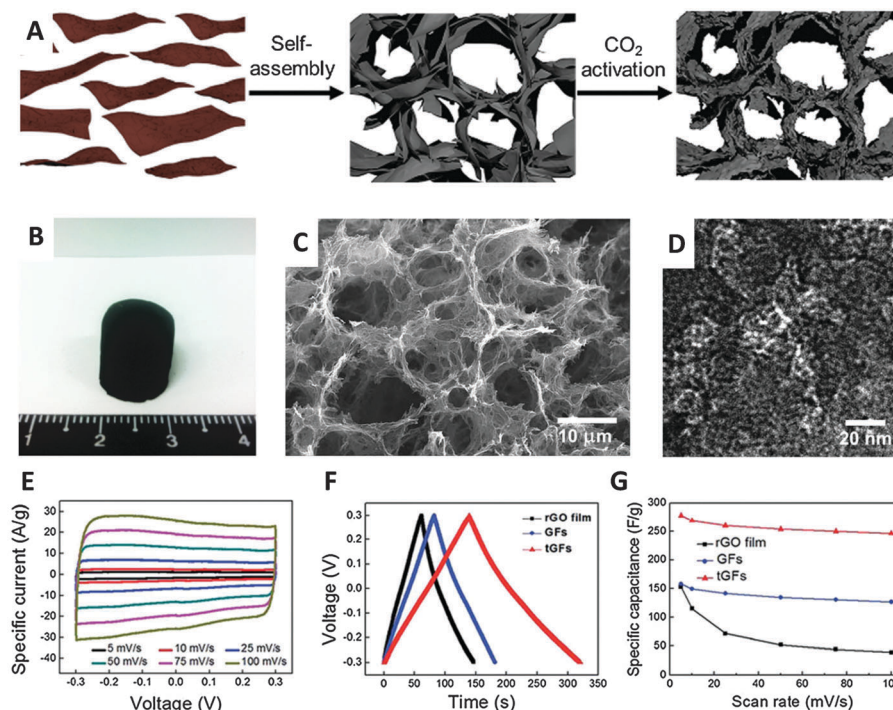

Fig. 8 (A) Schematic illustration of preparation of the tGFs through self-assembly and CO$_2$ activation. (B) Optical image of the resultant tGFs. (C) Low magnification SEM and (D) HR-TEM image of tGFs. (E) CV curves of tGF at the scan rates of 1 to 100 mV s^{-1}. (F) Galvanostatic charge/discharge curve of tGF at 1 A g^{-1}. (G) Rate capability of tGF at a scan rate of 5–100 mV s^{-1}. Reproduced with permission from ref. 57. Copyright (2014) Royal Society of Chemistry.

The mechanism is still not completely clear although with regard to the nitrogen it is believed that the increased capacitance is due to the changes in the electronic structure of graphene which is directly linked to the quantum capacitance.[77] Comparing different boron- and nitrogen-doped graphene materials and after careful chemical and structural characterization, we recently demonstrated that the density of structural defects (edge planes) in the graphene structure represents the dominating factor for the resulting capacitive behavior regardless of the type and amount of doping.[78] Sulfur-doping of graphene resulted in an increased capacitance due to the fact that the sulfur species decreased the ability of graphene to adsorb water, enhancing the electrosorption of the electrolyte ions.[79] Doping carbon materials with phosphorus has been proposed in the past using phosphoric acid as an activation agent during thermal treatment at 800 °C.[80] In this work the authors demonstrated the significant influence of the phosphorous groups on the capacitive behavior of the carbon substrate, which was greatly improved. However, only very recently phosphorus doping has been applied to graphene. In one work, Thirumal *et al.* proposed a simple electrochemical procedure to exfoliate a graphite electrode under anodic conditions in the presence of phosphoric acid. The resulting electrochemically exfoliated graphene presented about 0.7% content of phosphorus in the form of phosphate groups and exhibited a specific capacitance of 290 F g^{-1} at a current density of 0.5 A g^{-1}.[81] Wen and collaborators proposed an annealing procedure in the presence of phosphoric acid to prepare P-doped graphene. The authors obtained a graphene with about 1.3% P content which allowed graphene to be used with a larger potential window of 1.7 V and with great stability. The measured capacitance was found to be 115 F g^{-1} at a current density of 0.05 A g^{-1} in an aqueous sulfuric acid electrolyte.[82]

The graphene materials described so far are able to store electrical charges at the double layer electrode/electrolyte interface, without any faradaic process to occur and therefore are mainly influenced by conductivity and surface area. Another method of electrical storage is the one which exploits redox reactions with also electrons involved. This type of capacitor is based on the so-called pseudocapacitance and since a faradaic process occurs it can store a larger amount of electrical charges. Pseudocapacitors can be obtained by the introduction of redox active molecules and/or materials within a graphene structure. A common combination involves the use of metal oxides or hydroxides with a highly porous graphene. A graphene/Ni(OH)$_2$ nanocomposite has been recently obtained hydrothermally giving a capacitance value of 1212 F g^{-1} and 813 F g^{-1} at a current density of 2 and 16 A g^{-1}, respectively.[83] Graphene oxide decorated with Ni(OH)$_2$ nanoparticles was obtained by the decomposition of Ni(CH$_3$COO)$_2$ at 80 °C followed by hydrothermal treatment resulting in an impressive capacitance of 1335 F g^{-1}.[84] Cobalt oxide/graphene composites have been considered as one of the most promising materials for next-generation supercapacitors. Zhou and collaborators prepared a Co$_3$O$_4$/graphene composite which showed a specific capacitance of 159 F g^{-1} at a scan rate of 5 mV s^{-1}.[85] A 3D Co$_3$O$_4$/graphene aerogel material has been recently fabricated using

hydrothermal synthesis at 180 °C followed by a freeze-drying process. The material showed a capacitance of 660 F g^{-1} at a current density of 0.5 A g^{-1} in an aqueous electrolyte.[86] RuO$_2$ nanoparticles have been grown on the defects of a reduced graphene oxide using the atomic layer deposition (ALD) method. The rGO–RuO$_2$ material showed a specific capacitance of 1132 F g^{-1} at a scan rate of 50 mV s^{-1}.[87] Other studies proposed the combination of graphene with Fe$_2$O$_3$,[88] MnO$_2$,[89,90] V$_2$O$_5$,[91] Fe$_3$O$_4$[92] and SnO$_2$[93,94] among others. Another strategy to enhance the capacitive properties of graphene is to combine it with conducting polymers. Zhang *et al.* fabricated a polyaniline nanofiber/graphene composite which demonstrated a specific capacitance of 480 F g^{-1}.[95] *In situ* anodic electropolymerization (AEP) was used by Wang *et al.* to prepare polyaniline/graphene composite paper (GPCP) material which showed a specific capacitance of 233 F g^{-1} at a scan rate of 2 mV s^{-1} (Fig. 9).[96] Lately similar polyaniline/graphene composites achieved a capacitance of 286 F g^{-1} at 5 mV s^{-1}.[97] In recent years excellent capacitive behavior was obtained by combining graphene with other 2D materials, particularly transition metal dichalcogenides. Firmiano and collaborators deposited by microwave heating layered MoS$_2$ onto reduced graphene oxide (rGO) obtaining a composite material with capacitance as high as 265 F g^{-1} at 10 mV s^{-1} in acidic media.[98] The good capacitive behavior is due to a combined faradaic and non-faradaic capacitive process coupled with the high conductivity of graphene.[98] In another work, MoS$_2$ was firstly obtained by liquid phase exfoliation of bulk MoS$_2$ and then mixed with a dispersion of exfoliated graphene. The MoS$_2$/graphene composite material was assembled as a thin film and produced a capacitance of 11 mF cm^{-2} at a scan rate of 5 mV s^{-1}.[99]

5. Electrochemistry of graphene modified with p-block elements

5.1 Electronic and electrochemical properties

Graphene is a zero-gap semiconductor. Due to the intersecting valence and conduction bands at two inequivalent points, K and K', in the reciprocal space, graphene exhibits excellent conductivity and a distinct electric field effect with high charge concentrations and mobilities.[100,101] Pristine graphene shows a p-type behavior due to the presence of adsorbed oxygen or water on its surface.[102] Doping graphene with p-block elements (*i.e.*, nitrogen, boron, sulfur, hydrogen, oxygen and fluorine) disrupts the planar structure and introduces foreign elements which would alter its electronic properties. Despite that, such modifications have subsequently widened its applications in various technological devices.[103,104]

In the first part of this section, we will discuss the electronic and electrochemical properties of N-doped, B-doped, S-doped, hydrogenated graphene (graphane), hydroxylated graphene (graphol) and fluorinated graphene (fluorographene) (Fig. 10). Following that, the applications of these graphene materials for oxygen reduction and hydrogen evolution reactions would be evaluated. Readers interested in the synthesis methods of these
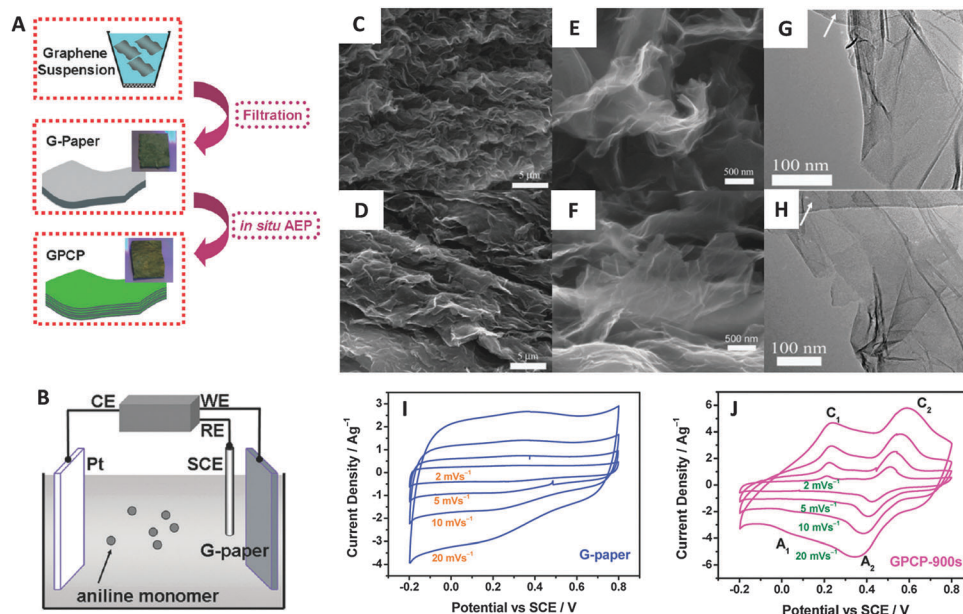
Fig. 9 (A) Illustrative fabrication process toward graphene/polyaniline composite paper (GPCP). (B) Cartoon illustrating the anodic electropolymerization (AEP) of an aniline monomer on G-paper. CE: counter electrode (Pt plate). WE: working electrode (G-paper). RE: reference electrode (SCE). SEM and TEM images of the G-paper (C, E and G) and GPCP-900s (D, F and H). (C and D) Low-magnification SEM images showing the stacked layer-by-layer structure. (E and F) High-magnification SEM images and (G and H) low-magnification TEM images showing the morphology of graphene and graphene/PANi sheets. Arrows in G and H denote the amorphous carbon film deposited on the copper grid. Cyclic voltammograms recorded from 2 to 20 mV s^{-1} in 1 M H$_2$SO$_4$ for (I) G-paper and (J) GPCP. Reproduced with permission from ref. 96. Copyright (2009) American Chemical Society.
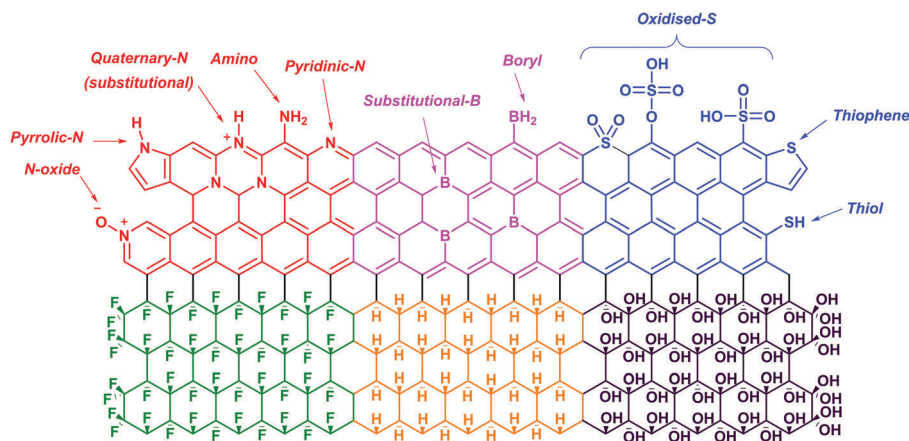

Fig. 10 Illustrations of the structures of N-doped (red), B-doped (pink), S-doped (blue), fluorinated (green), hydrogenated (yellow) and hydroxylated (purple) graphene.

graphene materials are directed to several review articles available in the literature.[105–108]

Based on the nature of the substitutionally-doped p-block elements (*i.e.*, carbon atoms in the graphene lattice is replaced by dopants), which could be electron-withdrawing or donating, the electronic properties of the resulting graphene materials would vary. Additional effects from additive dopants (*i.e.*, the graphene lattice is functionalized and resulted in the conversion of sp^2- to sp^3-hybridized carbon atoms) or topological defects could introduce more variables into the electronic properties. More often than not, such modifications vary the density of state (DOS) near the Fermi energy (F_m) level and thus

also the conductivities of the doped graphene materials. In electrochemistry, as electron transfer does not generally occur between an electrode and redox systems with E° values lying in the band gap region, the electrochemical properties of the doped graphene materials would differ greatly among themselves.[109]

5.1.1 Nitrogen-doped graphene. One of the earliest attempts to dope graphene was to introduce nitrogen atoms into the graphene lattice. Nitrogen doping of graphene typically incorporates nitrogen moieties such as pyridinic-N, pyrrolic-N, quaternary-N, amino and N-oxide. Among these nitrogen moieties, quaternary-N is introduced *via* substitutional doping whereby carbon atoms in the graphene lattice are replaced by nitrogen atoms. The remaining nitrogen

moieties are usually introduced at the edges or defects of graphene either *via* substitutional doping or addition reaction. Substitutional nitrogen doping suppresses the DOS of graphene near the F_m level and leads to band gap opening. Moreover, substitutional nitrogen dopants introduce strong electron donor states near the F_m level resulting in n-type semiconductor behavior. The carrier mobilities and conductivity of N-doped graphene are lower than pristine graphene since the presence of nitrogen dopants and topological defects introduced during the doping process could function as scattering centres that hinder the hole/electron transport.[110] On the other hand, the presence of the amino moiety increases the work function, as opposed to the effect of substitutional doping.[111] When applied as a transducer in an electrochemical glucose biosensor by Lin and co-workers, excellent selectivity and sensitivity for the reduction of hydrogen peroxide (H_2O_2) were observed (Fig. 11a).[112] Moreover, a high heterogeneous electron transfer (HET) rate on N-doped graphene toward $Co(bpy)_3^{3+/2+}$ and $Fe(CN)_6^{3-/4-}$ was previously reported.[113,114]

5.1.2 Boron-doped graphene. Doping graphene with boron, which is a common p-type dopant, is also highly favourable. Boron dopants introduce more holes into the valence band of graphene resulting in a high carrier concentration. Such B-doped graphene has high conductivity, in comparison to both N-doped graphene[114] and pristine graphene[115] (Fig. 11b), due to the large DOS near the F_m level. Substitutional doping of boron is

thermodynamically more favoured than addition reaction ($-BH_2$) due to the retention of aromaticity in the graphene lattice after doping and the avoidance of undesirable "deformational energy" upon conversion of carbon atoms from sp^3 to sp^2 hybridisation.[111] Similar to NH_2-rich N-doped graphene, the presence of the $-BH_2$ moiety in B-doped graphene increases the work function, resulting in a p-type semiconductor behavior.[111] Electrodes coated with B-doped graphene showed improved resistance to electrode fouling compared to un-doped graphene materials, especially for the electrochemical analysis of biomarkers.[116]

5.1.3 Sulfur-doped graphene. Doping sulfur in graphene is more challenging due to the large size of the sulfur atom. Early theoretical studies indicated the possibility to substitutionally dope graphene with sulfur and also to apply the S-doped graphene as a gas sensor since the absorption of NO_2 molecules can increase the DOS at the F_m level.[117,118] Further first principles calculations showed that the structural modifications induced by substitutional doping of sulfur could influence the DOS, thus resulting in the formation of a band gap or improving the metallic properties of S-doped graphene.[119,120] S-doped graphene has been shown to constitute predominantly sulfide (thiophene), sulfate and sulfonate groups.[121–123] The resistivity of sulfonate-rich S-doped graphene correlated positively with the extent of doping.[122] On the other hand, thiophene-rich S-doped graphene demonstrated high sensitivity and selectivity as well as an improved electrocatalytic effect over reduced graphene oxide for the reduction of H_2O_2, due to the better conductivity/charge transfer and creation of active sites as a result of sulfur doping.[123] Moreover, thiophene-rich S-doped graphene was also successfully applied for selective and sensitive detection of dopamine (Fig. 11c).[124]

5.1.4 Hydrogenated graphene (graphane). A fully hydrogenated graphene is termed graphane and exists as a puckered structure. Graphane should theoretically consist entirely of sp^3-hybridised carbon atoms existing in either the chair- or boat-like conformation, in contrast to graphene which is made up of layered sp^2-hybridised carbon atoms. By controlling the extent of hydrogenation, the band gap of graphene can be tuned to achieve semiconducting properties. Theoretical studies have indicated the highest possible theoretical band gap of 3.7 eV for pristine graphane.[125] The electrochemical properties of hydrogenated graphene are governed by the degree of hydrogenation. Less hydrogenated graphene (~ 3.5 at%) suffered from a low HET rate toward $Fe(CN)_6^{3-/4-}$, while highly hydrogenated graphene (~ 19 at%) showed an improvement in the HET rate.[126] Despite that, the measured HET rate could be a result of competing influences such as edge effects, which promote electron transfer. Nevertheless, hydrogenated graphene has been successfully applied for the electrochemical detection of biomarkers such as ascorbic acid, uric acid and dopamine.[127] However, it was not beneficial for the detection of nitroaromatic compounds such as trinitrotoluene (TNT).[128] The lack of sp^2 hybridisation on the hydrogenated graphene could have possibly reduced the extent of π–π interaction between the graphene material and TNT, thus resulting in a lower degree of absorption of TNT prior to electrochemical detection.
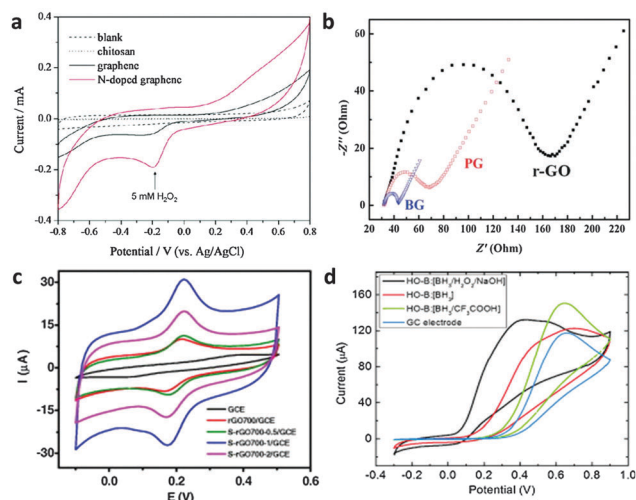

Fig. 11 (a) Cyclic voltammograms of 5 mM H_2O_2 in N_2-saturated 100 mM PBS (pH 7.0) on the chitosan electrode (dotted line), the graphene electrode (black line), and the N-doped graphene electrode (red line). Adapted with permission from ref. 112. Copyright (2010) American Chemical Society. (b) The typical electrochemical Nyquist plots of the reduced-GO (r-GO), pristine graphene (PG) and B-doped graphene electrodes. Adapted with permission from ref. 115. Copyright (2011) Royal Society of Chemistry. (c) CVs of GCE, rGO700/GCE, S-rGO700-0.5/GCE, S-rGO700-1/GCE and S-rGO700-2/GCE in 0.5 mM DA (200 mM PBD, pH 6.0) at a scan rate of 50 mV s^{-1}. Adapted with permission from ref. 124. Copyright (2015) Elsevier. (d) Cyclic voltammetry of ascorbic acid (10 mM) in 50 mM PBS buffer (pH 7.0) at the HO-B:[$BH_3/H_2O_2/NaOH$] ($C_1O_{0.78}H_{0.75}$)$_n$ electrode. Adapted with permission from ref. 133. Copyright (2015) John Wiley and Sons.

2472 | *Chem. Soc. Rev.*, 2016, **45**, 2458–2493

This journal is © The Royal Society of Chemistry 2016

5.1.5 Fluorinated graphene (fluorographene). Fluorine is the most electronegative element based on the Pauling scale, resulting in the strong bonding between carbon and fluorine. Similar to the hydrogenation process on graphene, fluorination of graphene would convert the carbon atoms from sp^2 to sp^3 hybridisation. Such modifications would inevitably affect the electronic properties and local structure of graphene. In fact, a fully fluorinated graphene, typically termed fluorographene, behaves similarly to an insulator with a band gap $E_g \geq 3.0$ eV and charge carrier mobility that is 3 orders of magnitude smaller than graphene.[129] Several studies have explored the electrochemistry of non-stoichiometry fluorinated graphene. Electrochemical studies have shown that the HET rate would improve by increasing the extent of fluorination on graphene.[130,131] However, as the synthesis methods of fluorinated graphene tend to introduce additional defects on graphene, the competing influences of edge effects on the HET rate of fluorinated graphene should be noted. Moreover, fluorinated graphene exhibited electrocatalytic properties toward the detection of biomarkers such as ascorbic acid, dopamine and uric acid.[131]

5.1.6 Hydroxylated graphene (graphol). A fully hydroxylated graphene is termed graphol. To date, not only has graphol not been experimentally synthesized, but theoretical studies on this material have also been limited. Nevertheless, hydroxylated graphene has been experimentally synthesized based on the conversion of fluorinated graphene to hydroxylated graphene and the hydroboration of graphene oxide with subsequent oxidation.[132,133] As of now, in terms of electrochemistry, highly hydroxylated graphene with a stoichiometry of $(C_1O_{0.78}H_{0.75})_n$ has shown favourable electrocatalytic properties toward the oxidation of ascorbic acid (Fig. 11d).[133]
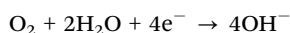
5.2 Oxygen reduction reaction

The oxygen reduction reaction (ORR) is a critical reaction in fuel cells and air–zinc batteries. Unfortunately, the slow kinetics of ORR at the cathode sides of fuel cells, which are typically composed of platinum-based catalysts, has hindered the practical application of this technology. Given the high cost and sensitivity of platinum to CO poisoning and methanol crossover, carbon-based catalysts especially doped graphene materials are vigorously explored as inexpensive and robust alternative electrocatalysts. While doping can modify the electronic and chemical properties of graphene to improve O_2 reduction, the ORR performances of the doped graphene materials, in most cases, exceed that of platinum electrocatalysts only in alkaline solutions.
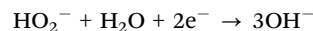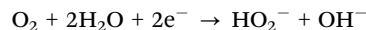
In alkaline (and acidic) solutions, oxygen reduction can proceed by either a two- or four-electron pathway (shown below). Pure carbon-based materials typically catalyse ORR reaction through the two-electron pathway, which involves the formation of a metastable intermediate H_2O_2. However, doped-graphene materials are expected to proceed *via* the four-electron pathway, in both alkaline and acidic solutions.

(A) Alkaline solutions
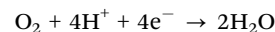(a) Direct four-electron pathway:

$$O_2 + 2H_2O + 4e^- \rightarrow 4OH^-$$

(b) Two-step two-electron pathway through peroxide formation:

$$O_2 + 2H_2O + 2e^- \rightarrow HO_2^- + OH^-$$

$$HO_2^- + H_2O + 2e^- \rightarrow 3OH^-$$

(B) Acidic solutions
(a) Direct four-electron pathway:

$$O_2 + 4H^+ + 4e^- \rightarrow 2H_2O$$

(b) Two-step two-electron pathway through peroxide formation:

$$O_2 + 2H^+ + 2e^- \rightarrow H_2O_2$$

$$H_2O_2 + 2H^+ + 2e^- \rightarrow H_2O$$

Despite understanding the basic mechanism of ORR, further enhancement of the catalytic activity of doped graphene materials can only be achieved by contemplating on the structure of the electrocatalysts and catalytic active sites. Recent advances have ventured into three-dimensional (3D) graphene materials as such electrocatalysts can provide high specific surface areas, strong mechanical strength as well as fast mass and electron transport kinetics due to the combination of 3D porous structures and the excellent intrinsic properties of graphene materials.[134] Further dual- and tri-doped graphene materials have been introduced to exploit the benefits of each type of dopant for oxygen reduction.[108] These would, however, not be covered in this review.

On top of all these, the presence of metallic impurities in doped graphene materials should not be overlooked. Most graphene materials derived from graphite oxide are contaminated with a considerable amount of metallic impurities.[135–137] It has previously been shown that manganese-based impurities, which are usually introduced in excess during oxidation of graphite using Hummer's oxidation method, are able to catalyse oxygen reduction.[138] As a result, the electrocatalytic effects observed for oxygen reduction could be mistakenly assigned as the inherent performance of graphene materials. Readers are thus cautioned on the possibilities of manganese-based impurities masking the actual electrocatalytic effect of doped-graphene materials.

5.2.1 Nitrogen-doped graphene. N-doped graphene is currently the most researched among graphene materials for oxygen reduction. As aforementioned, nitrogen doping of graphene incorporates pyridinic-N, pyrrolic-N, quaternary-N, amino and N-oxide moieties into the graphene lattice. Moreover, excellent ORR activity was achieved with even a low doping level of 2.8%.[139]

The electronegative nitrogen atoms are capable of inducing charge polarisation on the surrounding carbon atoms resulting in positively charged carbon centres. Such high spin density and hybridization freedom on carbon atoms are deduced to improve the adsorption of oxygen molecules on N-doped

This journal is © The Royal Society of Chemistry 2016

Chem. Soc. Rev., 2016, **45**, 2458–2493 | **2473**

graphene resulting from charge transfer, which is a critical step for ORR activity. In fact, density functional theory (DFT) studies highlighted that the bonding interactions between oxygen and N-doped graphene grew stronger with increasing concentration of nitrogen, whereby the endothermicity of oxygen adsorption became exothermic.[140]

Although energy separation between the highest occupied molecular orbital (HOMO) and the lowest unoccupied molecular orbital (LUMO) was expected to function as a simple indicator of the kinetic stability and chemical reactivity for ORR activity, it fell-short as a conclusive indicator. In fact, the availability of catalytic active sites on N-doped graphene is determined by the spin density distribution and atomic charge distribution.[141]

On the other hand, pyridinic-N and quaternary-N moieties were determined as the catalytic active sites of N-doped graphene for ORR.[142] Ruoff and co-workers have concluded that the electrocatalytic activity of N-doped graphene is dependent on the presence of these two nitrogen moieties, whereby the quaternary-N determines the limiting current density, while the pyridinic-N improves the onset potential for ORR.[143] A further study by Murakoshi highlighted that the quaternary-N reduces oxygen *via* a two-electron pathway while pyridinic-N reduces oxygen *via* a four-electron pathway, in alkaline solutions (Fig. 12). The determination of active ORR catalytic sites in N-doped graphene

Fig. 12 (a) Selective nitrogen doping in graphene. (b) N1s spectra of Py-NG and Ju-NG. (c) RDE voltammetry curves for oxygen reduction on pristine graphene, Ju-NG, and Py-NG in an O_2-saturated 0.1 M KOH solution. The electrode rotating rate and scan rate was 625 rpm and 0.01 V s^{-1}, respectively. Reproduced with permission from ref. 146. Copyright (2013) Royal Society of Chemistry.

has, as such, spurred further research in the synthesis of pyridinic-N-rich graphene materials.[144,145]

5.2.2 Boron-doped graphene. The introduction of boron, which is less electronegative than carbon, modifies the electronic properties of graphene. Due to electronegativity differences, the positive charge is localized on boron. Moreover, boron functions as the main catalytic active site for oxygen adsorption. Further DFT studies have shown that the local high spin density in B-doped graphene facilitates the adsorption of oxygen and OOH leading to favourable oxygen reduction activity.[147] B-doped graphene has been applied for ORR in alkaline solutions and demonstrated excellent electrocatalytic activity as well as long term stability and good CO tolerance. In accordance to theory whereby reduction reactions have become more difficult in electron-deficient materials,[148] experimental investigations have determined that a higher content of boron increases the resistivity and lowers the ORR activity in alkaline solutions.[149]

5.2.3 Sulfur-doped graphene. S-doped graphene can function as a versatile electrocatalyst for oxygen reduction as well. Despite the similarity in electronegativity between sulfur and carbon, the ORR mechanism on S-doped graphene could differ. Recent DFT studies showed that the catalytic active sites are located along the zig-zag edges or the neighbouring carbon atoms of oxidised sulfur moieties, which possess large spin or charge density. Furthermore, substitutional sulfur atoms with high charge density catalyzed oxygen reduction *via* a two-electron pathway while carbon atoms with high spin or charge density followed a four-electron pathway. Furthermore, S-doped graphene was calculated to exhibit comparable catalytic properties to platinum and N-doped graphene.[150] Experimental results showed that S-doped graphene demonstrated a similar ORR onset potential and higher current density in comparison to the Pt/C electrocatalyst.[121] Moreover, S-doped graphene exhibited superior durability and tolerance to methanol crossover effects.[121,151]

5.3 Hydrogen evolution reaction

The hydrogen evolution reaction (HER) is another important energy reaction of interest. It occurs in the cathodic side of electrolyser systems which provides a clean supply of hydrogen gas for fuel cells, without any carbon emissions. Similar to ORR, HER has thermodynamic and kinetic constraints; the kinetic constraints are typically resolved by using efficient platinum-based electrocatalysts. However, their high cost and limited abundance hinder their widespread practical implementation. To improve cost-competitiveness, it is critical to develop alternative efficient HER electrocatalysts based on earth-abundant elements. Previously, the search had mainly revolved around non-noble metal-based materials (*i.e.*, Mo, W, Ni, Fe). However, recently, the research community has witnessed numerous carbon-based electrocatalysts reported with good HER activities. Compared to non-noble metals, carbon-based materials are generally cheaper, more abundant, and less susceptible to corrosion and oxidation. For these reasons, they are attractive as possible alternative HER electrocatalysts. In particular, doped graphene and related materials have been developed
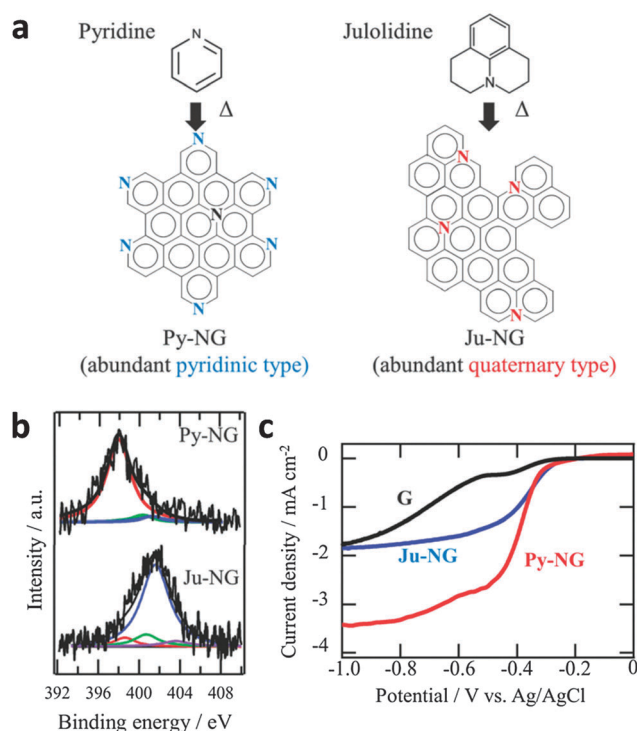
2474 | *Chem. Soc. Rev.*, 2016, **45**, 2458–2493

This journal is © The Royal Society of Chemistry 2016

with promising HER performances close to that reported for platinum in acidic media.

HER occurs *via* a two-electron pathway ($2H^+ + 2e^- \rightarrow H_2$). It is generally accepted to involve two steps; namely electrochemical hydrogen adsorption (Volmer step) and desorption which can occur either electrochemically (Heyrovský step) or chemically (Tafel step).[152–155] In the Volmer step, a proton and an electron combine to produce adsorbed hydrogen (H*) on the active site of the electrocatalyst surface (M). Subsequently, the reaction can proceed by either the Heyrovský or Tafel step.[152] In the Heyrovský step, adsorbed hydrogen merges with a proton in the presence of an electron to produce hydrogen gas, whereas in the Tafel step, two adsorbed hydrogen atoms combine for hydrogen gas formation. Since H* is present regardless which route is followed, the Gibbs free energy of hydrogen adsorption (ΔG_{H*}) greatly influences the overall rate of reaction and is often described as the main criterion for assessment of the process. Optimal HER electrocatalysts, such as platinum, have ΔG_{H*} close to zero which indicates that H* binds neither too strongly (when ΔG_{H*} is largely negative) nor too weakly (when ΔG_{H*} is largely positive) onto the electrocatalyst surface.[156]

In order to determine which pathway the HER process proceeds after the first step of electrochemical hydrogen adsorption, a Tafel plot obtained from the HER polarization curve can be used.[157] The Tafel plot relates the overpotential (η) as a function of logarithm of current density (j). By fitting the linear portion of the graph to the Tafel equation ($\eta = b \log j + a$), the Tafel slope value can be obtained from the value 'b'. Tafel slope values close to 40 mV per decade (mV dec^{-1}) indicate that the Heyrovský step is the rate-determining step (RDS), while values close to 30 mV dec^{-1} suggest that the Tafel step is the RDS. From here, we can propose whether the reaction pathway proceeded through the electrochemical desorption or the chemical desorption process. In fact, Tafel slope is an inherent property of a material. For Pt, its Tafel slope value is measured to be 30 mV dec^{-1} [155] which shows that it catalyses HER *via* the Volmer–Tafel pathway, with the Tafel step being the RDS.

Besides acidic media, HER can also be performed under alkaline conditions ($2H_2O + 2e^- \rightleftharpoons H_2 + 2OH^-$) in electrolyser systems. However, comparing acidic and alkaline electrolysers, the former is generally more superior to the latter in terms of industrial operation.[153] This could be due to an additional water dissociation step required for hydrogen generation under basic conditions, which increases the energy requirement of the process.[155] A summary and comparison of the HER mechanism in acidic and basic media is presented in Table 1.

In the pursuit of finding alternative HER electrocatalysts to replace Pt, numerous theoretical studies based on the established

mechanisms behind HER have been subsequently conducted. With the possible tailoring of the electronic and electrochemical properties of graphene through doping, computational studies predicted that doping graphene materials with p-block elements can successfully tailor the ΔG_{H*} to enhance their HER activities.[158] Qiao's group presented one of the earliest explorations on density functional theory (DFT) calculations of doped graphene materials for HER applications.[158] They showed that the presence of a p-block element dopant can produce noticeable differences in the charge population of adjacent carbon atoms to tune their electron donor–acceptor properties for different H* adsorption behaviors. Using molecular orbital theory, they proposed that the lowest valence orbital of the activated carbon atom hybridizes with the bonding orbital of the adsorbed H* to form bonding and antibonding states. With lower and more stable valence-band energy levels, a stronger bonding between H* and the active carbon can be achieved for a reduced ΔG_{H*}. Indeed, experimentally, there have been several reports where p-block element doped graphene materials show enhanced HER electrocatalysis compared to their undoped counterparts.[158–160]

However, the sole presence of a dopant in graphene materials is often insufficient to compete with the performances of state-of-the-art metal HER electrocatalysts. As such, various strategies have been explored to further improve the catalytic activity of doped graphene materials for hydrogen generation. Here, we review such strategies investigated. Even though some of these novel HER electrocatalysts may be presented as metal-free, readers are cautioned that there may be traces of metallic impurities in the graphene materials which can arise from the starting material or preparation method that could play a role in altering their electrochemical properties. As a parameter of comparison among reported electrocatalysts, overpotential at a current density of -10 mA cm^{-2} is commonly used.[153] To provide a general overview, Pt-based electrocatalysts exhibit excellent activity with almost zero overpotential, while many state-of-the-art metal-based HER electrocatalysts require between 100 to 200 mV to reach this current density.[153] Unless otherwise stated, the term 'overpotential' used subsequently here refers to the overpotential required to achieve a current density of -10 mA cm^{-2}. Besides overpotential and Tafel slope, other parameters frequently reported to characterize HER catalyst materials include onset potential, exchange current density and turnover frequency. However, for simplicity, overpotential and Tafel slope are chosen as the more relevant aspects of HER activity for comparison in our discussion here. Readers interested to know more about the other parameters of HER performance can refer to ref. 153 and 154. Since most of the HER experiments reported are conducted under acidic conditions (0.5 M H_2SO_4),

Table 1 HER mechanism in acidic and basic media

Reaction pathway	Acidic media	Basic media	Tafel slope (mV dec^{-1})
Volmer step	$M + H^+ + e^- \rightleftharpoons M - H*$	$M + H_2O + e^- \rightleftharpoons M - H* + OH^-$	120
Heyrovský step	$M - H* + H^+ + e^- \rightleftharpoons M + H_2$	$M - H* + H_2O + e^- \rightleftharpoons M + H_2 + OH^-$	40
Tafel step	$2(M - H*) \rightleftharpoons H_2 + 2M$	$2(M - H*) \rightleftharpoons H_2 + 2M$	30
Overall:	$2H^+ + 2e^- \rightleftharpoons H_2$	$2H_2O + 2e^- \rightleftharpoons H_2 + 2OH^-$	—

the performances depicted that follows would refer to acidic conditions unless otherwise stated. For ease of comparison, the main details of various reports to be presented below on doped graphene and their related materials for HER applications are summarized in Table 2.

5.3.1 p-block element-doped graphene. Doping graphene with p- or n-type dopants can produce contrasting electronic effects. p-doping typically displays improved cathodic electrocatalysis while n-doping often shows enhanced anodic electrocatalysis.[161] Therefore, in the case of HER whereby it is based on cathodic electrocatalysis, n-type doping is often preferred.[158,160,162] This is indeed proven experimentally with numerous reports of N-doped graphene (n-type doping) dominating the field of doped graphene materials for HER catalysis (Table 2). This is possibly

due to good tailoring abilities of the inherent pyridinic-N and graphitic-N moieties to activate the adjacent carbon atom for a reduced ΔG_{H^*}, as suggested from DFT calculations by Qiao's group.[158]

Even though p-type doping of graphene is usually not preferred for HER catalysis, Asefa and co-workers reported the use of B-doped graphene (p-type doping) material for this application.[159] They explored different borylating agents (*i.e.*, carborane, $B(OH)_3$, $NaBH_4$, and BH_3-THF) on defective graphene and found that BH_3-THF-treated graphene (1.85 at% B) achieved HER performance with a Tafel slope of ~ 99 mV dec^{-1}, indicating a Volmer-limiting step, and an overpotential of ~ 440 mV.[159] Compared to its undoped counterpart, there was ~ 60 mV upshift in overpotential. Such observation, where p-type doping

Table 2 Summary of doped graphene and related materials reported for HER applications

Electrocatalyst	Remarks (*e.g.* dopant amounts, surface area, particle size, *etc.*)	Overpotential at −10 mA cm^{-2} current density (mV)	Tafel slope (mV dec^{-1})	Ref.
Under acidic conditions (0.5 M H$_2$SO$_4$)				
p-block element doped graphene				
B-doped graphene	1.85 at% B	$\sim 440^b$	~ 99	159
N-doped mesoporous graphene	3.93 at% N, 927 m^2 g^{-1}	$\sim 245^b$	~ 109	162
N,P-codoped graphene	4.60 at% N, 1.63 at% P	~ 420	~ 91	158
N,S-codoped nanoporous graphene	5.06 at% S, 3.79 at% N, 0.07 at% Ni, 1320 m^2 g^{-1}	~ 280	~ 81	160
Highly N,P-dual doped multilayer nanoporous graphene	3 at% P, 11 at% N, 1102.1 m^2 g^{-1}	~ 213	~ 79	165
Doped graphene with carbon nitride				
C$_3$N$_4$@N-doped graphene hybrid	33 wt% g-C$_3$N$_4$	~ 240	~ 52	170
Porous C$_3$N$_4$ nanolayers@N-doped graphene films after 750 CV cycles	4.6 wt% N, 9.1% PCN nanolayers, 58 m^2 g^{-1}	~ 80	~ 49	171
N,P-doped nanoporous graphene/g-C$_3$N$_4$ hybrid	2.14 at% P, 42.08 at% N (from C$_3$N$_4$ and N-graphene), 119 m^2 g^{-1}	~ 340	~ 90	166
Doped graphene with metal-based materials				
Molybdenum sulfide clusters-N-doped graphene hybrid hydrogel film	2.1 wt% MoS$_x$	~ 140	~ 105	173
N-doped graphene decorated by few-layer MoS$_2$	45.1 wt% MoS$_x$, 2.01 at% N	$\sim 160^b$	~ 45	178
WS$_2$ nanolayers@heteroatom-doped graphene	3.36 at% N, 9.73 at% O, 0.63 at% P, 20 wt% WS$_2$	~ 125	~ 53	167
Nanostructured SnS-N-doped graphene	2.15 at% N, 17.31 at% S, 17.28 at% Sn	~ 125	~ 38	180
Atomic cobalt on N-doped graphene	8.5 at% N, 0.57 at% Co	~ 147	~ 82	181
N-doped carbon-wrapped Co nanoparticles on N-doped graphene nanosheets	7.5 at% N, 0.48 at% Co	$\sim 190^b$	~ 80	184
Co embedded in N-doped carbon	2.8 at% N, nanoparticle size: <10 nm	~ 265	~ 98	182
N-doped graphene/Co-embedded porous carbon polyhedron hybrid	3.5 at% N, ~ 0.5 at% Co on surface, 375 m^2 g^{-1}	~ 229	~ 126	183
S-doped graphene with carbon black and Ru nanoparticles	4.45 at% S, 0.75 at% Ru, 20% carbon black	$\sim 70^b$	~ 61	169
3D N-doped graphene supported MoS$_2$ nanoparticles	5.4 wt% N, 3.53 wt% S, 5.39 wt% Mo, 1066.6 m^2 g^{-1}, graphene thickness: ~ 0.34 nm, MoS$_2$ lateral size: ~ 35 nm	$\sim 290^b$	~ 44	179
Co nanoparticles at N-doped graphene with porous structure	4.9 at% N, 0.8 at% Co, 104.5 m^2 g^{-1}, pore size: 10 to >100 nm	~ 125	~ 94	185
Ultrathin N-doped graphene shells encapsulate CoNi nanoalloy^a	1.8 at% N, 12.2 at% Co, 9.9 at% Ni, 1 to 3 graphene layers per shell, nanoalloy size: 4 to 7 nm, 5 wt equivalent mass loadings used	~ 142	~ 105	186
Under basic conditions (0.1 M KOH)				
P,N-codoped graphene	4.60 at% N, 1.63 at% P	$\sim 585^c$	~ 145	158
Co embedded in N-doped carbon	2.8 at% N, nanoparticle size: <10 nm	~ 337	Not mentioned	182

^{a} HER experiment was conducted in 0.1 M H$_2$SO$_4$. ^{b} The overpotential at a current density of −10 mA cm^{-2} was not mentioned, but approximated from the polarization curve. ^{c} The overpotential at a current density of −10 mA cm^{-2} was not mentioned, but the overpotential at a current density of −5 mA cm^{-2} was approximated from the polarization curve.

shows a similar catalytic effect to n-type doping, could be attributed to variations in the doping mechanism (*i.e.*, addition instead of substitution) as suggested from computational studies by Lazar *et al.*[161]

Similar to ORR, the strategy of dual-doping was investigated to further enhance the catalytic performance of doped graphene. From DFT calculations of various single- and dual-doped graphenes, Qiao and co-workers predicted that dual-doped graphene would show higher HER activity compared to single-doped graphene. Their calculations revealed pyridinic-N and P dual-doped graphene to have the best HER performance among the different possible electrocatalysts studied, as it yielded the lowest ΔG_{H*} value of 0.08 eV.[158] This was further supported experimentally with N,P-codoped graphene (N,P-graphene-1), containing 4.60 at% N and 1.63 at% P, showing improved HER catalytic performance as compared to its single-doped graphene counterparts (Fig. 13). Additionally, the electrocatalyst was tested under alkaline conditions (0.1 M KOH) to demonstrate the stability of doped graphene materials over a wide range of pH. By qualitatively evaluating the number of active sites derived from Tafel plots, the group found that the enhancement seen in N,P-graphene was not merely due to a simple increase in the number of active sites. Instead, it was evidence for a synergistic coupling effect arising from the dual-doping of N and P. As suggested from a study by Woo and co-workers,[163] the co-doping of P could promote preferential bonding of pyridinic-N to induce this synergistic effect.[164] This finding has also been experimentally observed by several other studies.[165–167] Interestingly, Qiao's group also found that random coupling of heteroatoms (*i.e.*, B,N-graphene) could not produce such an effect. This highlights the importance of N and P co-doping in graphene for improved HER catalysis.

From the predicted value of ΔG_{H*} of the co-doped graphene material, one would expect a better HER performance for the material. However, in experimental studies, this could have been impeded due to strong π–π interactions and/or hydrophobic affinities between graphene layers leading to restacking and agglomeration during the electrode drying process. To overcome this, porous structures of doped graphene have been investigated as one possible solution.

Wang's group developed N-doped mesoporous graphene using micelle-template synthesis and compared its HER performance with its 2D graphene counterpart.[162] The group found that porous architecture greatly increased the specific surface area (by over five times), thereby effectively accelerating the HER catalysis to achieve $\sim$245 mV overpotential from over 400 mV in N-doped graphene.

Chen and co-workers combined these strategies of dual-doping and porous structures to further enhance the HER performances of doped graphene materials.[160] N and S co-doped graphene was grown on nanoporous Ni by the chemical vapour deposition method. The Ni template was then etched away to yield nanoporous dual-doped graphene. With an overpotential of $\sim$280 mV and a Tafel slope of $\sim$80.5 mV dec^{-1}, the electrocatalyst displayed superior HER activity over its undoped and single-doped counterparts. The co-doping of S could have promoted the formation of graphitic-N to result in the observed synergistic effect.[164] The group also studied the effect of different CVD synthesis temperatures (500 and 800 °C) and found that a lower temperature produced more favourable bonding configurations (*i.e.*, C–S–C–, –C=S–) for HER. From XPS analysis, the group found that 4 to 6 at% of –C–S–C– and –C=S– were converted to –C–SO$_2$– upon 1000 HER cycles, suggesting that these bonding types could be responsible for the observed HER catalysis. Moreover, the group found residual amounts of Ni ($<$0.07 at%) which could have also contributed to its HER activity.

Besides designing porous structures, inserting carbon black particles in between graphene layers was successfully investigated as an alternative solution to prevent restacking of graphene.[168] Shervedani and Amini reported S-doped graphene showing improvements in HER performance after the treatment with carbon black (20%).[169]

5.3.2 Doped graphene hybrids. Even though doping graphene with p-block element(s) can enhance its HER activity, their performances are generally poorer as compared to many state-of-the-art metal-based HER electrocatalysts (Table 2). In order to further improve their HER performances, the idea of hybrid formation was exploited as an important strategy. In particular, hybrid materials containing doped graphene and other carbon-based (*e.g.* carbon nitride) or metal-based materials (*e.g.* WS$_2$, MoS$_2$, SnS, Co) have been recently reported.

5.3.2.1 Doped graphene with carbon nitride. Qiao's group coupled graphitic-carbon nitride (g-C$_3$N$_4$) with N-doped graphene (N-graphene; NG) to form a hybrid (C$_3$N$_4$@NG).[170] Various proportions of C$_3$N$_4$ were investigated and 33 wt% was found to produce the optimum HER performance. C$_3$N$_4$@NG showed an overpotential of $\sim$240 mV and a Tafel slope of $\sim$51.5 mV dec^{-1},
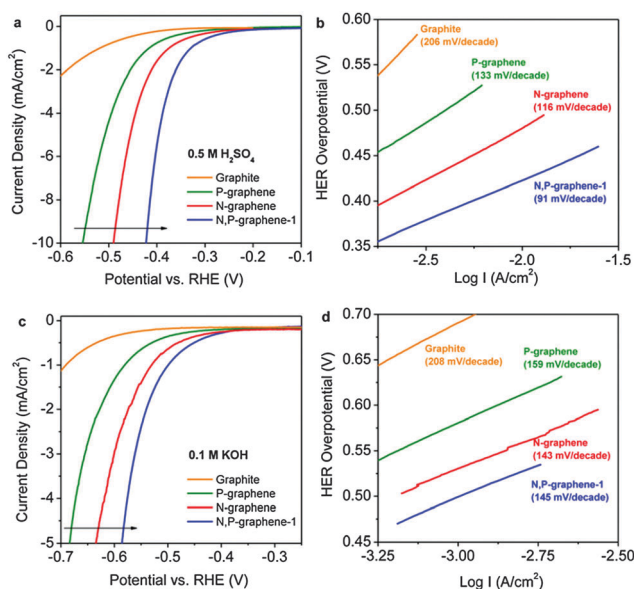

Fig. 13 (a and c) HER polarization curves and (b and d) the corresponding Tafel slopes of N,P-graphene and its single-doped counterparts under (a and b) acidic and (c and d) alkaline conditions. Adapted with permission from ref. 158. Copyright (2014) American Chemical Society.

This journal is © The Royal Society of Chemistry 2016

Chem. Soc. Rev., 2016, **45**, 2458–2493 | **2477**

outperforming the control g-C₃N₄, N-graphene and C₃N₄/NG (physically mixed) samples. The authors credited this high HER activity to a synergistic coupling effect between N-graphene and g-C₃N₄. Electrical impedance spectroscopy (EIS) data revealed an increased electrical conductivity through the coupling effect, which could possibly have resulted in the improved HER performances observed. DFT calculations further supported the experimental results with C₃N₄@NG showing a favourable ΔG_{H^*} value close to zero (0.19 eV) as compared to g-C₃N₄ (ΔG_{H^*} = −0.54 eV) and N-graphene (ΔG_{H^*} = 0.57 eV).

In an effort to improve the HER performance, the group later reported a 3D porous structure of C₃N₄ nanolayers in N-graphene films, which contained more exposed active sites. Interestingly, they found that the HER activity greatly improved after an optimized electrochemical treatment of 750 cyclic voltammetry (CV) cycles (denoted as PCN@N-graphene-750), with remarkable overpotential observed at 80 mV and a Tafel slope of 49.1 mV dec⁻¹ (Fig. 14).[171] The HER mechanism shifted from the Volmer step being the RDS prior to the CV cycles, to become the desorption controlled step after the electrochemical treatment. Besides N-doped graphene, Lee and co-workers explored the HER activity of g-C₃N₄ with P-doped graphene hybrid material.[166] They found that the P-doped graphene hybrid material performed better than the N-doped counterpart. However, one must always be cautious in evaluating the performance of the material and consider the possible effects of metallic impurities present in such systems.

5.3.2.2 Doped graphene with metal-based materials. Besides carbon-based materials, doped graphene has also been successfully coupled to metal-based materials for enhanced HER activity. These include transition metal dichalcogenides (TMDs) such as MoS₂ and WS₂ as well as metallic atoms/nanoparticles/nanoalloys. Here, doped graphene function as a support material which provides efficient electrical conductivity, high stability and

large surface area for improved catalysis.[155,172] Among various doped graphene materials, N-doped graphene is especially preferred due to its enhanced electrical conductivity, which has been proven both theoretically and experimentally.[164] When coupled with metal-based materials, which have long been identified to be HER active, these hybrids can offer dual active centres arising from the metals as well as the pyridinic-N/pyrrolic-N structures of N-doped graphene.[173] Alternatively, these metal-based materials may also act as dopants to tailor the electronic and electrochemical properties of neighbouring carbon atoms on graphene to be catalytically active sites for HER. In either case, these doped graphenes with metal-based hybrid materials have great potential to act as excellent HER electrocatalysts.

MoS₂ and WS₂ are well-studied examples of metal-based materials reported with promising HER activities.[153,174,175] They have been coupled with graphene related materials to give enhanced HER performances. Starting from hybrid materials with undoped graphene,[176,177] the trend then shifted towards coupling with N-doped graphene. Dai *et al.* demonstrated a facile synthesis of few layer MoS₂ decorated on N-doped graphene displaying improved HER performance compared to bulk MoS₂.[178] Taking a step further, Qiao's group combined this strategy with 3D structures when reporting molybdenum sulfide clusters (MoSₓ; due to the presence of HER active MoS₃ found with MoS₂) with N-doped graphene hybrid hydrogel film, and showed that the 3D hybrid performed better than its 2D counterpart.[173] Similarly, Zhang and co-workers reported MoS₂ nanoparticles supported on 3D-N-doped graphene with good HER activity.[179] Qiao's group also explored 3D WS₂ nanolayers on tri-doped graphene (P,N,O) and found that they performed better relative to the non-P-doped film, highlighting the synergistic effect between N and P co-doping.[167] Alongside MoSₓ and WS₂, SnS has also been coupled with N-doped graphene to investigate its HER performance. This hybrid (SnS–rGr) presented by Lee and co-workers clearly showed improvements in HER activity through the coupling and doping strategies, by comparison with control samples (Fig. 15).[180]

Apart from TMDs, metallic atoms, nanoparticles and nanoalloys have also been coupled with doped graphene for HER applications. Recently, Fei *et al.* reported small amounts of atomic Co dispersed on N-doped graphene with good HER catalytic activity (∼147 mV overpotential).[181] The amount of Co was optimized to be 0.57 at%, beyond which the HER
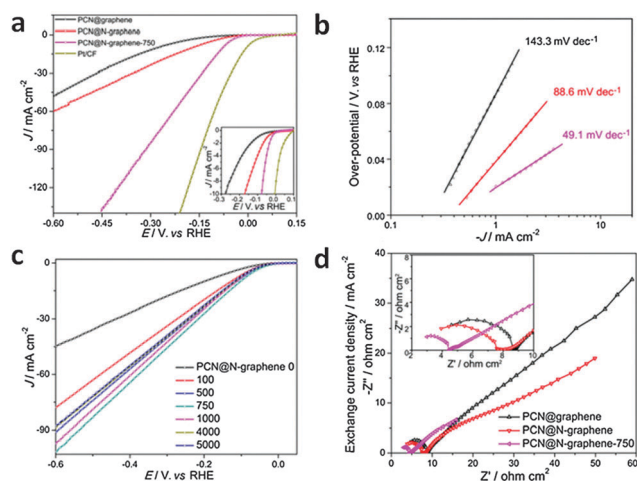

Fig. 14 (a) HER polarization curves and (b) the corresponding Tafel plots for PCN@N-graphene-750 and its control samples. (c) HER polarization curves upon various CV cycles. (d) EIS data collected at −200 mV *vs.* reversible hydrogen electrode (RHE). Adapted with permission from ref. 171. Copyright (2015) American Chemical Society.
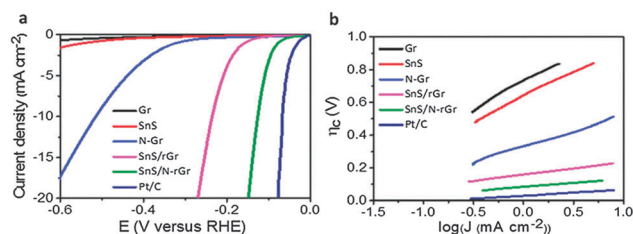

Fig. 15 (a) HER polarization curves and (b) the corresponding Tafel plots for SnS–rGr and its control samples. Adapted with permission from ref. 180. Copyright (2015) Royal Society of Chemistry.

performance deteriorated. They found that the presence of N-dopants (8.5 at%) greatly enhanced the HER activity of the hybrid ($\sim$200 mV upshift in overpotential) compared to the control sample without N-dopants. The group also investigated the role of Co by replacing Co with Fe in the catalyst, in another study.[182] They observed poorer HER performance when Fe was used, which highlights an important synergistic effect of Co–N interactions in enhancing the HER catalysis. This synergistic effect was further supported by other studies.[183,184] Besides Co atoms, Co nanoparticles ($\sim$15 nm) wrapped by N-doped carbon on N-doped graphene nanosheets as HER electrocatalysts have been reported by Zhou et al.[184] The group later expanded this strategy to 3D porous structures with improved HER activity.[185] In addition to Co atoms and nanoparticles, a Co nanoalloy was also investigated. Bao's group reported a CoNi nanoalloy encapsulated by ultrathin graphene shells (1 to 3 layers) with good HER activity.[186] They found that thinner graphene shells and higher amounts of nitrogen dopants can significantly increase the electron density in the graphene shells to enhance HER activities. Besides cobalt, ruthenium nanoparticles have also been reported to improve the HER performance of S-doped graphene materials by Shervedani and Amini.[169]

6. Electrochemistry of graphene modified with d-block elements

Whilst there is interest in doping graphene with metals (d-block elements), one should not overlook the point that the only difference between dopants and impurities is semantic. Generally, dopants are introduced into the system on purpose, while impurities tend to be inherently present or introduced unintentionally. Graphene materials are known to host a wide range of impurities, which can either be inherent in the graphitic precursors used to synthesize graphene materials, or the result of unintentional contamination of the material at various stages of the synthesis process.[136] Metallic impurities thus introduced are often electrochemically active, and have been shown to be responsible for the apparent electrocatalytic behavior of graphene materials towards an array of analytes (e.g. hydrazine, peroxides, sulfides) as well as the oxygen reduction reaction.[187–192] For top-down approaches to the synthesis of graphene materials, graphite or carbon nanotube (CNT) precursors contain metallic impurities that are extremely challenging to remove, even after exposure to strong oxidative or reductive conditions, ultrasonication, and Cl_2 at 1000 °C.[135,193] Synthetic procedures and CVD graphene transfer methods involving metal-based reagents (e.g. $KMnO_4$, $FeCl_3$) often contaminate the end materials with significant amounts of metallic impurities, despite many washing steps taken to maximize the removal of excess reagents.[8,194] Extended exposure of CVD graphene to ammonium persulfate (APS) as the chemical etchant was able to significantly decrease (but not eliminate) the amount of residual metallic impurities (Fig. 16A).[195] Unfortunately, Raman mapping (Fig. 16B) as well as optical microscopy (Fig. 16C and D) of the graphene sheets showed that this reduction of impurities came at the expense of graphene
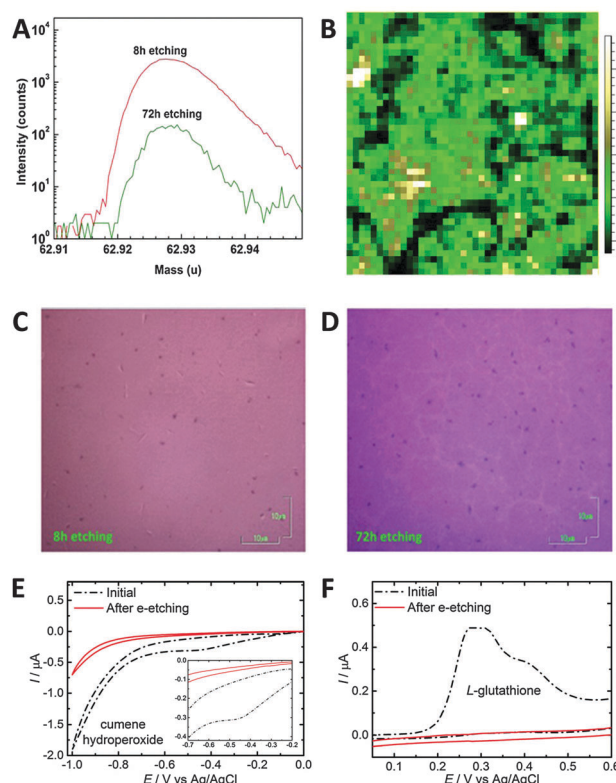

Fig. 16 Removal of metallic impurities from CVD graphene materials. (A) ToF-SIMS mass spectra in the ^{63}Cu region for CVD graphene samples etched for 8 h and 72 h in APS. (B) Mapping of Raman 2D peak intensity on CVD graphene etched for 72 h, mapped area shown is 20 × 20 μm^2. (C) Optical microscopy images of CVD graphene on SiO_2 substrates after 8 h and (D) 72 h etching. Reproduced with permission from ref. 195. Copyright (2015) American Chemical Society. (E) CVs of CVD graphene before and after electrochemical etching in the presence of 5 mmol L^{-1} CHP (inset shows a zoomed-in region) as well as (F) 5 mmol L^{-1} L-glutathione. Reproduced with permission from ref. 198. Copyright (2014) John Wiley and Sons.

layer integrity. To complicate matter further, inadvertent contamination can occur due to metallic impurities within the synthetic reagents themselves, making it difficult to anticipate the type and amount of contamination.[196] This issue was exemplified in the fabrication of graphene screen-printed electrodes using commercially available graphene inks, where the resulting devices exhibited electrocatalytic responses for the oxidation of hydrazine that was dominated by the presence of metallic impurities.[197] As the compositions and production methods of such inks are proprietary information of the manufacturer, the exact stage at which metallic impurities were introduced into the graphene could not be ascertained. Since these metallic impurities exert a dramatic influence on the electrochemical properties of graphene materials, recent research efforts have attempted to tackle this issue via purification methods. It was shown that redox-accessible metallic impurities such as Fe could be partially removed from chemically reduced graphene oxide via an electrochemical purification process by cycling the electrode in nitric acid. Successive repetitions of the purification step led to an increasing suppression of the electrocatalytic activity of the material towards the reduction of cumene hydroperoxide

(CHP), paving the way for the extension of this method to other types of graphene materials. A similar electrochemical etching method was also demonstrated to remove residual metallic impurities on CVD graphene using a solution of HCl/H_2O_2; 20 cycles of this electrochemical etching was sufficient to completely remove any parasitic electrochemical signals arising from Cu and its oxides, as well as the disappearance of cathodic and anodic peaks corresponding to the electrocatalytic reduction and oxidation of CHP and L-glutathione, respectively (Fig. 16E and F).[198] Another strategy to exclude the influence of electrochemically active metallic impurities in graphene is to pursue alternative fabrication procedures that explicitly do not involve the use of such metals, thus minimizing the possibility of such contamination. Using this line of reasoning, pure elemental lithium was combusted in carbon dioxide (in the form of dry ice), yielding graphene powder and lithium oxide.[199] Conceptually, the use of high purity starting materials (Li and CO_2) should have led to impurity-free graphene; however, ultralow traces of transition metals were still detected in the graphene sample. These levels of metallic impurities were found to be electrochemically benign toward the oxidation of NaHS, presumably because they were present at levels many factors less than conventional chemically reduced graphene.

While the profound effect of metallic impurities on the electrochemical properties of graphene materials has been reasonably studied, another major impurity that cannot be overlooked is amorphous carbon. These carbonaceous impurities, which are common in CNT samples, are known to be highly active in the electrocatalytic responses of CNTs towards many compounds.[200] The possibility of amorphous carbon impurities making their way into graphene materials should be immediately obvious if they are derived from the unzipping of CNTs, but can also occur as a side-product when graphitic materials are exposed to strong oxidative conditions.[201] It was also recently shown that even under well-controlled CVD graphene growth on Pt, amorphous carbon impurity islands can form in between the catalyst surface and monolayer graphene, and is often misidentified as areas of few-layer graphene.[202] Unsurprisingly, amorphous carbon impurities were found to be responsible for the supposed electrocatalytic responses of graphene materials toward NADH, acetaminophen, as well as hydroquinone.[201]

7. Recent electrochemical applications of graphene and its derivatives: towards the fabrication of sensors and biosensors

Owing to the extraordinary characteristics of graphene and its analogues, these materials have been widely employed to fabricate electrochemical sensors and biosensors. Here we wish to focus our attention only on the past year 2014–2015, reviewing studies on the detection of selected examples of small molecules followed by the description of studies on the detection of biomolecules.

7.1 Electrochemical sensing: direct detection of target molecules

The electrochemical sensing approach is exemplified by a direct electron transfer between the sensing platform (graphene and its derivatives) and an electroactive species, which can either be the target molecule itself or a molecule in which its produced electrochemical signal can be correlated to the target molecule. For such an approach, graphene and its derivatives are mainly utilized due to their high surface area and electron conductivity, leading to enhanced heterogeneous electron transfer and thus greater output signal intensity. In some cases, detection of target molecules can be achieved at a lower applied potential. In addition, functionalities on the surface of graphene and its derivatives can also be exploited to confer a greater affinity for the target molecules, thereby reducing the effects from interferences. Hence, with the utilization of graphene and its derivatives, greater sensitivity of the electrochemical sensor and its applicability for real sample matrices can be achieved.

Chemically modified graphene (CMG) materials[203] have been successfully used as transducers for the analysis of electroactive probes in food samples. Given the multitude of CMGs prepared by following various protocols and possessing different structural features such as the amount of disorders and oxygen functionalities, comparisons have been performed in order to identify the material that could be better suited to detect a specific analyte. Detection of nitrite, which is commonly used as a food additive but can be hazardous to humans, has been performed on both chemically reduced graphene oxide (CRGO) and electrochemically reduced graphene oxide (ERGO).[204] The former showed higher sensitivity, lower potential for nitrite oxidation and a better selectivity in the presence of interferences. The authors attribute this behavior to the presence of unreduced oxygen moieties on ERGO, which were absent on the CRGO surface, as shown also by the FTIR study. The transducer based on CRGO was finally employed for the selective detection of nitrite in water samples.

Several CMG platforms namely graphite oxide (GPO), graphene oxide (GO) and ERGO were used for a comparative study on the detection of caffeine in coffee, tea and energetic drink samples.[205] It was found that ERGO, due to the lower amount of oxygen functionalities, provided the best analytical performance for the detection of caffeine based on sensitivity, linearity and reproducibility of response. The same authors also demonstrated that depending on the graphite oxide preparation protocol, different intrinsic electrochemistry can be shown by the electrochemically reduced graphene materials.[206] The authors used electrochemically reduced graphene nanoribbons in which the corresponding graphite oxide was obtained by using permanganate oxidants. They observed that the oxidation peak of caffeine on such a platform was strongly influenced by the inherent background signal of the reduced graphene nanoribbons. This showed that the potential window of these materials should be carefully taken into account when detecting analytes which are electroactive at positive potentials, such as most of the biological and clinical probes. A comparative study on how the structural properties of

2480 | Chem. Soc. Rev., 2016, 45, 2458–2493

This journal is © The Royal Society of Chemistry 2016

the graphene material could influence the assessment of anti-oxidant capacity in wine samples was also performed.[207] The authors employed three CMG platforms namely GO, CRGO and ERGO, possessing different amounts of oxygen-containing groups. They demonstrated that the latter could favour the interaction between the graphene surface and the analyte of interest, and at the same time be detrimental to the heterogeneous charge transfer. The best electrochemical performance in terms of calibration sensitivity, selectivity, and linearity of response was shown by ERGO, due to the presence of non-electrochemically reducible oxygen functionalities which played a major role in promoting the interactions between the graphene surface and the analyte. Therefore, the same group was able to tune the analytical performance of the graphene oxide platform by carrying out the electrochemical reduction of the starting material at increasing negative potentials from -0.25 V to -1.50 V.[208] The eight ERGO platforms, carrying a decreasing amount of oxygen-containing groups, were used for the detection of standard gallic acid, a standard polyphenol which is commonly used as an index of the anti-oxidant capacity of food and beverages. ERGO obtained after reduction at -0.90 V, which provided the best electroanalytical performance, was then employed for the assessment of the antioxidant capacity of fruit juice samples. Lately, several nanomaterials have been used to fabricate functional graphene nanocomposites which show improved performances when used as sensing and biosensing platforms. This behavior has been attributed to various reasons, including the increased surface area and the synergistic effect derived from the combination of the materials. Long et al.[209] developed a novel imprinted electrochemical sensor based on a composite including graphene nanosheets and cobalt–nickel bimetallic nanoparticles for the detection of octylphenol, a compound known to be involved in the disruption of the mammalian endocrine system. The electrochemical detection of the analyte in plastic bottles, metal bottles and food packaging bags was performed and the achieved detection limit was in the pM range. An electrodeposited bi-enzymatic biosensor based on graphene and gold nanoparticles was employed for the detection of carbamates, a major class of pesticides with very severe adverse effects on both humans and animals.[210] The proposed biosensor exhibited an improved Michaelis–Menten kinetic constant and a low detection limit for the detection of several carbamates in citrus fruit samples, without significant interferences from ascorbic and citric acid and glucose.

Electrochemical detection of nitrite was carried out on reduced graphene oxide and dendritic copper nanoclusters electrodeposited on a glassy carbon electrode.[211] The developed sensor showed improved electrocatalytic activity for nitrite detection as well as a low detection limit of 0.4 μM, due to the enlarged surface-to-volume ratio including more electroactive sites for the reduction of nitrite. The same analyte was detected on a biosensor based bifunctionalized graphene–gold nanoparticle hybrid, obtained by the in situ growth of gold nanoparticles. Haemoglobin was then employed as a bio-recognition element and the developed biosensor allowed the

detection of nitrite in pickled radish by achieving a detection limit of 0.01 μM.

A novel electrochemical sensor for the detection of fructose was developed by immobilizing a highly dispersed CuO–Cu nanocomposite on graphene, which was previously non-covalently functionalized with sodium dodecyl benzene sulfonate (SDBS).[212] The improved electrochemical performance of the composite material for fructose detection was mainly due to the exceptional cation anchoring ability of SDBS, which prevented the aggregation among Cu-based nanoparticles during the nanocomposite synthesis.

The detection of colorants in food has also been successfully performed on graphene-composite materials. For safety issues, either the amount of dyes used in the food industry as colouring agents or the trace colorants present as food contaminants have to be strictly controlled, those compounds being harmful for humans at high doses. Gan et al. used graphene sheets decorated with highly-ordered mesoporous TiO$_2$ nanoparticles to detect Sudan I, one of the most used azo-dyes in petroleum and textile industries which can be found as trace in animal tissues.[213] The low detection limit achieved with the composite material was due to its high specific area, strong adsorptive capacity and excellent electrocatalytic properties. The same authors used the same transducer to analyse chilli products and ketchup samples for the presence of Orange II, an azo-colorant which is not permitted in food preparation due to its high toxicity.[214] In addition, the graphene–TiO$_2$ composite was also used by the same group for the simultaneous detection of sunset yellow and tartrazine,[215] two very common colorants used as food additives. Well separated voltammetric peaks were obtained by using the composite materials, thus allowing the determination of both compounds in several food sample extracts. The simultaneous detection of the same colorants in commercial soft drinks was also performed by Ye et al.[216] on a beta-cyclodextrin-coated poly(diallyldimethylammonium chloride)-functionalized graphene composite film, obtained by using L-ascorbic acid as the reducing agent. Finally, a graphene quantum dot-gold nanoparticle multi-layered material was employed by Hou et al. for the determination of malachite green, a dye generally used in materials such as silk, leather and paper.[217] The developed transducer presented good recoveries and a detection limit of 1×10^{-7} M for the detection of malachite green in fish samples.

Doped graphene platforms have also been recently used for the assessment of food quality and safety. Recent reports have shown that p- and n-type doped graphene materials obtained by performing doping with either electron donating or electron withdrawing species yield graphene materials possessing different electronic properties.[218] Bonanni and coworkers compared boron-doped graphene and nitrogen-doped graphene platforms containing different amounts of heteroatoms for the antioxidant activity quantification of tea samples.[219] They demonstrated that for this purpose, the type and amount of dopant have a significant influence on the electrochemical detection of gallic acid rather than the structural properties of the materials. In a different study performed by the same

This journal is © The Royal Society of Chemistry 2016

Chem. Soc. Rev., 2016, 45, 2458–2493 | 2481

group, the electrochemical detection of catechin was carried out on boron-doped graphene, nitrogen-doped graphene and undoped graphene platforms.[220] The authors found out that the undoped graphene, possessing a lower amount of oxygen functionalities, a higher density of defects and a larger electroactive surface area provided the best electroanalytical performance for the determination of catechin in commercial beer samples.

7.2 Electrochemical biosensing: detection of target molecules *via* the bio-recognition process

The electrochemical biosensing approach shows that detection of the target molecules is achieved through a specific bio-recognition process between the target molecules and their respective bio-recognition elements. The main aspect of this approach lies in the employment of a bio-recognition layer and this layer is responsible for conferring selectivity and specificity to the respective biosensors. The bio-recognition layer is fabricated on the sensing platform with biological recognition structures such as nucleic acids, antibodies and enzymes, as depicted in Fig. 17. Similarly, for the electrochemical biosensing approach, graphene and its derivatives are generally adopted because of their large surface area and excellent electron conductivity. The large surface area displayed by these materials is beneficial for enhancing the amount of bio-recognition elements that can be immobilized during the fabrication of a bio-recognition layer. In addition, they can also provide a greater available surface area for heterogeneous electron transfer. For achieving excellent electron conductivity, they aid in faster heterogeneous electron transfer. The properties of both graphene and its derivatives can contribute greatly to the enhancement of the analytical signal intensity, therefore improving the sensitivity of the electrochemical biosensor.

7.2.1 Nucleic acids as bio-recognition elements (genosensing). With nucleic acid adopted as the bio-recognition element, different immobilization techniques have been employed to construct a bio-recognition layer on the surface of graphene and its analogues. It is imperative to choose the most appropriate immobilization technique in order to ensure the stability and the desired orientation of the immobilized nucleic acid bio-recognition element as graphene and its analogue materials have different

Fig. 17 The different classes of bio-recognition elements utilized in the fabrication of electrochemical biosensors.

properties and functional moieties present on their surfaces. Immobilization techniques that are widely adopted are:

● Physical adsorption – in physical adsorption, the immobilization of nucleic acid probes onto graphene materials exploits the hydrophobic and π–π interactions between the aromatic rings of nucleobases in nucleic acids and the hexagonal cells of graphene materials. The resulting orientation of the immobilized nucleic acid probes is random.

● Covalent attachment – in covalent attachment, the immobilization process involves the formation of a covalent bond, usually an amide bond, between the graphene materials and the nucleic acid probes. To achieve an amide bond, the inherent carboxylic functional groups on the surface of the materials are often exploited. Upon activation by carbodiimide/ N-hydroxysuccinimide (EDC/NHS) chemistry, nucleic acid with a NH_2 terminal can subsequently be covalently attached to the surface of graphene materials.

● Cross-linking –the cross-linking method often involves an organic linker molecule which facilitates the covalent immobilization of nucleic acid probes onto the surface of graphene materials. A linker molecule is usually employed when the graphene materials do not have sufficient inherent carboxylic functional groups on the surface for direct covalent attachment with the nucleic acid probes. Hence, linker molecules generally have dual properties; containing hydrophobic regions for conjugation to the basal plane of graphene materials by hydrophobic and π–π interactions, and containing carboxylic functional groups for formation of amide linkages with nucleic acid probes with NH_2 terminal.

● Biotin–avidin interaction – the biotin–avidin immobilization technique is a form of bio-recognition process on its own. Avidin is a protein which has the ability to bind up to four biotin molecules. Interesting to note, the biotin–avidin complex is the strongest known non-covalent interaction between a protein and a ligand. For this technique, prior modification of the surface of graphene materials with a layer of avidin molecules is required before the introduction of biotinylated nucleic acid probes. Upon introduction, biotinylated nucleic acid probes will bind to the avidin molecules by affinity, resulting in the immobilization of nucleic acid probes on graphene materials.

● Electrostatic attraction – in electrostatic attraction, immobilization of nucleic acid probes is achieved through the negatively charged phosphate backbone of nucleic acids, thereby exposing the nucleobases for efficient hybridization. Hence, this suggests that the surface of graphene materials has to be modified in order to confer a certain degree of positive charge to it. Similar to the cross-linking method, an organic molecule with dual properties may be exploited.

With nucleic acids functioning as the bio-recognition elements, electrochemical biosensors for the detection of various target molecules have been developed, with their concepts elaborated in the subsequent subsections, according to the class of target molecules.

7.2.1.1 Nucleic acid analysis. For the purpose of detecting nucleic acids with nucleic acids also serving as the recognition
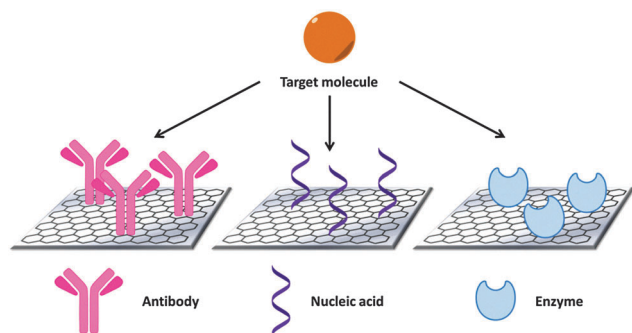
2482 | *Chem. Soc. Rev.,* 2016, **45**, 2458–2493

This journal is © The Royal Society of Chemistry 2016

elements, various forms of graphene materials have been employed in recent years, with the most common being chemically reduced graphene oxide (CRGO). Mukherjee et al.[221] designed a biosensor for the detection of *Mycobacterium tuberculosis* gene, with CRGO functioning as the sensing platform. A single-stranded nucleic acid probe was first covalently immobilized onto the CRGO surface, with methylene blue (MB) serving as an electroactive hybridization indicator. Due to the greater affinity which MB has for single-stranded nucleic acid as compared to double-stranded nucleic acid, a smaller differential pulse voltammetry (DPV) peak current was derived after hybridization with the target nucleic acid. A detection range of 2.872×10^{-3}–2.872×10^{5} ng μL^{-1} was obtained for the fabricated biosensor, with good selectivity against single-base mismatched and non-complementary nucleic acids. In another report, Benvidi et al.[222] demonstrated an impedimetric biosensor for the sensing of amelogenin gene, also using CRGO as the transducing platform, and covalent nucleic acid probe immobilization (Fig. 18A). The proposed biosensor presented a wide detection range of

1×10^{-20}–1×10^{-14} M, with a limit of detection (LOD) of 3.2×10^{-21} M. In addition, the biosensor also displayed good specificity against non-complementary nucleic acid. Subsequently, the same group attempted to improve the analytical performance of their biosensor in another study.[223] Employing CRGO as the sensing interface, Zhang et al.[224] reported on an impedimetric biosensor for the detection of hepatitis B virus. In this study, the nucleic acid probe was covalently immobilized onto CRGO by the cross-linking technique. In order to facilitate the cross-linking process, CRGO was first functionalized with tryptamine and then glutaraldehyde. The sensing platform exhibited a detection range of 1×10^{-12}–1×10^{-7} M, with a LOD of 5.2×10^{-13} M. Furthermore, the biosensor also showed high selectivity against single-base mismatched and non-complementary nucleic acids.

Apart from chemical reduction, graphene oxide (GO) can be reduced by thermal methods as well. In 2014, Rasheed and Sandhyarani[225] published a work on employing thermally reduced graphene oxide (TRGO) as the sensing platform for the detection of breast cancer 1 (BRCA1) gene. The proposed sensor used a sandwich detection strategy, as illustrated in Fig. 18B. The capture probe (DNA-c) underwent physical adsorption onto TRGO while gold nanoparticle (AuNP) were covalently conjugated to the reporter probe (DNA-r) to form DNA-r.AuNP. Upon hybridization with the BRCA1 gene, a sandwich complex was formed and the oxidation signal of AuNPs was utilized for BRCA1 gene detection by chronoamperometry. A detection range of 1 fM–1 nM was attained and selectivity was achieved with three-base mismatched and non-complementary nucleic acids.

Following CRGO and TRGO, electrochemically reduced graphene oxide (ERGO) was employed for the purpose of nucleic acid detection. Li et al.[226] presented a human immunodeficiency virus 1 (HIV1) gene biosensor based on an ERGO modified graphene surface. The nucleic acid probe was physically immobilized onto the sensing platform, before undergoing hybridization with HIV1 gene. Herein, the analytical signal was derived from the DPV peak current of ferricyanide. The sensing interface achieved a detection range of 10^{-12}–10^{-7} M, with a LOD of 1.58×10^{-13} M and selectivity against non-complementary nucleic acid.

Moving on, in addition to reduced analogues of GO, other types of graphene materials have also been applied to nucleic acid sensing. These materials include thiofluorographene,[227] GO[228] and GO/graphite hybrid.[229,230] Urbanova et al.[227] demonstrated the proof-of-concept of using thiofluorographene as a platform for impedimetric nucleic acid sensing. Thiofluorographene was obtained by substituting fluorine atoms in fluorographene with nucleophilic sulfhydryl groups. Physical adsorption was adopted to immobilize the nucleic acid probe before hybridization reaction. It was shown that thiofluorographene could distinguish between complementary, single-base mismatched and non-complementary nucleic acids, while fluorographene did not have such capability. On another note, Sun et al.[228] fabricated a biosensor for the sensing of miRNA-21, a diagnostic tool for lung cancer. In this report, GO was utilized as the transducing platform with a silver nanoparticle (AgNP)-labelled
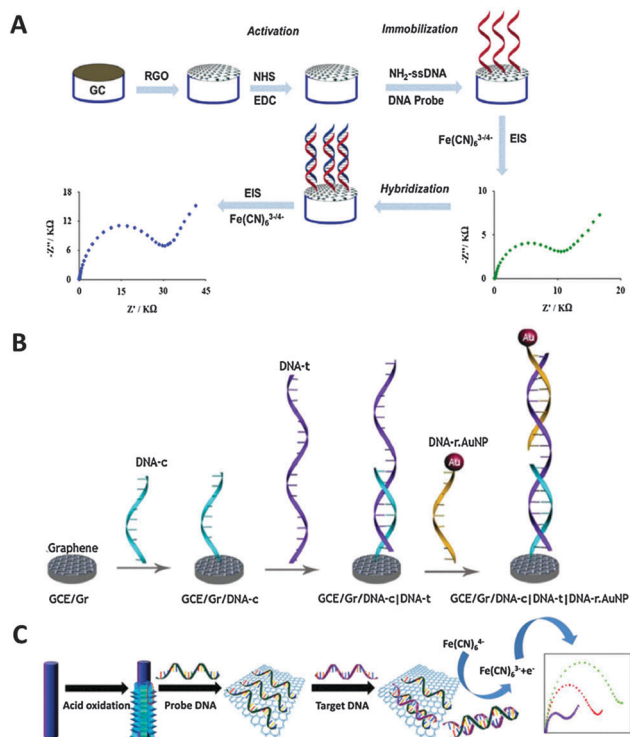

Fig. 18 (A) Illustration of impedimetric biosensor for the sensing of amelogenin gene, based on CRGO as the transducing platform and covalent immobilization of a single-stranded nucleic acid probe. Upon hybridization with the amelogenin gene, charge transfer resistance (R_{ct}) between $[Fe(CN)_6]^{3-/4-}$ and the electrode surface increased. Reproduced with permission from ref. 222. Copyright (2014) Elsevier. (B) Schematic representation of the various fabrication stages of the biosensor designed for BRCA1 gene detection. Reproduced with permission from ref. 225. Copyright (2014) Elsevier. (C) Illustration of a scaly GO/graphite fiber hybrid electrode employed for impedimetric DNA sensing. Upon hybridization with a complementary DNA target, the partial release of the double-stranded DNA resulted in a lower R_{ct}. Reproduced with permission from ref. 230. Copyright (2015) John Wiley and Sons.

This journal is © The Royal Society of Chemistry 2016

Chem. Soc. Rev., 2016, **45**, 2458–2493 | **2483**

nucleic acid probe physically adsorbed on the surface. In the presence of miRNA-21, hybridization occurred, forming a duplex structure which was then released from GO. Hence, the stripping current of AgNPs can be exploited as the analytical signal and a detection range of 100 fM–1 nM was acquired, with a LOD of 60 fM. Selectivity of the biosensor was also displayed against up to three mismatched sites. For the application of the GO/graphite hybrid, two separate studies have been published. Firstly, Congur et al.[229] presented an impedimetric biosensor for detecting miRNA-34a, which is related to Alzheimer's disease and cancers. In this work, a pencil graphite electrode modified with GO was adopted as the sensing surface. Interesting to note, their sensing approach was to hybridize the nucleic acid probes with the miRNA-34a targets before exposing the sensing surface to the formed duplex. Due to the NH_2 terminal of the nucleic acid probe, the duplex underwent covalent bonding with the GO/graphite surface. The fabricated sensor achieved a detection range of 0–10 μg mL^{-1}, with a LOD of 1.9 μg mL^{-1} and selectivity against other miRNAs. In the second study conducted by Zhang et al.,[230] a scaly GO/graphite fiber hybrid electrodes were utilized as the sensing platform for impedimetric detection of nucleic acid (Fig. 18C). GO sheets were synthesized in situ at the surface of graphite fibers by acid oxidation to yield scaly GO/graphite fiber hybrid electrodes. The partially peeled GO sheets provided numerous binding sites for nucleic acid probe immobilization and thus enhanced electron transfer. Herein, the nucleic acid probe underwent physical adsorption on a GO/graphite hybrid prior to hybridizing with its complementary nucleic acid target. Due to the lower affinity towards double-stranded nucleic acid as compared to single-stranded nucleic acid, detection of the nucleic acid target was achieved. The range of detection was determined to be 0.01–1 nM, with a LOD of 5.6 pM and selectivity demonstrated against single-base mismatched and non-complementary nucleic acids.

7.2.1.2 Biomolecule analysis.
In addition to the detection of nucleic acids, sensing of smaller biological molecules is also achievable with nucleic acids functioning as the recognition elements. Wu et al.[231] reported an aptasensor for the detection of adenosine triphosphate (ATP) using the ATP aptamer as the recognition element (Fig. 19). Aptamers are synthetic single-stranded nucleic acids which are in vitro selected through the systematic evolution of ligands by exponential enrichment (SELEX) process to bind to specific target biomolecules. They exhibit several advantages, including high specificity, simple structure, easy synthesis and long-term stability. Herein, CRGO was utilized as a label and its electrocatalytic property towards ascorbic acid (AA) oxidation, derived from its defective sites, was exploited. For the fabrication of the aptasensor, the ATP aptamer with a SH terminal was first covalently linked to the gold electrode. In the absence of ATP, CRGO can bind to the ATP aptamer through π–π stacking interactions, leading to a greater DPV oxidation current and a lower oxidation potential of AA. On the other hand, in the presence of ATP, the immobilized aptamer formed a complex with ATP and CRGO was released from the biosensing interface, resulting in a sharp
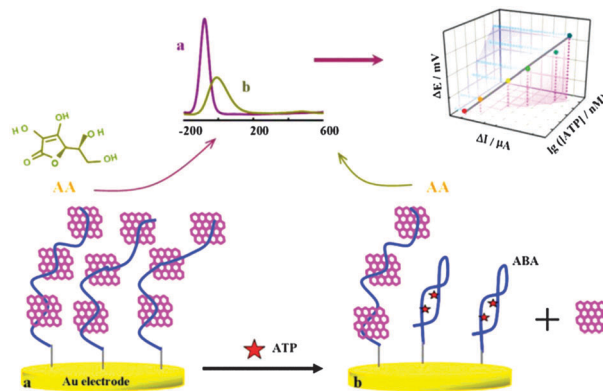

Fig. 19 Schematic representation of an electrochemical aptasensor for ATP. Reproduced with permission from ref. 231. Copyright (2015) Elsevier.

decrease in oxidation current and an increase in the oxidation potential of AA. The changes in the oxidation current and the oxidation potential of AA were both employed as the analytical signals for the detection of ATP. With oxidation current as the analytical signal, a low LOD of 11.7 pM and a wide detection range of 0.05 nM–1.0 μM were attained. Whereas, when using oxidation potential as the analytical signal, a LOD of 25.0 pM with a detection range of 0.05–10.0 nM was acquired. In addition, the aptasensor also displayed excellent selectivity for ATP over the other analogues.

7.2.1.3 Heavy metal analysis.
Nucleic acids playing the role of a recognition element can contribute to the monitoring of environmental safety by detecting for pollution by heavy metals. Zhang et al.[232] demonstrated a biosensor for mercury (Hg^{2+}) detection based on thymine–mercury–thymine ($T–Hg^{2+}–T$) interactions and CRGO as the transducing platform. As shown in Fig. 20A, a single-stranded, ferrocene-tagged T-rich nucleic acid probe was first physically adsorbed onto the surface of CRGO, with the redox peaks of ferrocene utilized as the analytical signal with DPV. In the presence of Hg^{2+}, the ferrocene-labelled T-rich probe could hybridize with another single-stranded nucleic acid, forming a double-stranded nucleic acid complex through Hg^{2+}-mediated coordination of $T–Hg^{2+}–T$ base pairs. Owing to the weaker affinity between CRGO and a double-stranded nucleic acid complex, ferrocene drew away from the surface of CRGO and the resulting redox peaks were substantially diminished. The proposed biosensor displayed a LOD of 5 pM, with a detection range of 25 pM–10 μM. Furthermore, high selectivity of the biosensor was also reported.

In another study, Tang et al.[233] also reported a biosensor for Hg^{2+} sensing, exploiting $T–Hg^{2+}–T$ interactions and ERGO as the sensing platform. As seen in Fig. 20B, a single-stranded nucleic acid was first covalently immobilized onto the sensing platform by cross-linking. Upon exposure to Hg^{2+}, stable duplex complexes were formed through strong $T–Hg^{2+}–T$ bonding with two immobilized nucleic acid strands in close proximity. The captured Hg^{2+} subsequently catalyzed the formation of AuNPs. Since the extent of AuNPs formation was proportional to the concentration of Hg^{2+}, Hg^{2+} concentration was directly quantified
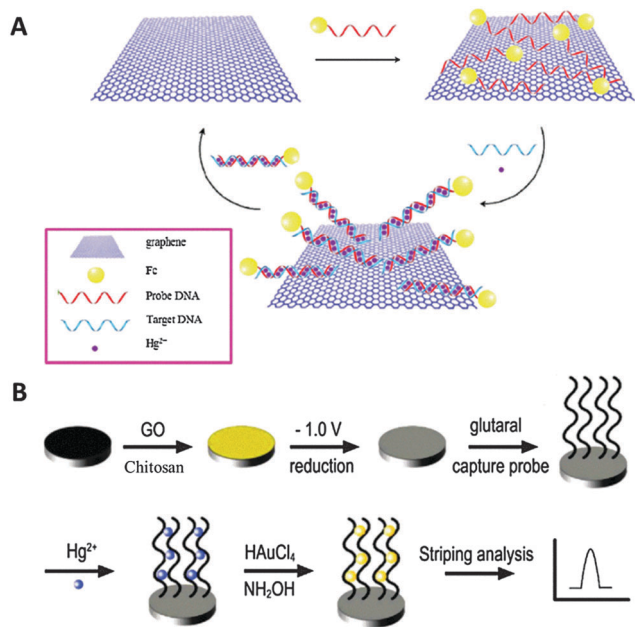
Fig. 20 (A) Schematic illustration of an electrochemical Hg^{2+} biosensor based on T−Hg^{2+}−T interactions and CRGO as the transducing platform. Reproduced with permission from ref. 232. Copyright (2015) Elsevier. (B) Representation of an electrochemical biosensor for Hg^{2+} based on the catalytic formation of AuNPs. Reproduced with permission from ref. 233. Copyright (2014) Elsevier.

by stripping voltammetry of the formed AuNPs. The proposed biosensor demonstrated a range of detection of 0.5–120 nM, with a LOD of 0.06 nM. Similar to the previous work, excellent selectivity against other metal ions was also obtained.

7.2.2 Antibodies as bio-recognition elements (immuno-sensing). For the construction of bio-recognition layers with antibodies, additional considerations have to be exercised as antibodies are a class of proteins. As compared to nucleic acids, proteins are generally much more sensitive to their physiological environments and can be easily denatured or degraded by physical and chemical effects. Furthermore, it is crucial to maintain the inherent conformation of an antibody during the immobilization process and ensure its correct orientation. The common immobilization strategies are:

• Physical adsorption – in physical adsorption, antibodies are conjugated onto the surface of graphene materials through mainly hydrophobic interactions. Physical adsorption is the simplest and most straightforward immobilization method as compared to the other strategies. However, such a method results in the random orientation of the immobilized antibodies.

• Covalent attachment – based on the covalent attachment technique, antibodies are linked to the surface of graphene materials through the formation of covalent bonds, usually an amide bond. To form an amide bond, antibodies with a NH$_2$ terminal and inherent carboxylic functional groups on the surface of graphene materials are often exploited. Upon activation by EDC/NHS chemistry, amide linkages are generated and antibodies are covalently attached to the surface of graphene materials. Apart from amide bonds, other types of covalent

bonds are also plausible, depending on the type of functional groups available on the antibodies and graphene materials. As compared to physical adsorption, covalent attachment allows control over the orientation of the immobilized antibodies.

• Cross-linking – the cross-linking immobilization approach makes use of linker molecules to facilitate the covalent attachment of antibodies to the surface of graphene materials. This approach is generally employed in cases where there are no or insufficient quantity of the desired functional groups present on the surface of graphene materials. In addition, cross-linking can also be employed to create spacing, thereby enhancing the accessibility of the antibodies to the target molecules.

• Biotin–avidin interaction – the principle behind this immobilization technique lies in the exceptional affinity between biotin and avidin molecules. Each avidin molecule is capable of binding to four molecules of biotin. To adopt this immobilization strategy, pre-modification of graphene materials and antibodies is crucial. Graphene materials have to be modified with avidin molecules while antibodies have to be functionalized with a biotin moiety each. Upon exposure, the biotinylated antibodies will bind to the avidin molecules by affinity, thereby immobilizing the antibodies onto graphene materials.

The following subsections will demonstrate how electrochemical biosensors exploiting antibodies as the bio-recognition elements can be used for the detection of various target molecules.

7.2.2.1 Disease biomarker analysis. The detection of disease biomarkers using antibodies as the recognition elements represents a popular and effective clinical diagnostic tool. Among the various measurement techniques, electrochemical immunoassays are the most ideal owing to their advantages of affordability, rapid analysis, sensitivity and portability. To date, graphene materials have been extensively involved in the development of electrochemical immunosensors for the detection of biomarkers and other target molecules.

Chemical vapor deposition grown graphene represents an example of graphene materials, which has been gaining research attention in recent years due to the demand for high quality graphene materials. Eissa *et al.*[234] reported on the utilization of CVD graphene for the development of an impedimetric immunosensor for ovalbumin. The ovalbumin antibody was covalently immobilized on CVD graphene using the cross-linking approach, where CVD graphene underwent prior functionalization with carboxylic groups. The reported immunosensor displayed a detection range of 1 pg mL^{-1}–100 ng mL^{-1}, with a LOD of 0.9 pg mL^{-1} and selectivity against non-specific proteins. In another study adopting CVD graphene as the transducing platform, Jin *et al.*[235] designed a voltammetric immunosensor for carcinoembryonic antigen (CEA). Interesting to note, the capture antibodies were first covalently immobilized onto magnetic beads before getting attached onto a CVD graphene platform by an external magnetic field. A sandwich strategy was also employed, using AuNPs conjugated with detection antibodies and horseradish peroxidase (HRP) enzymes. The sensing approach is presented in Fig. 21A and the HRP/H$_2$O$_2$ catalytic system

This journal is © The Royal Society of Chemistry 2016

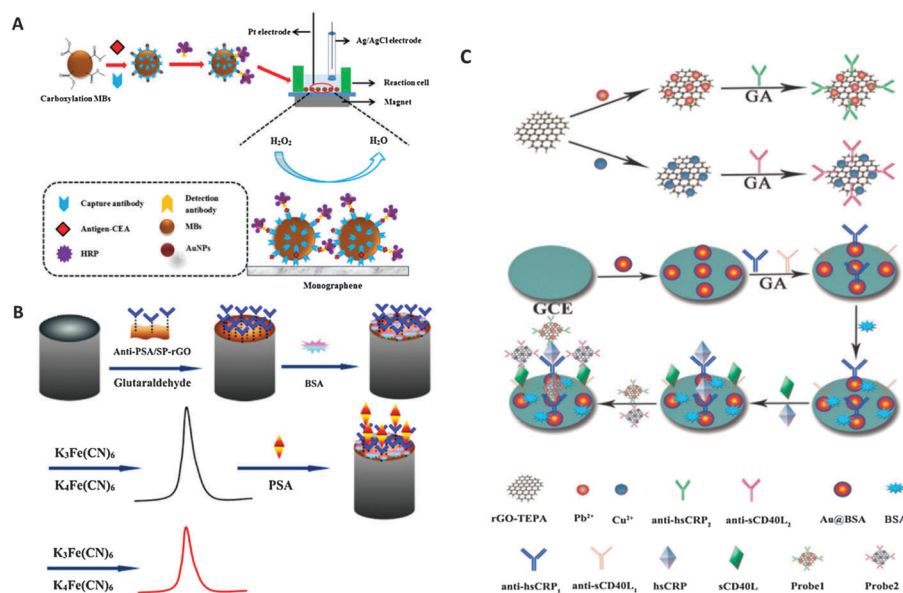*Chem. Soc. Rev.,* 2016, **45**, 2458–2493 | 2485

Fig. 21 (A) Preparation of a magnetic field-controlled voltammetric CEA immunosensor with CVD graphene functioning as the sensing platform. Reproduced with permission from ref. 235. Copyright (2014) Elsevier. (B) Schematic representation of the fabrication process and electrochemical response of the PSA immunosensor. Reproduced with permission from ref. 237. Copyright (2015) Springer. (C) Preparation of CRGO conjugated with respective metal ions and antibodies to function as labels for simultaneous detection of CRP and CD40L. Schematic illustration of the electrochemical immunoassay employed. After CRP and CD40L had been captured by their respective antibodies on the sensing interface, CRGO hybrid labels selectively bound to CRP and CD40L, forming a sandwich complex. Reproduced with permission from ref. 238. Copyright (2015) Elsevier.

provided an analytical signal which was monitored by cyclic voltammetry. Based on the sensing approach, the detection range was concluded to be 5–60 ng mL^{-1}, with a LOD of 5 ng mL^{-1} and superior specificity. CVD grown graphene was also exploited as the transducing material for the detection of immunoglobulin G (IgG) in a report by Loo et al.[236] Loo et al. demonstrated impedimetric immunosensing of IgG, with the recognition element physically immobilized on CVD graphene. The fabricated immunosensor displayed a range of detection of 0.1–100 μg mL^{-1}, a LOD of 0.136 μg mL^{-1} and selectivity against other proteins.

Apart from CVD grown graphene, reduced analogues of GO, such as CRGO, have also been widely used for immunosensing. Wang et al.[237] fabricated an impedimetric immunosensor for the detection of prostate specific antigen (PSA). In their work, CRGO was employed as the transducing material and it was functionalized with silk peptide and glutaraldehyde to facilitate the covalent immobilization of anti-PSA via the cross-linking technique. The immunosensing approach is shown in Fig. 21B. Based on the fabricated sensor, 0.1–5.0 ng mL^{-1} and 5.0–80.0 ng mL^{-1} were determined as the detection ranges, with a LOD of 0.053 ng mL^{-1}. Finally, selectivity against other proteins was also observed. In another two studies, CRGO functionalized with tetraethylene pentamine (CRGO-TEPA) was utilized. Firstly, Yuan et al.[238] reported a voltammetric immunosensor for simultaneous detection of C-reactive protein (CRP) and CD40 ligand (CD40L) based on a sandwich assay (Fig. 21C). Herein, CRGO-TEPA was employed as a label, with metal ions conjugated to it and detection antibodies covalently immobilized on it through cross-linking with glutaraldehyde. Detection of

CRP and CD40L was achieved by detecting their respective metal ions on the CRGO-TEPA labels with DPV. With the proposed sensing interface, the detection range was assessed to be 0.05–100 ng mL^{-1}, with a LOD of 16.7 pg mL^{-1} and 13.1 pg mL^{-1} for CRP and CD40L, respectively. Furthermore, specificity was also shown by the immunosensor. In the second study, Wu et al.[239] used CRGO-TEPA as the platform to design a voltammetric immunosensor for the simultaneous detection of two cervical cancer biomarkers, CEA and squamous cell carcinoma antigen (SCCA). The respective capture antibodies were covalently immobilized on CRGO-TEPA and a sandwich assay was employed. Two different redox mediators, neutral red and thionine, were utilized as labels to produce the analytical signals which were then monitored by DPV. Based on the immunosensing approach, CEA and SCCA could be detected in the range of 0.05–20 ng mL^{-1} and 0.03–20 ng mL^{-1} accordingly. In addition, LOD of CEA and SCCA was found to be 0.013 ng mL^{-1} and 0.010 ng mL^{-1}, respectively. Acceptable selectivity parameters were also displayed by the immunosensor. As an extension of CRGO, CRGO nanoribbons have also been demonstrated by Shi et al.[240] to be an useful platform for the concurrent detection of interleukin-6 (IL-6) and matrix metallopeptidase-9 (MMP-9). In their work, IL-6 and MMP-9 capture antibodies were immobilized onto CRGO nanoribbons by physical adsorption to fabricate the sensing interface. A sandwich assay was also employed with two different metals acting as labels for detection by stripping voltammetry. The developed immunosensor exhibited a detection range of 10 fg mL^{-1}–1 μg mL^{-1} and 1 pg mL^{-1}–1 μg mL^{-1}, with a LOD of 5 fg mL^{-1} and 0.1 pg mL^{-1}, for MMP-9 and IL-6, respectively.

2486 | Chem. Soc. Rev., 2016, 45, 2458–2493

This journal is © The Royal Society of Chemistry 2016

In addition, good specificity was also displayed by the immunosensor.

Moving on from CRGO, other types of graphene materials have also been used in recent years. For example, Kailashiya et al.[241] presented a GO-based impedimetric immunosensor for platelet-derived microparticles (PMPs). In their work, the antibody for PMPs was covalently immobilized on the GO surface and the sensing platform attained a detection range of 100–7000 counts per μL with specificity. In another study, Lim et al.[242] reported on a graphene-based immunosensor for human chorionic gonadotropin (hCG), where AuNPs were utilized as labels. The capture antibody was first physically adsorbed onto graphene, before exposing to hCG and sandwiched with a detection antibody conjugated with AuNPs. DPV was subsequently employed to measure the analytical signal derived from AuNPs and the detection range was found to be 0–500 pg mL^{-1}, with a LOD of 5 pg mL^{-1}.

7.2.2.2 Nucleic acid analysis. Apart from biomarkers, the application of antibodies as recognition elements can be extended to nucleic acid analysis. Tran et al.[243] demonstrated the use of antibodies in the fabrication of a voltammetric immunosensor for the detection of miRNA-141. Herein, a CRGO and carbon nanotube composite was employed as the transducing platform and a single-stranded DNA probe was first covalently immobilized onto the surface. Upon exposure to the target miRNA, hybridization occurred and a DNA/RNA hybrid was formed. Subsequently, an antibody bound selectively to the DNA/RNA hybrid before a

secondary antibody, which was conjugated to HRP, bound to the first antibody. The HRP/H$_2$O$_2$ catalytic system oxidized hydroquinone to benzoquinone and the subsequent reduction of benzoquinone back to hydroquinone at the electrode was exploited as the analytical signal using square wave voltammetry (SWV). With this immunosensing approach, the LOD was calculated to be 30 fM, with selectivity shown against non-complementary miRNA.

7.2.2.3 Relevant biological molecule analysis. For the monitoring of food safety, Narayanan et al.[244] designed a voltammetric immunosensor for the detection of botulinum neurotoxin (BoNT). The proposed sensor utilized carboxylic groups functionalized CRGO as the sensing platform, with the BoNT antibody covalently immobilized on it. Fig. 22 briefly illustrates the immunosensing protocol, ending with the deposition of AgNPs. As such, the stripping current of AgNPs was used for the quantification of BoNT. The developed immunosensor could selectively detect BoNT in the range of 10 pg mL^{-1}–10 ng mL^{-1}, with the LOD at 5 pg mL^{-1}.

Other than food toxins, antibodies can also be applied in the sensing of important biological molecules such as cholesterol. Ali et al.[245] demonstrated an impedimetric lipid cholesterol immunosensor, with the antibody covalently immobilized onto aminated CRGO as the sensing interface. Based on the sensing interface, a detection range of 5–120 mg dL^{-1} and a LOD of 5 mg dL^{-1} were acquired.

7.2.3 Enzymes as bio-recognition elements. Similar to antibodies, extra attention has to be dedicated to the fabrication of
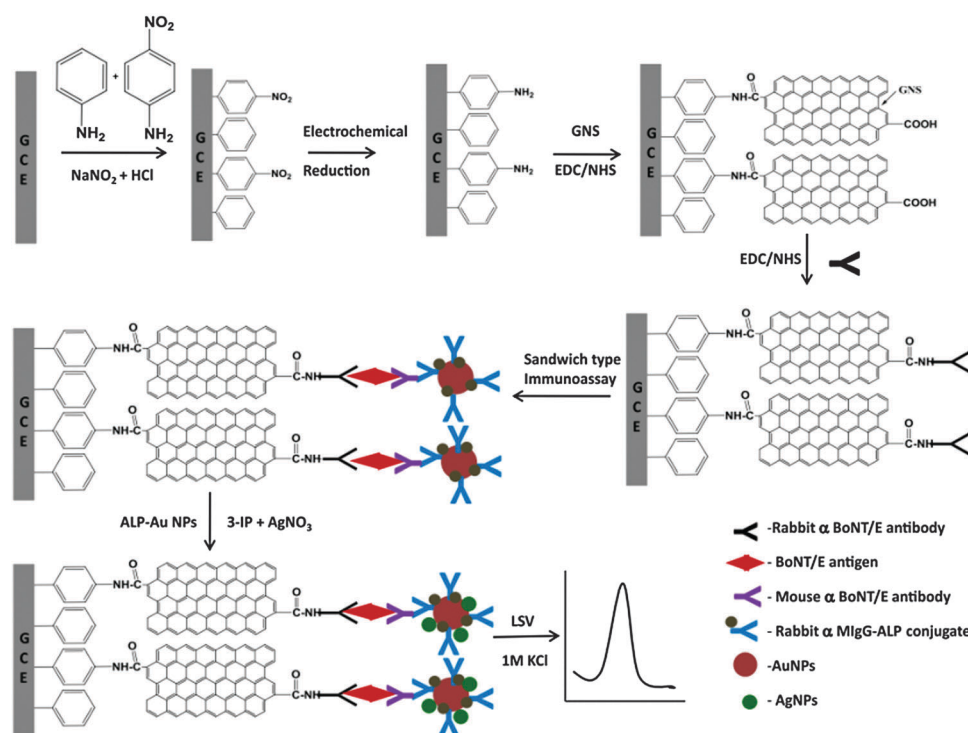

Fig. 22 Fabrication steps for sandwich immunoassay-based detection of BoNT. Upon specific binding with BoNT, a series of recognition events followed and ended with deposition of AgNPs generated by the reaction between MIgG-ALP/AuNPs and 3-IP. Reproduced with permission from ref. 244. Copyright (2015) Elsevier.
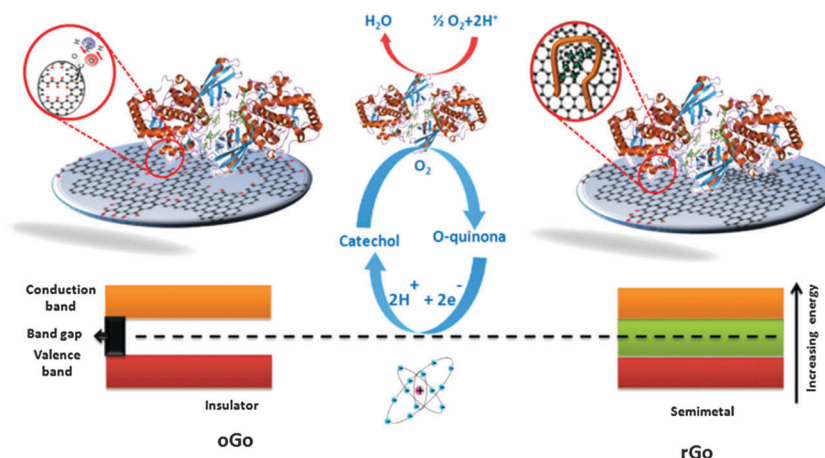
This journal is © The Royal Society of Chemistry 2016

Chem. Soc. Rev., 2016, 45, 2458–2493 | 2487

Fig. 23 Schematic diagram displaying tyrosinase and the reactions involved in the enzymatic detection of catechol on GO and CRGO surfaces. Reproduced with permission from ref. 246. Copyright (2014) Elsevier.

enzymatic bio-recognition layers since enzymes are also a class of proteins. To that aim, the most important enzyme immobilization procedures are:

• Physical adsorption – physical adsorption is a fast and simple method, utilizing hydrophobic interactions to immobilize enzymes onto the surface of graphene materials. Based on this method, there is little or no control over the orientation of the resulting immobilized enzymes.

• Covalent attachment – in covalent attachment, inherent functional groups present on the surface of graphene materials are exploited to form covalent bonds with the exposed side chains of amino acids used to build the enzymes. Based on the type of covalent bonding formed, it may be possible to influence the final orientation of the immobilized enzymes. In addition, this method allows direct anchoring of the enzyme onto the graphene material modified electrode surface. Hence, direct transfer of electrons to the enzyme's active site is enabled.

• Cross-linking – the cross-linking approach involves the use of linker molecules to assist in immobilizing enzymes onto graphene materials through covalent bonds. Such an approach is generally adopted in cases where the surface of graphene materials does not contain or contain insufficient moieties of the desired functional groups.

• Electropolymerization – for this technique, the enzyme is mixed with a monomer molecule which can undergo polymerization before applying an electrochemical procedure to initiate electropolymerization. Incorporation of the enzymes into the polymer matrix is mainly achieved by electrostatic interactions. Using this technique, thin layers can be produced with superior control.

• Layer by layer – the principle behind the layer by layer immobilization approach is based on the attraction between oppositely charged ionic layers on the electrode's surface. By combining layer by layer immobilization and graphene materials, the response of enzymatic biosensors has demonstrated improvements.

Employing an enzymatic bio-recognition layer, electrochemical detection of small molecular targets has been reported.

7.2.3.1 Small molecule analysis. Baptista-Pires *et al.*[246] presented an enzymatic biosensor for catechol using tyrosinase enzyme as a proof-of-concept receptor and graphene materials as the transducing platforms. Tyrosinase enzyme was immobilized onto GO and CRGO by physical adsorption and the biosensing performance of these two materials was compared. The principle of detection lies in tyrosinase enzyme catalyzing the oxidation of catechol to *o*-quinone. The electrochemical reduction of *o*-quinone to catechol was then exploited as the analytical signal using chronoamperometry (Fig. 23). The coupling between catalytic oxidation (catechol to *o*-quinone) and electrochemical reduction (*o*-quinone to catechol) shuttled catechol into a repetitive cycle, leading to potential amplification of the signal. In this work, it was demonstrated that CRGO had better analytical performance than GO. CRGO exhibited a LOD of 0.0103 nM and a sensitivity of 0.0898 $\mu A\ \mu M^{-1}$ while GO displayed a LOD of 0.0711 nM and a sensitivity of 0.0679 $\mu A\ \mu M^{-1}$. The enhanced analytical performance by CRGO was attributed to its higher conductivity and its mode of interactions with the tyrosinase enzyme. Tyrosinase enzyme was physically immobilized onto CRGO *via* hydrophobic interactions while GO interacted with tyrosinase through electrostatic attractions. Hydrophobic interactions for tyrosinase enzyme immobilization were more efficient than electrostatic attraction as the latter adversely affected the activity of the immobilized enzyme.[247] Nevertheless, both types of graphene materials led to better analytical response for the detection of catechol than the unmodified bare electrode.

8. Conclusions

Graphene and its derivatives, such as graphene oxide and heteroatom-doped graphene, proved to have rich electrochemistry. This rich electrochemistry stems from the fact that practically any graphene materials applied for electrochemical measurements do not have an ideal structure as per the IUPAC definition of graphene, but in contrast, they contain defects, amorphous carbon-based impurities, and heteroatoms, among which the

most common is oxygen-containing groups, as well as metals either intentionally or unintentionally introduced into the graphene materials. This rich electrochemistry is not only reflected in the observed "electrocatalysis", but also in the inherent ability of graphene oxide to be oxidized or reduced electrochemically. While there has been tremendous progress in the investigation of graphene since 2010, when our *Chem. Soc. Rev.*[3] tutorial review was published, there is still more room for further research on the determination of underlying reasons for the catalytic activity of graphene materials, such as the recent insight which established that ORR catalysis on N-doped graphene may stem from the electron-deficient carbon neighbouring pyridinic nitrogen.[248] Future avenues are expected to take advantage of developments in materials chemistry, specifically in the chemistry on graphene with inclination towards well-defined graphene structures of nearly stoichiometric composition (*i.e.*, fluorographene, hydrogenated graphene, and graphene oxide), in order to attain both reproducibility and well-understood mechanisms for electrocatalysis.

Acknowledgements

References

1 R. K. Joshi, S. Alwarappan, M. Yoshimura, V. Sahajwalla and Y. Nishina, *Appl. Mater. Today*, 2015, **1**, 1–12.

2 A. C. Ferrari, *et al.*, *Nanoscale*, 2015, **7**, 4598–4810.

3 M. Pumera, *Chem. Soc. Rev.*, 2010, **39**, 4146–4157.

4 J. N. Coleman, *Acc. Chem. Res.*, 2013, **46**, 14–22.

5 A. Ambrosi, C. K. Chua, A. Bonanni and M. Pumera, *Chem. Rev.*, 2014, **114**, 7150–7188.

6 A. V. Krasheninnikov and R. M. Nieminen, *Theor. Chem. Acc.*, 2011, **129**, 625–630.

7 F. M. Hu, T. X. Ma, H. Q. Lin and J. E. Gubernatis, *Phys. Rev. B: Condens. Matter Mater. Phys.*, 2011, **84**, 075414.

8 A. Ambrosi and M. Pumera, *Nanoscale*, 2014, **6**, 472–476.

9 Y. Takada and R. Fujii, *Tanso*, 1985, **1985**, 110–113.

10 M. Noel, R. Santhanam and M. F. Flora, *J. Appl. Electrochem.*, 1994, **24**, 455–459.

11 H. Takenaka, M. Kawaguchi, M. Lerner and N. Bartlett, *J. Chem. Soc., Chem. Commun.*, 1987, 1431–1432, DOI: 10.1039/c39870001431.

12 M. Inagaki, N. Iwashita, Z. D. Wang and Y. Maeda, *Synth. Met.*, 1988, **26**, 41–47.

13 A. Jnioui, A. Metrot and A. Storck, *Electrochim. Acta*, 1982, **27**, 1247–1252.

14 G. Wang, B. Wang, J. Park, Y. Wang, B. Sun and J. Yao, *Carbon*, 2009, **47**, 3242–3246.

15 G. M. Morales, P. Schifani, G. Ellis, C. Ballesteros, G. Martinez, C. Barbero and H. J. Salavagione, *Carbon*, 2011, **49**, 2809–2816.

16 J. Wang, K. K. Manga, Q. Bao and K. P. Loh, *J. Am. Chem. Soc.*, 2011, **133**, 8888–8891.

17 Y. L. Zhong and T. M. Swager, *J. Am. Chem. Soc.*, 2012, **134**, 17896–17899.

18 A. J. Cooper, N. R. Wilson, I. A. Kinloch and R. A. W. Dryfe, *Carbon*, 2014, **66**, 340–350.

19 M. Alanyalioglu, J. Jose Segura, J. Oro-Sole and N. Casan-Pastor, *Carbon*, 2012, **50**, 142–152.

20 V. V. Singh, *et al.*, *Adv. Funct. Mater.*, 2012, **22**, 2352–2362.

21 J. Wang, J. Huang, R. Yan, F. Wang, W. Cheng, Q. Guo and J. Wang, *J. Mater. Chem. A*, 2015, **3**, 3144–3150.

22 C.-Y. Su, A.-Y. Lu, Y. Xu, F.-R. Chen, A. N. Khlobystov and L.-J. Li, *ACS Nano*, 2011, **5**, 2332–2339.

23 K. Parvez, *et al.*, *ACS Nano*, 2013, **7**, 3598–3606.

24 K. Parvez, Z.-S. Wu, R. Li, X. Liu, R. Graf, X. Feng and K. Müllen, *J. Am. Chem. Soc.*, 2014, **136**, 6083–6091.

25 T. J. Davies, M. E. Hyde and R. G. Compton, *Angew. Chem., Int. Ed.*, 2005, **44**, 5121–5126.

26 A. Ambrosi and M. Pumera, *Chem. – Eur. J.*, 2016, **22**, 153–159.

27 J. Liu, *et al.*, *Nano Energy*, 2013, **2**, 377–386.

28 K. S. Rao, J. Senthilnathan, Y.-F. Liu and M. Yoshimura, *Sci. Rep.*, 2014, **4**, 4237.

29 K. S. Rao, J. Sentilnathan, H.-W. Cho, J.-J. Wu and M. Yoshimura, *Adv. Funct. Mater.*, 2015, **25**, 298–305.

30 S. Yang, *et al.*, *J. Am. Chem. Soc.*, 2015, **137**, 13927–13932.

31 M. Hofmann, C. Wan-Yu, T. D. Nguyễn and Y.-P. Hsieh, *Nanotechnology*, 2015, **26**, 335607.

32 Y. Wang, Y. Zheng, X. F. Xu, E. Dubuisson, Q. L. Bao, J. Lu and K. P. Loh, *ACS Nano*, 2011, **5**, 9927–9933.

33 L. B. Gao, *et al.*, *Nat. Commun.*, 2012, **3**, 699.

34 X. H. Wang, *et al.*, *Small*, 2014, **10**, 694–698.

35 C. T. Cherian, F. Giustiniano, I. Martin-Fernandez, H. Andersen, J. Balakrishnan and B. Ozyilmaz, *Small*, 2015, **11**, 189–194.

36 F. Pizzocchero, *et al.*, *Carbon*, 2015, **85**, 397–405.

37 X. W. Yang, H. L. Peng, Q. Xie, Y. Zhou and Z. F. Liu, *J. Electroanal. Chem.*, 2013, **688**, 243–248.

38 L. J. Shi, Y. Q. Liu, F. Yang, L. Gao and J. Sun, *Nanotechnology*, 2014, **25**, 145704.

39 M. Zhou, Y. Wang, Y. Zhai, J. Zhai, W. Ren, F. Wang and S. Dong, *Chem. – Eur. J.*, 2009, **15**, 6116–6120.

40 A. Y. S. Eng, A. Ambrosi, C. K. Chua, F. Šaněk, Z. Sofer and M. Pumera, *Chem. – Eur. J.*, 2013, **19**, 12673–12683.

41 A. Bonanni, A. Ambrosi, C. K. Chua and M. Pumera, *ACS Nano*, 2014, **8**, 4197–4204.

42 L. Chen, Y. Tang, K. Wang, C. Liu and S. Luo, *Electrochem. Commun.*, 2011, **13**, 133–137.

43 A. H. Loo, A. Bonanni and M. Pumera, *Nanoscale*, 2013, **5**, 4758–4762.

44 C. S. Lim, C. K. Chua and M. Pumera, *J. Phys. Chem. C*, 2014, **118**, 23368–23375.

45 A. Ambrosi and M. Pumera, *Chem. – Eur. J.*, 2013, **19**, 4748–4753.

46 D. A. C. Brownson, D. K. Kampouris and C. E. Banks, *Chem. Soc. Rev.*, 2012, **41**, 6944–6976.

This journal is © The Royal Society of Chemistry 2016

Chem. Soc. Rev., 2016, **45**, 2458–2493 | 2489

47 J. G. S. Moo, A. Ambrosi, A. Bonanni and M. Pumera, *Chem. – Asian J.*, 2012, **7**, 759–770.

48 M. M. Hantel, T. Kaspar, R. Nesper, A. Wokaun and R. Kötz, *J. Electrochem. Soc.*, 2013, **160**, A747–A750.

49 M. S. Goh and M. Pumera, *Electrochem. Commun.*, 2010, **12**, 1375–1377.

50 M. D. Stoller, C. W. Magnuson, Y. Zhu, S. Murali, J. W. Suk, R. Piner and R. S. Ruoff, *Energy Environ. Sci.*, 2011, **4**, 4685–4689.

51 J. Xia, F. Chen, J. Li and N. Tao, *Nat. Nanotechnol.*, 2009, **4**, 505–509.

52 H. Marsh and F. Rodríguez Reinoso, *Activated carbon*, Elsiever Ltd., 2006.

53 Y. Zhu, *et al.*, *Science*, 2011, **332**, 1537–1541.

54 Y. Chen, X. Zhang, H. Zhang, X. Sun, D. Zhang and Y. Ma, *RSC Adv.*, 2012, **2**, 7747–7753.

55 L. Zhang, *et al.*, *Sci. Rep.*, 2013, **3**, 1408.

56 X. Sun, P. Cheng, H. Wang, H. Xu, L. Dang, Z. Liu and Z. Lei, *Carbon*, 2015, **92**, 1–10.

57 S. Yun, S.-O. Kang, S. Park and H. S. Park, *Nanoscale*, 2014, **6**, 5296–5302.

58 Y. Xu, *et al.*, *Nano Lett.*, 2015, **15**, 4605–4610.

59 L. Buglione, A. Bonanni, A. Ambrosi and M. Pumera, *ChemPlusChem*, 2012, **77**, 71–73.

60 H. R. Byon, S. W. Lee, S. Chen, P. T. Hammond and Y. Shao-Horn, *Carbon*, 2011, **49**, 457–467.

61 T. Lu, L. Pan, H. Li, C. Nie, M. Zhu and Z. Sun, *J. Electroanal. Chem.*, 2011, **661**, 270–273.

62 L. Qiu, X. Yang, X. Gou, W. Yang, Z.-F. Ma, G. G. Wallace and D. Li, *Chem. – Eur. J.*, 2010, **16**, 10653–10658.

63 Q. Cheng, J. Tang, J. Ma, H. Zhang, N. Shinya and L.-C. Qin, *Phys. Chem. Chem. Phys.*, 2011, **13**, 17615–17624.

64 K.-S. Kim and S.-J. Park, *Electrochim. Acta*, 2011, **56**, 1629–1635.

65 S.-Y. Yang, *et al.*, *J. Mater. Chem.*, 2011, **21**, 2374–2380.

66 L. Buglione and M. Pumera, *Electrochem. Commun.*, 2012, **17**, 45–47.

67 L. Buglione, E. L. K. Chng, A. Ambrosi, Z. Sofer and M. Pumera, *Electrochem. Commun.*, 2012, **14**, 5–8.

68 A. Bonanni and M. Pumera, *Electrochem. Commun.*, 2013, **26**, 52–54.

69 W. Song, X. Ji, W. Deng, Q. Chen, C. Shen and C. E. Banks, *Phys. Chem. Chem. Phys.*, 2013, **15**, 4799–4803.

70 K. Chen, F. Liu, S. Song and D. Xue, *CrystEngComm*, 2014, **16**, 7771–7776.

71 F. Liu, S. Song, D. Xue and H. Zhang, *Adv. Mater.*, 2012, **24**, 1089–1094.

72 M. Seredych, D. Hulicova-Jurcakova, G. Q. Lu and T. J. Bandosz, *Carbon*, 2008, **46**, 1475–1488.

73 W. Kim, J. B. Joo, N. Kim, S. Oh, P. Kim and J. Yi, *Carbon*, 2009, **47**, 1407–1411.

74 L. Zhao, L.-Z. Fan, M.-Q. Zhou, H. Guan, S. Qiao, M. Antonietti and M.-M. Titirici, *Adv. Mater.*, 2010, **22**, 5202–5206.

75 J. P. Paraknowitsch, J. Zhang, D. Su, A. Thomas and M. Antonietti, *Adv. Mater.*, 2010, **22**, 87–92.

76 J. Han, *et al.*, *ACS Nano*, 2013, **7**, 19–26.

77 L. L. Zhang, *et al.*, *Energy Environ. Sci.*, 2012, **5**, 9618–9625.

78 A. Ambrosi, H. L. Poh, L. Wang, Z. Sofer and M. Pumera, *ChemSusChem*, 2014, **7**, 1102–1106.

79 M. Seredych and T. J. Bandosz, *J. Mater. Chem. A*, 2013, **1**, 11717–11727.

80 D. Hulicova-Jurcakova, A. M. Puziy, O. I. Poddubnaya, F. Suárez-García, J. M. D. Tascón and G. Q. Lu, *J. Am. Chem. Soc.*, 2009, **131**, 5026–5027.

81 V. Thirumal, A. Pandurangan, R. Jayavel, K. S. Venkatesh, N. S. Palani, R. Ragavan and R. Ilangovan, *J. Mater. Sci.: Mater. Electron.*, 2015, **26**, 6319–6328.

82 Y. Wen, B. Wang, C. Huang, L. Wang and D. Hulicova-Jurcakova, *Chem. – Eur. J.*, 2015, **21**, 80–85.

83 Y. Xu, X. Huang, Z. Lin, X. Zhong, Y. Huang and X. Duan, *Nano Res.*, 2013, **6**, 65–76.

84 H. Wang, H. S. Casalongue, Y. Liang and H. Dai, *J. Am. Chem. Soc.*, 2010, **132**, 7472–7477.

85 W. Zhou, *et al.*, *Phys. Chem. Chem. Phys.*, 2011, **13**, 14462–14465.

86 L. Xie, *et al.*, *ChemSusChem*, 2015, **8**, 2917–2926.

87 F. Yang, *et al.*, *ACS Appl. Mater. Interfaces*, 2015, **7**, 20513–20519.

88 K. K. Lee, *et al.*, *Nanoscale*, 2012, **4**, 2958–2961.

89 B. G. Choi, M. Yang, W. H. Hong, J. W. Choi and Y. S. Huh, *ACS Nano*, 2012, **6**, 4020–4028.

90 J. Yan, Z. Fan, T. Wei, W. Qian, M. Zhang and F. Wei, *Carbon*, 2010, **48**, 3825–3833.

91 S. D. Perera, A. D. Liyanage, N. Nijem, J. P. Ferraris, Y. J. Chabal and K. J. Balkus Jr, *J. Power Sources*, 2013, **230**, 130–137.

92 W. Shi, *et al.*, *J. Mater. Chem.*, 2011, **21**, 3422–3427.

93 R. B. Rakhi, W. Chen, D. Cha and H. N. Alshareef, *J. Mater. Chem.*, 2011, **21**, 16197–16204.

94 R. B. Rakhi and H. N. Alshareef, *J. Power Sources*, 2011, **196**, 8858–8865.

95 K. Zhang, L. L. Zhang, X. S. Zhao and J. Wu, *Chem. Mater.*, 2010, **22**, 1392–1401.

96 D.-W. Wang, *et al.*, *ACS Nano*, 2009, **3**, 1745–1752.

97 R. R. Salunkhe, S.-H. Hsu, K. C. W. Wu and Y. Yamauchi, *ChemSusChem*, 2014, **7**, 1551–1556.

98 E. G. da Silveira Firmiano, A. C. Rabelo, C. J. Dalmaschio, A. N. Pinheiro, E. C. Pereira, W. H. Schreiner and E. R. Leite, *Adv. Energy Mater.*, 2014, **4**, 1301380.

99 M. A. Bissett, I. A. Kinloch and R. A. W. Dryfe, *ACS Appl. Mater. Interfaces*, 2015, **7**, 17388–17398.

100 K. S. Novoselov, *et al.*, *Science*, 2004, **306**, 666–669.

101 K. S. Novoselov, *et al.*, *Nature*, 2005, **438**, 197–200.

102 F. Schedin, A. K. Geim, S. V. Morozov, E. W. Hill, P. Blake, M. I. Katsnelson and K. S. Novoselov, *Nat. Mater.*, 2007, **6**, 652–655.

103 K. S. Novoselov, V. I. Fal'ko, L. Colombo, P. R. Gellert, M. G. Schwab and K. Kim, *Nature*, 2012, **490**, 192–200.

104 M. Pumera, *J. Mater. Chem. C*, 2014, **2**, 6454–6461.

105 H. Wang, T. Maiyalagan and X. Wang, *ACS Catal.*, 2012, **2**, 781–794.

2490 | *Chem. Soc. Rev.*, 2016, **45**, 2458–2493

This journal is © The Royal Society of Chemistry 2016

106 M. Pumera and C. H. A. Wong, *Chem. Soc. Rev.*, 2013, **42**, 5987–5995.

107 F. Karlicky, K. K. R. Datta, M. Otyepka and R. Zboril, *ACS Nano*, 2013, **7**, 6434–6464.

108 J. J. Duan, S. Chen, M. Jaroniec and S. Z. Qiao, *ACS Catal.*, 2015, **5**, 5207–5234.

109 R. L. McCreery, *Chem. Rev.*, 2008, **108**, 2646–2687.

110 A. Lherbier, X. Blase, Y. M. Niquet, F. Triozon and S. Roche, *Phys. Rev. Lett.*, 2008, **101**, 036808.

111 P. Lazar, R. Zboril, M. Pumera and M. Otyepka, *Phys. Chem. Chem. Phys.*, 2014, **16**, 14231–14235.

112 Y. Wang, Y. Shao, D. W. Matson, J. Li and Y. Lin, *ACS Nano*, 2010, **4**, 1790–1798.

113 M. J. Ju, *et al.*, *ACS Nano*, 2013, **7**, 5243–5250.

114 H. L. Poh, P. Simek, Z. Sofer, I. Tomandl and M. Pumera, *J. Mater. Chem. A*, 2013, **1**, 13146–13153.

115 T. Lin, F. Huang, J. Liang and Y. Wang, *Energy Environ. Sci.*, 2011, **4**, 862–865.

116 S. M. Tan, H. L. Poh, Z. Sofer and M. Pumera, *Analyst*, 2013, **138**, 4885–4891.

117 A. G. Garcia, S. E. Baltazar, A. H. R. Castro, J. F. P. Robles and A. Rubio, *J. Comput. Theor. Nanosci.*, 2008, **5**, 2221–2229.

118 J. Dai, J. Yuan and P. Giannozzi, *Appl. Phys. Lett.*, 2009, **95**, 232105.

119 P. A. Denis, R. Faccio and A. W. Mombru, *ChemPhysChem*, 2009, **10**, 715–722.

120 P. A. Denis, *Chem. Phys. Lett.*, 2010, **492**, 251–257.

121 Z. Yang, *et al.*, *ACS Nano*, 2011, **6**, 205–211.

122 H. L. Poh, P. Šimek, Z. Sofer and M. Pumera, *ACS Nano*, 2013, **7**, 5262–5272.

123 Y. Liu, Y. Ma, Y. Jin, G. Chen and X. Zhang, *J. Electroanal. Chem.*, 2015, **739**, 172–177.

124 M. Li, C. Liu, H. Zhao, H. An, H. Cao, Y. Zhang and Z. Fan, *Carbon*, 2015, **86**, 197–206.

125 J. O. Sofo, A. S. Chaudhari and G. D. Barber, *Phys. Rev. B: Condens. Matter Mater. Phys.*, 2007, **75**, 153401.

126 X. Feng, *et al.*, *J. Mater. Chem. A*, 2013, **1**, 12818.

127 S. M. Tan, Z. Sofer and M. Pumera, *Electroanalysis*, 2013, **25**, 703–705.

128 T. H. Seah, H. L. Poh, C. K. Chua, Z. Sofer and M. Pumera, *Electroanalysis*, 2014, **26**, 62–68.

129 R. R. Nair, *et al.*, *Small*, 2010, **6**, 2877–2884.

130 H. L. Poh, Z. Sofer, K. Klimova and M. Pumera, *J. Mater. Chem. C*, 2014, **2**, 5198–5207.

131 S. Boopathi, T. N. Narayanan and S. Senthil Kumar, *Nanoscale*, 2014, **6**, 10140–10146.

132 P. W. Gong, *et al.*, *Nanoscale*, 2014, **6**, 3316–3324.

133 H. L. Poh, Z. Sofer, P. Šimek, I. Tomandl and M. Pumera, *Chem. – Eur. J.*, 2015, **21**, 8130–8136.

134 X. Ji, X. Zhang and X. Zhang, *J. Nanomater.*, 2015, **2015**, 9.

135 A. Ambrosi, C. K. Chua, B. Khezri, Z. Sofer, R. D. Webster and M. Pumera, *Proc. Natl. Acad. Sci. U. S. A.*, 2012, **109**, 12899–12904.

136 C. K. Chua, A. Ambrosi, Z. Sofer, A. Mackova, V. Havranek, I. Tomandl and M. Pumera, *Chem. – Eur. J.*, 2014, **20**, 15760–15767.

137 C. H. A. Wong, Z. Sofer, M. Kubešová, J. Kučera, S. Matějková and M. Pumera, *Proc. Natl. Acad. Sci. U. S. A.*, 2014, **111**, 13774–13779.

138 L. Wang, A. Ambrosi and M. Pumera, *Angew. Chem., Int. Ed.*, 2013, **52**, 13818–13821.

139 D. S. Geng, *et al.*, *Energy Environ. Sci.*, 2011, **4**, 760–764.

140 Y. Okamoto, *Appl. Surf. Sci.*, 2009, **256**, 335–341.

141 L. P. Zhang and Z. H. Xia, *J. Phys. Chem. C*, 2011, **115**, 11170–11176.

142 H. Kim, K. Lee, S. I. Woo and Y. Jung, *Phys. Chem. Chem. Phys.*, 2011, **13**, 17505–17510.

143 L. Lai, *et al.*, *Energy Environ. Sci.*, 2012, **5**, 7936–7942.

144 D. W. Chang, H.-J. Choi and J.-B. Baek, *J. Mater. Chem. A*, 2015, **3**, 7659–7665.

145 J. Wu, *et al.*, *ACS Appl. Mater. Interfaces*, 2015, **7**, 14763–14769.

146 S. Yasuda, L. Yu, J. Kim and K. Murakoshi, *Chem. Commun.*, 2013, **49**, 9627–9629.

147 X. Kong, Q. Chen and Z. Sun, *ChemPhysChem*, 2013, **14**, 514–519.

148 L. Kavan, *Chem. Rec.*, 2012, **12**, 131–142.

149 L. Wang, Z. Sofer, P. Šimek, I. Tomandl and M. Pumera, *J. Phys. Chem. C*, 2013, **117**, 23251–23257.

150 L. Zhang, J. Niu, M. Li and Z. Xia, *J. Phys. Chem. C*, 2014, **118**, 3545–3553.

151 J. Wang, R. Ma, Z. Zhou, G. Liu and Q. Liu, *Sci. Rep.*, 2015, **5**, 9304.

152 Y. Jiao, Y. Zheng, M. Jaroniec and S. Z. Qiao, *Chem. Soc. Rev.*, 2015, **44**, 2060–2086.

153 J. D. Benck, T. R. Hellstern, J. Kibsgaard, P. Chakthranont and T. F. Jaramillo, *ACS Catal.*, 2014, **4**, 3957–3971.

154 X. Zou and Y. Zhang, *Chem. Soc. Rev.*, 2015, **44**, 5148–5180.

155 J. Duan, S. Chen, M. Jaroniec and S. Z. Qiao, *ACS Catal.*, 2015, **5**, 5207–5234.

156 Y. Zheng, Y. Jiao, M. Jaroniec and S. Z. Qiao, *Angew. Chem., Int. Ed.*, 2015, **54**, 52–65.

157 B. E. Conway and B. V. Tilak, *Electrochim. Acta*, 2002, **47**, 3571–3594.

158 Y. Zheng, Y. Jiao, L. H. Li, T. Xing, Y. Chen, M. Jaroniec and S. Z. Qiao, *ACS Nano*, 2014, **8**, 5290–5296.

159 B. R. Sathe, X. Zou and T. Asefa, *Catal. Sci. Technol.*, 2014, **4**, 2023–2030.

160 Y. Ito, W. Cong, T. Fujita, Z. Tang and M. Chen, *Angew. Chem., Int. Ed.*, 2015, **54**, 2131–2136.

161 P. Lazar, R. Zboril, M. Pumera and M. Otyepka, *Phys. Chem. Chem. Phys.*, 2014, **16**, 14231–14235.

162 X. Huang, Y. Zhao, Z. Ao and G. Wang, *Sci. Rep.*, 2014, **4**, 7557.

163 C. H. Choi, M. W. Chung, H. C. Kwon, S. H. Park and S. I. Woo, *J. Mater. Chem. A*, 2013, **1**, 3694–3699.

164 X. Wang, G. Sun, P. Routh, D.-H. Kim, W. Huang and P. Chen, *Chem. Soc. Rev.*, 2014, **43**, 7067–7098.

165 H. Jiang, Y. Zhu, Y. Su, Y. Yao, Y. Liu, X. Yang and C. Li, *J. Mater. Chem. A*, 2015, **3**, 12642–12645.

166 S. S. Shinde, A. Sami and J.-H. Lee, *ChemCatChem*, 2015, **7**, 3873–3880.

167 J. Duan, S. Chen, B. A. Chambers, G. G. Andersson and S. Z. Qiao, *Adv. Mater.*, 2015, **27**, 4234–4241.

168 Y. Li, Y. Li, E. Zhu, T. McLouth, C.-Y. Chiu, X. Huang and Y. Huang, *J. Am. Chem. Soc.*, 2012, **134**, 12326–12329.

169 R. K. Shervedani and A. Amini, *Carbon*, 2015, **93**, 762–773.

170 Y. Zheng, *et al.*, *Nat. Commun.*, 2014, **5**, 3783.

171 J. Duan, S. Chen, M. Jaroniec and S. Z. Qiao, *ACS Nano*, 2015, **9**, 931–940.

172 N. M. Julkapli and S. Bagheri, *Int. J. Hydrogen Energy*, 2015, **40**, 948–979.

173 S. Chen, J. Duan, Y. Tang, B. Jin and S. Z. Qiao, *Nano Energy*, 2015, **11**, 11–18.

174 J. Yang and H. S. Shin, *J. Mater. Chem. A*, 2014, **2**, 5979–5985.

175 M. Chhowalla, H. S. Shin, G. Eda, L.-J. Li, K. P. Loh and H. Zhang, *Nat. Chem.*, 2013, **5**, 263–275.

176 Y. Li, H. Wang, L. Xie, Y. Liang, G. Hong and H. Dai, *J. Am. Chem. Soc.*, 2011, **133**, 7296–7299.

177 L. Liao, J. Zhu, X. Bian, L. Zhu, M. D. Scanlon, H. H. Girault and B. Liu, *Adv. Funct. Mater.*, 2013, **23**, 5326–5333.

178 X. Dai, *et al.*, *Electrochim. Acta*, 2015, **171**, 72–80.

179 H. Dong, *et al.*, *Sci. Rep.*, 2015, **5**, 17542.

180 S. S. Shinde, A. Sami, D.-H. Kim and J.-H. Lee, *Chem. Commun.*, 2015, **51**, 15716–15719.

181 H. Fei, *et al.*, *Nat. Commun.*, 2015, **6**, 8668.

182 H. Fei, *et al.*, *ACS Appl. Mater. Interfaces*, 2015, **7**, 8083–8087.

183 Y. Hou, Z. Wen, S. Cui, S. Ci, S. Mao and J. Chen, *Adv. Funct. Mater.*, 2015, **25**, 872–882.

184 W. Zhou, *et al.*, *Chem. Mater.*, 2015, **27**, 2026–2032.

185 D. Hou, *et al.*, *J. Mater. Chem. A*, 2015, **3**, 15962–15968.

186 J. Deng, P. Ren, D. Deng and X. Bao, *Angew. Chem., Int. Ed.*, 2015, **54**, 2100–2104.

187 A. Ambrosi, S. Y. Chee, B. Khezri, R. D. Webster, Z. Sofer and M. Pumera, *Angew. Chem., Int. Ed.*, 2012, **51**, 500–503.

188 A. Ambrosi, C. K. Chua, B. Khezri, Z. Sofer, R. D. Webster and M. Pumera, *Proc. Natl. Acad. Sci. U. S. A.*, 2012, **109**, 12899–12904.

189 M. Pumera, A. Ambrosi and E. L. K. Chng, *Chem. Sci.*, 2012, **3**, 3347–3355.

190 L. Wang, A. Ambrosi and M. Pumera, *Angew. Chem., Int. Ed.*, 2013, **52**, 13818–13821.

191 S. Y. Chee and M. Pumera, *Analyst*, 2012, **137**, 2039–2041.

192 R. J. Toh and M. Pumera, *Faraday Discuss.*, 2013, **164**, 275–282.

193 C. H. A. Wong, C. K. Chua, B. Khezri, R. D. Webster and M. Pumera, *Angew. Chem., Int. Ed.*, 2013, **52**, 8685–8688.

194 L. Wang, C. H. A. Wong, B. Khezri, R. D. Webster and M. Pumera, *ChemCatChem*, 2015, **7**, 1650–1654.

195 G. Lupina, *et al.*, *ACS Nano*, 2015, **9**, 4776–4785.

196 C. H. A. Wong, Z. Sofer, M. Kubesova, J. Kucera, S. Matejkova and M. Pumera, *Proc. Natl. Acad. Sci. U. S. A.*, 2014, **111**, 13774–13779.

197 J. P. Smith, C. W. Foster, J. P. Metters, O. B. Sutcliffe and C. E. Banks, *Electroanalysis*, 2014, **26**, 2429–2433.

198 R. M. Iost, F. N. Crespilho, L. Zuccaro, H. K. Yu, A. M. Wodtke, K. Kern and K. Balasubramanian, *ChemElectroChem*, 2014, **1**, 2070–2074.

199 H. L. Poh, Z. Sofer, J. Luxa and M. Pumera, *Small*, 2014, **10**, 1529–1535.

200 A. Ambrosi and M. Pumera, *J. Phys. Chem. C*, 2011, **115**, 25281–25284.

201 L. Wang, A. Ambrosi and M. Pumera, *Chem. – Asian J.*, 2013, **8**, 1200–1204.

202 J. L. Ping and M. S. Fuhrer, *J. Appl. Phys.*, 2014, **116**, 044303.

203 D. R. Dreyer, R. S. Ruoff and C. W. Bielawski, *Angew. Chem., Int. Ed.*, 2010, **49**, 9336–9344.

204 V. Mani, A. P. Periasamy and S. M. Chen, *Electrochem. Commun.*, 2012, **17**, 75–78.

205 W. Y. H. Khoo, M. Pumera and A. Bonanni, *Anal. Chim. Acta*, 2013, **804**, 92–97.

206 C. E. Chng, M. Pumera and A. Bonanni, *Electrochem. Commun.*, 2014, **46**, 137–139.

207 K. H. Hui, M. Pumera and A. Bonanni, *Chem. – Eur. J.*, 2015, **21**, 11793–11798.

208 K. H. Hui, A. Ambrosi, M. Pumera and A. Bonanni, *Chem. – Eur. J.*, 2016, **22**, 3830–3834.

209 F. Long, Z. H. Zhang, J. Wang, L. Yan and B. W. Zhou, *Electrochim. Acta*, 2015, **168**, 337–345.

210 T. M. B. F. Oliveira, *et al.*, *Bioelectrochemistry*, 2014, **98**, 20–29.

211 D. Zhang, *et al.*, *Electrochim. Acta*, 2013, **107**, 656–663.

212 S. Zhou, D. Wei, H. Shi, X. Feng, K. Xue, F. Zhang and W. Song, *Talanta*, 2013, **107**, 349–355.

213 T. Gan, J. Y. Sun, M. M. He and L. L. Wang, *Ionics*, 2014, **20**, 89–95.

214 T. Gan, J. Y. Sun, Z. M. Lin and Y. L. Li, *Anal. Methods*, 2013, **5**, 2964–2970.

215 T. Gan, J. Y. Sun, W. Meng, L. Song and Y. X. Zhang, *Food Chem.*, 2013, **141**, 3731–3737.

216 X. Ye, Y. Du, D. Lu and C. Wang, *Anal. Chim. Acta*, 2013, **779**, 22–34.

217 J. Hou, F. Bei, M. Wang and S. Ai, *J. Appl. Electrochem.*, 2013, **43**, 689–696.

218 H. T. Liu, Y. Q. Liu and D. B. Zhu, *J. Mater. Chem.*, 2011, **21**, 3335–3345.

219 K. H. Hui, A. Ambrosi, Z. Sofer, M. Pumera and A. Bonanni, *Nanoscale*, 2015, **7**, 9040–9045.

220 C. E. Chng, Z. Sofer, M. Pumera and A. Bonanni, *Sci. Rep.*, 2016, **6**, 20673.

221 M. Das Mukherjee, *et al.*, *Sens. Actuators, B*, 2015, **210**, 281–289.

222 A. Benvidi, N. Rajabzadeh, M. Mazloum-Ardakani, M. M. Heidari and A. Mulchandani, *Biosens. Bioelectron.*, 2014, **58**, 145–152.

223 A. Benvidi, N. Rajabzadeh, H. M. Zahedi, M. Mazloum-Ardakani, M. M. Heidari and L. Hosseinzadeh, *Talanta*, 2015, **137**, 80–86.

224 Z. Zhang, L. Q. Luo, G. F. Chen, Y. P. Ding, D. M. Deng and C. H. Fan, *Biosens. Bioelectron.*, 2014, **60**, 161–166.

225 P. A. Rasheed and N. Sandhyarani, *Sens. Actuators, B*, 2014, **204**, 777–782.

226 B. Li, G. H. Pan, N. D. Avent, R. B. Lowry, T. E. Madgett and P. L. Waines, *Biosens. Bioelectron.*, 2015, **72**, 313–319.

2492 | *Chem. Soc. Rev.*, 2016, **45**, 2458–2493

This journal is © The Royal Society of Chemistry 2016

227 V. Urbanova, *et al.*, *Adv. Mater.*, 2015, **27**, 2305–2310.

228 E. L. Sun, *et al.*, *RSC Adv.*, 2015, **5**, 69334–69338.

229 G. Congur, E. Eksin and A. Erdem, *Electrochim. Acta*, 2015, **172**, 20–27.

230 J. Zhang, *et al.*, *Adv. Mater. Interfaces*, 2015, **2**, 1500072.

231 L. A. Wu, E. H. Xiong, Y. Yao, X. Zhang, X. H. Zhang and J. H. Chen, *Talanta*, 2015, **134**, 699–704.

232 Y. L. Zhang, *et al.*, *Electrochim. Acta*, 2015, **170**, 210–217.

233 S. R. Tang, P. Tong, W. Lu, J. F. Chen, Z. M. Yan and L. Zhang, *Biosens. Bioelectron.*, 2014, **59**, 1–5.

234 S. Eissa, *et al.*, *Nano Res.*, 2015, **8**, 1698–1709.

235 B. Jin, *et al.*, *Biosens. Bioelectron.*, 2014, **55**, 464–469.

236 A. H. Loo, A. Ambrosi, A. Bonanni and M. Pumera, *RSC Adv.*, 2014, **4**, 23952–23956.

237 Y. Y. Wang, *et al.*, *Microchim. Acta*, 2015, **182**, 2061–2067.

238 G. L. Yuan, C. Yu, C. Y. Xia, L. L. Gao, W. L. Xu, W. J. Li and J. L. He, *Biosens. Bioelectron.*, 2015, **72**, 237–246.

239 D. Wu, A. P. Guo, Z. K. Guo, L. L. Xie, Q. Wei and B. Du, *Biosens. Bioelectron.*, 2014, **54**, 634–639.

240 J. J. Shi, T. T. He, F. Jiang, E. S. Abdel-Halim and J. J. Zhu, *Biosens. Bioelectron.*, 2014, **55**, 51–56.

241 J. Kailashiya, N. Singh, S. K. Singh, V. Agrawal and D. Dash, *Biosens. Bioelectron.*, 2015, **65**, 274–280.

242 S. A. Lim, H. Yoshikawa, E. Tamiya, H. M. Yasin and M. U. Ahmed, *RSC Adv.*, 2014, **4**, 58460–58466.

243 H. V. Tran, B. Piro, S. Reisberg, L. H. Nguyen, T. D. Nguyen, H. T. Duc and M. C. Pham, *Biosens. Bioelectron.*, 2014, **62**, 25–30.

244 J. Narayanan, M. K. Sharma, S. Ponmariappan, S. M. Shaik and S. Upadhyay, *Biosens. Bioelectron.*, 2015, **69**, 249–256.

245 M. A. Ali, K. K. Reza, S. Srivastava, V. V. Agrawal, R. John and B. D. Malhotra, *Langmuir*, 2014, **30**, 4192–4201.

246 L. Baptista-Pires, *et al.*, *Biosens. Bioelectron.*, 2014, **61**, 655–662.

247 Y. Zhang, J. Zhang, X. Huang, X. Zhou, H. Wu and S. Guo, *Small*, 2012, **8**, 154–159.

248 D. Guo, R. Shibuya, C. Akiba, S. Saji, T. Kondo and J. Nakamura, *Science*, 2016, **351**, 361–365.

This journal is © The Royal Society of Chemistry 2016

Chem. Soc. Rev., 2016, **45**, 2458–2493 | 2493